# INVESTIGATION OF THE STRUCTURAL PROPERTIES OF SILICENE NANORIBBONS BY MOLECULAR DYNAMICS SIMULATIONS

THESIS SUBMITTED TO
THE GRADUATE SCHOOL OF NATURAL AND APPLIED SCIENCES
OF
MIDDLE EAST TECHNICAL UNIVERSITY

BY

ALPER İNCE

IN PARTIAL FULFILLMENT OF THE REQUIREMENTS
FOR
THE DEGREE OF THE MASTER OF SCIENCE
IN
MICRO AND NANOTECHNOLOGY

MAY 2012

Approval of the thesis:

**INVESTIGATION OF THE STRUCTURAL PROPERTIES OF SILICENE NANORIBBONS BY MOLECULAR DYNAMICS SIMULATIONS**

submitted by **ALPER İNCE** in partial fulfillment of the requirements for the degree of **Master of Science in Micro and Nanotechnology Department, Middle East Technical University** by

Prof. Dr. Canan Özgen _____
Dean, **Graduate School of Nat. and Applied Sciences**

Prof. Dr. Mürvet Volkan _____
Head of Department, **Micro and Nanotechnology**

Prof. Dr. Şakir Erkoç _____
Supervisor, **Physics Dept., METU**

Prof. Dr. Mehmet Kadri Aydınol _____
Co-advisor, **Metal. and Materials Eng. Dept.,METU**

**Examining Commitee Members:**

Prof. Dr. Güngör Gündüz _____
Chemical Engineering Dept., METU

Prof. Dr. Şakir Erkoç _____
Physics Dept., METU

Prof. Dr. Mehmet Kadri Aydınol _____
Metallurgy and Materials Engineering Dept.,METU

Assist. Prof. Dr. Yiğit Yazıcıoğlu _____
Mechanical Engineering Dept., METU

Assist. Prof. Dr. Hande Toffoli _____
Physics Dept., METU

**Date:**

**I hereby declare that all information in this document has been obtained and presented in accordance with academic rules and ethical conduct. I also declare that, as required by these rules and conduct, I have fully cited and referenced all material and results that are not original to this work.**

Name, Last name: Alper İNCE

Signature:

## ABSTRACT


**INVESTIGATION OF THE STRUCTURAL PROPERTIES OF SILICENE NANORIBBONS BY MOLECULAR DYNAMICS SIMULATIONS**

İNCE, Alper

M.Sc., Department of Micro and Nanotechnology

Supervisor: Prof. Dr. Şakir ERKOÇ

Co-Supervisor: Prof. Dr. Mehmet Kadri AYDINOL

May 2012, 148 Pages

With the emergence of nanotechnology, mankind has obtained the capability to manipulate materials at nanoscale and this led to the invention of a new group of novel materials like carbon nanotubes, graphene and quantum nanodots. Silicene nanoribbons (SiNRs) are one of the newest members of this nanomaterial family which has been synthesized very recently by deposition on silver substrates. A SiNR sheet is made up of a layer of two dimensional honeycomb structure solely composed of silicon atoms. In this thesis, structural and mechanical properties of SiNR are being investigated with the help of classical empirical molecular dynamics simulation technique.

In the first part of this thesis, structural properties of SiNR sheets have been investigated. This investigation has been carried out by performing classical molecular dynamics simulations using atomistic many-body potential energy functions at many different SiNR sheet lengths and widths, at low and room temperatures with and without periodic boundaries. It has been found that SiNR

sheets do not have perfectly flat honeycomb geometry. It has also been found that finite length models are more likely to form tubular structures resembling distorted silicon nanotubes at room temperature.

In the second part of this thesis, mechanical properties of SiNRs have been investigated. Mechanical properties of silicene nanoribbons of varying width have been investigated under 5% and 10% uniaxial strain via classical Molecular-Dynamics simulations at 1 K° and 300 K° temperatures by the aid of atomistic many-body potential energy functions. It has been found that under strain, SiNRs show such material properties: they are very ductile, they have considerable toughness and despite their low elasticity, they have a very long plastic range before fragmentation.

Keywords: Silicene, Silicene nanoribbons, Molecular-dynamics, Atomistic simulations

# ÖZ

## MOLEKÜLER DİNAMİK BENZETİMİ İLE SİLİSEN NANOŞERİTLERİN YAPISAL ÖZELLİKLERİNİN İNCELENMESİ

İNCE, Alper

Yüksek Lisans, Mikro ve Nanoteknoloji Bölümü
Tez Yöneticisi: Prof. Dr. Şakir ERKOÇ
Ortak Tez Yöneticisi: Prof.Dr. Mehmet Kadri AYDINOL

Mayıs 2012, 148 Sayfa

Nanoteknolojinin ortaya çıkmasıyla, insanoğlu malzemeleri nano ölçekte işleyebilme kabiliyetine erişti ve bu da karbon nanotüpler, grafen ve kuantum noktalar gibi özgün malzemelerin icadını sağladı. Sentezi henüz çok yakın bir geçmişte gümüş substratlar üzerine çöktürülerek gerçekleştirilen Silisen nanoşeritler (SiNŞler) bu nanomalzeme ailesinin en yeni üyelerinden biridir. Bir SiNŞ tabaka sadece silikon atomlarından oluşan iki boyutlu petek yapıya sahip bir katmandan meydana gelmektedir. Bu tezde, SİNŞ tabakaların yapısal ve mekanik özellikleri klasik empirik moleküler dinamik benzetimi tekniği ile incelenmektedir.

Bu tezin ilk kısmında, SİNŞ tabakaların yapısal özellikleri incelenmektedir. Bu inceleme farklı SiNŞ tabaka uzunluklarında ve kalınlıklarında, düşük sıcaklıkta ve oda sıcaklığında, periyodik sınırlarla ve periyodik sınırlar olmaksızın atomistik n-cisimli potansiyel enerji fonksiyonlarını kullanan klasik moleküler dinamik benzetimi yönteminin uygulanmasıyla gerçekleştirilmiştir. Çalışmada, SiNŞ

tabakaların kusursuz, düz petek geometriye sahip olmadıkları gözlenmiştir. Aynı zamanda da, sonlu uzunluğa sahip modellerde SİNŞ tabakaların oda sıcaklığında bozulmuş silikon nanotüplere benzeyen tüpümsü yapılar oluşturmaya eğilimli olduğu da görülmüştür.

Tezin ikinci kısmında, SiNŞ tabakaların mekanik özellikleri incelenmiştir. Farklı kalınlıklara sahip SiNŞ tabakaların mekanik özellikleri, 1 K° ve 300 K° sıcaklıklarda %5 ve %10'luk tek eksenli gerinim altında atomistik n-cisimli potansiyel enerji fonksiyonu ile yapılan moleküler dinamik benzetimleri aracılığıyla incelenmiştir. Gerinim altında SİNŞ tabakaların şu malzeme özelliklerine sahip oldukları gözlenmiştir: SİNŞ şeritler sünektirler, kayda değer miktarda tokluğa sahiptirler ve düşük elastisiteye sahip olmalarına karşın, kopma noktasından önce uzun bir plastik esneme alanına sahiptirler.

Keywords: Silisen, Silisen nanoşeritler, Moleküler Dinamik, Atomistik simülasyonlar

**To all the warriors of light in their labcoats,**

## ACKNOWLEDGEMENTS

First and foremost I offer my sincerest gratitude to my supervisor, Prof. Dr. Şakir Erkoç, who has supported me thoughout my thesis with his patience and knowledge whilst allowing me the room to work in my own way. One simply could not wish for a better or friendlier supervisor. I would also like to express my deepest gratitute to my co-supervisor Prof. Dr. Mehmet Kadri Aydınol for their guidance, advice, criticism, encouragements and insight throughout the research. I would like to thank Asst. Prof. Dr. Hande Toffoli for her efforts in teaching me Density Functional Theory, giving her valuable opinions about the work in this thesis and supporting me during the course of this study in many ways.

I would especially like to thank Hilal Ezgi Toraman for supporting me emotionally throughout all my studies at the Micro and Nanotechnology department whenever I felt short of ambition to keep on going.

## TABLE OF CONTENTS

# LIST OF TABLES

**TABLES**

## LIST OF FIGURES

**FIGURES**

# CHAPTER I

# INTRODUCTION

## 1.1 A Brief Introduction to Nanotechnology

Throughout the history, the relationship between mankind and nature has always been a very strong function of how humans benefit from the nature. In fact, civilization is a measure of the extent of a society's capability to manipulate nature, namely, the materials that nature provides. The relationship between mankind and the materials became much more important than ever after the scientific development in Europe and the following Industrial Revolution in England in the $18^{th}$ century. Now, the extent of this relationship is considered as a major indicator of the development of a country. Through the end of $20^{th}$ century, a new field of technology aiming to revolutionize the mankind-materials relationship has emerged. This technology was coined nanotechnology that studies materials at atomic scale and aims to manipulate them with atomic accuracy for the benefit of the human kind.

In the late 1970s, the word "nanotechnology" was first used by Norio Tanaguchi [1] in order to describe this revolutionary technological development. When we look at the etymology of the word "nanotechnology", we see that the word "nano" is derived from a Greek word meaning "dwarf" [2]. Considering that 1 nm is one-billionth of a meter, such an appellation is of no coincidence. Development of a technology with an accuracy of dealing with materials at that small scale will surely develop the quality of the resulting end-products since this technology will provide more opportunities for a material designer in manipulating the materials. Nanotechnology promises not only higher quality for the present products but it also

evokes emergence of new products and new technologies that were not possible to develop before.

Despite the fact that there are many different definitions of nanotechnology, definition of the National Nanotechnology Initiative (NNI) is widely used. The NNI defines a branch of technology as "nanotechnology" only if it involves all of the following:

- Ability to control or manipulate on the atomic scale.

-Research and technology development at the atomic, molecular, or macromolecular levels, in the length scale of approximately 1 to 100-nanometer range.

- Creating and using structures, devices, and systems that have novel properties and functions because of their small and/or intermediate size [3].

In the early 1980's, K. Eric Drexler published a book "Engines of Creation: The Coming Era of Nanotechnology" which made the word "nanotechnology" very popular [4]. He attended Richard Feynman's famous talk entitled "There's plenty of room at the bottom" in 1959 in Caltech which he later named as "the promise that launched nanotechnology" on the $50^{th}$ anniversary of Feynman's talk [5]. Drexler was deeply fascinated about the nano idea and in the book that he wrote back in 1986, he mentioned about fully functioning robots, computers, and motors of a scale that is smaller than a cell. Despite the fact that Drexler's attitude towards nanotechnology was considered as an enthusiastic approach, he was also the one who created the "grey goo" scenario which envisioned a pessimistic future for nanotechnology in which nanoparticle assemblers cease to follow their programmed instructions and start consuming all of the Earth's resources like cancerous cells [6].

Nowadays, nanotechnology finds application in a wide variety of areas: sporting goods where carbon nanoparticles are utilized to stiffen areas of the racquet head and shaft where tennis balls are coated internally with membranes produced at the nano-scale; automotive sector where car paints and waxes with scratch resistant properties are produced with the help of nano-sized agents; in the medical sector

where antibacterial cleansers and medical bandages with nano-scale silver are used to kill pathogens; cosmetics sector where in sunscreens, zinc oxide nanoparticles which protect the skin and prevent white marks on the skin are used. In addition to these applications, nanotechnology is very important in organic light-emitting displays or OLEDs which constitute ideal displays for mobile electronics like cellular phones, digital cameras and handheld computers [2,7].

It should be noted that nanotechnology is still in its infancy and it promises much more than it has achieved up to now. Some future applications of nanotechnology are expected to include applications in environment where nanoparticles will trap organic contaminants in water and mitigate pollution; in solar cells which will efficiently utilize the energy of sun (which is nearly an infinite energy source) and in fuel cells which utilize energy of chemical bonds by converting their chemical energy into electricity and heat so that one of the most important problems on earth, namely the problem of energy will come to an end. Future applications encompass medical applications like lab-on-a-chip which is a nanoscale electronic device designed to diagnose and monitor medical conditions of a patient and controlled drug delivery systems which deliver the drug directly to a targeted location within the human body with nanoscale accuracy like delivering anti-cancer drugs directly to the cancerous site in the body so that healthy cells in the body are not affected by the poisonous effect of these drugs [7].

## 1.2 Research Methods in Nanotechnology

Nanotechnology research, which is primarily a materials research, is carried out with many different methods which can mainly be classified into two distinct groups: experimental and theoretical studies. These two different approaches both serve the science behind nanotechnology to gain better insight about the material being studied.

### 1.2.1 Experimental Methods

The primary requirement of research at the nanoscale is the presence of tools that enable magnification at nanoscale so that the material under investigation and its properties can be visualized. Light microscopes or optical microscopes were first invented in the beginning of 17$^{th}$ century [8] and in time, they have evolved so that they could use the full capacity of visible light to obtain maximum resolution. Even after these developments, the resolution of light microscopes were far away from the nanoscale (the way it is termed now which is the 0-100 nm range) due to the wavelength of the visible light which is in the range of 390nm-750nm. The theoretical maximum resolution (denoted as d) of a light microscope is limited by the wavelength of the photons used (denoted as λ) and the numerical aperture of the system (denoted as NA) which is given in Eq. 1.1 [9]. Here, the resolution limit of light microscopes is approximately 200 nm even though many of these microscopes cannot achieve this resolution due to other factors (like aberration of lenses).

$$d = \frac{\lambda}{2n \sin \alpha} \approx \frac{\lambda}{2NA} \tag{1.1}$$

In the 20$^{th}$ century, researchers started to use electrons instead of visible light to overcome the resolution limit described above. In 1931, Max Knoll and Ernst Ruska invented the Transmission Electron Microscope (TEM) which uses the basic principles of light microscope but uses electromagnets instead of glass lenses and electrons instead of light. In this device, electrons are transmitted through the sample and information about the material being investigated has been collected with the aid of these electrons. Later in 1935, Max Knoll developed Scanning Electron Microscope (SEM) [10] where electrons interact with the atoms in the sample without passing through them and this interaction produces signals that carry the crucial information about the surface topography, composition, morphology and other properties of the material. SEM and TEM cannot operate in air or water; these microscopes have to operate under vacuum conditions since presence of any other atoms within the microscope slows down the speed of electrons and diffracts them due to collisions.

Even though TEM and SEM enabled resolution at the nanoscale, the advent of these devices could not trigger the nanotechnology revolution at that époque. It can be said that the era of nanotechnology truly started after the invention of Scanning Probe Microscopes (SPM) and especially Scanning Tunneling Microscope (STM) by Gerd Binnig and Heinrich Röhrer in 1981 which earned them a Nobel Prize in 1986 [11,12]. With the aid of these microscopes, resolution of 0.1 nm and even lower resolutions became possible [13]. In STM, surface of the sample is analyzed with a very sharp conducting tip that is attached to the end of a cantilever. A voltage difference, named as bias, is applied to the conducting tip and the sample, so a circuit is obtained through which electrons are transported by tunneling through the distance between them. As the tip scans across the surface, information is obtained by monitoring the tunneling current and displayed in 3D topographic image form [14]. Atomic Force Microscope (AFM) can be considered as another very important microscopic technique in the SPM family. The difference of AFM from STM lies in the measurement technique: AFM uses the intermolecular van der Waals interactions between the tip and the surface instead of tunneling to obtain the topography of the surface. AFM not only enables visualization with 3D surface profiles with higher resolutions than SEM and TEM can provide but it also has the capability of manipulating surfaces by moving the atoms with the aid of the tip. Picking up, dragging and positioning atoms to any desired location on the sample surface is possible by AFM which is another property that makes this device a cornerstone for the material science. Historically, the advent of scanning probe microscopes and the atomic force microscope can be considered to flag the start of the nanotechnology era [15].

There is another group of techniques coined as spectroscopic methods some of which are NMR, IR or FTIR, UV-VIS, Raman and XPS spectrometry techniques. In these methods, one does not directly see the geometry of the material; what is seen there is the measurement of intensity peaks with respect to the changing wavelengths or frequencies of electromagnetic radiation sent to the material. For example, the abbreviations like IR (infrared), UV (ultraviolet) and VIS (visible) represent the

region of the electromagnetic spectrum to which the frequency or wavelength of the electromagnetic radiation sent to the material belongs. The amount of electromagnetic radiation absorbed or emitted is measured and these measurements create peaks when the amount of absorbed/emitted radiation is plotted against the wavelength of electromagnetic radiation sent to the sample. The peaks give plenty of physical and chemical information about the properties of material under investigation [16,17].

### 1.2.2 Computational Methods

In experiments, it is well known that there is no physical quantity that can be measured perfectly and hence, there are always errors and analyzing errors in an experiment is very crucial for analyzing the result of an experiment. It should be taken into consideration that the sources of errors are not always human based in an experiment (i.e. based on the carelessness of the person conducting the experiment), these errors can be due to the method or the equipment used (for example; errors due to noise) [18,19].

In theoretical studies, researchers always get confronted with very complex calculations where equations cannot be solved analytically. So, numerical and mostly iterative methods for solving complex calculations come into play with the errors introduced due to the assumptions of the numeric method employed. For instance: classical molecular dynamics simulation techniques use Verlet algorithms [20] or Predictor-Corrector algorithms [21] to solve ordinary differential equations which are in fact equations of motion (Newton's Laws). Since ordinary differential equations are solved by taking integrals of both sides of a differential equation, the numeric method applied in this case is a numerical integrator, which succeeds in taking the integral numerically which is very hard or mostly impossible otherwise. Along with the numeric methods applied, almost every calculation involves approximations which lead to the deviation of the result from the exact solution. For example, density functional theory (DFT) method applies Born-Oppenheimer approximation [22,23] which simply states that the total wavefunction of a system can be separated

as the nuclear wavefunction and the electronic wavefunction of that system (which simply means that nuclei and electrons can be dealt separately) based on the fact that the nuclei are very slow when compared to the surrounding electrons, so most DFT calculations treat the nuclei classically. But there may be other types of approximations which may only be used under certain circumstances, so the code developer or the user should be well aware of the underlying scientific theory behind the computer code since every computer simulation code cannot be used to assess the properties of any material under any circumstance.

Theoretical or computational studies are very crucial in nanotechnology since every experiment cannot be realized due to many different factors: some experiments may not be possible to conduct with the available technology or are too expensive to conduct without knowing that the results of the experiment will refund its initial cost. In some cases, experiments are too dangerous to realize before knowing its outcomes or it is too hard to characterize a resulting material or some part of a material in the desired range of precision.

## 1.3 Computational Research Methods in Nanotechnology

Nowadays, in computational material science, the computational methods (which encompass simulation methods at atomic or smaller levels which do not include larger scale simulation methods like computational fluid dynamics) are classified into two broad groups as: atomistic simulation methods and electronic simulation methods.

### 1.3.1 Atomistic Simulation Methods

Atomistic simulation methods calculate the interactions between atoms and molecules with the aid of classical and statistical physics take electrons and electronic interactions into account indirectly. Disregarding Schrödinger equation enables a greater number of atoms to be simulated with a computationally cheaper (in the sense of shorter calculation time) approach. Evidently, it is impossible to obtain electronic information like energy band gaps, density of states, and

conductivity with these techniques. Among the atomistic simulation methods, two of them stand a step ahead that has proved important in the test of time: Molecular Dynamics (MD) and Monte Carlo (MC) methods. Apart from these techniques, there are also other methods specialized and proven useful for specific cases such as Brownian Dynamics Method (BD) and Lattice Dynamics (LD) Method. Brownian Dynamics Method is very useful in simulating the motion of atoms in gases and solutions [24] whereas Lattice Dynamics Method is generally applied to crystalline solid materials where the vibration frequencies of the phonons inside crystals are studied. Even though MD and MC are classified here as atomistic simulation methods, they can be used with the electronic methods as well, such as Quantum Molecular Dynamics and Quantum Monte Carlo methods.

In MD simulations, Newton's laws of motion are applied to determine the trajectory of particles, which demonstrate evolution of the system in time. So, molecular dynamics is a deterministic method: given an initial set of positions and velocities, the subsequent time evolution is completely determined. The laws of motion may be formed in Lagrangian, Hamiltonian or the Newtonian formalisms all of which formulate the basic laws of motion in different ways within the framework of classical mechanics [25]. More details about these formalisms and a detailed explanation of the theory underlying Molecular Dynamics Simulation will be given in **Section 2.1** since the study conducted in this thesis is carried out by utilizing software coded on the basis of Molecular Dynamics simulation technique.

The other important method, namely the Monte Carlo Simulation Method (MC) was first developed by Von Neumann, Ulam, and Metropolis in order to make a calculation on the diffusion of neutrons in fissionable material. Historically MC is an important method since it is the first technique with which the computational calculations have been carried out [26]. In the MC method, the initial geometry is given a random perturbation (as if the atoms are kicked by a random force) and the new configuration is formed based on the ratio of the probabilities for the new and old configurations, according to the Metropolis algorithm. Rather than trying to reproduce the dynamics of a system as in MD simulation, MC generates states

according to appropriate Boltzmann probabilities. This criterion for acceptance is also known as the Metropolis condition [26]. If the new configuration is accepted, simulation continues running with the new configuration. If the new configuration is rejected, then the old configuration is taken as the new one. Repeating this procedure many times accumulates sums for averages [26, 27].

When MC and MD methods are compared, it is clearly seen than the most important difference between these two techniques is the concept of time which is central to the application of MD. As mentioned before, MD simulations create trajectories of particles which show evolution of a system of particles in time whether the system is in equilibrium or not. So, MD is a dynamic method as its name implies. With MD, one can obtain transient information by analyzing the system as it moves from one thermodynamic equilibrium state to another equilibrium state. So, with MD, one can obtain some dynamic properties related with transport phenomena like mass transfer diffusion constant. In contrast to MD, MC method does not use equations of motion since it is rather a stochastic method based on the generation of a series of microscopic states under a certain stochastic law working regardless of the laws of motion that govern the motion of the system [28].

### 1.3.2 Electronic Simulation Methods

As mentioned in **Section 1.3.1**, classical atomistic simulation methods neglect the presence of electrons and electronic interactions. Apart from the simulation methods mentioned, there are other kind of hybrid methods between classical atomistic calculation techniques and electronic methods like *ab-initio* molecular dynamics where computation of the forces acting on the nuclei is carried out from electronic structure calculations while trajectories are calculated from Newton's classical equations of motion [29].

The Schrödinger equation is the central equation of quantum mechanics by which the properties of all electronic systems are described in contemporary physics.

The most general form of Schrödinger equation given in Eq. 1.2 is a measure of the time dependence of the quantum state of a physical system. This equation is also called as the time-dependent Schrödinger equation.

$$i\hbar\frac{\partial}{\partial t}\psi = \hat{H}\psi \tag{1.2}$$

For the stationary solutions, Schrödinger equation takes a simplified form given in Eq. 1.3. This is the time-independent Schrödinger equation [30].

$$\hat{H}\psi = E\psi \tag{1.3}$$

All the electronic simulation methods are devised to bring solutions to either the time-dependent or time-independent forms of Schrödinger equation given above. Since analytical solution of the Schrödinger equation is impossible except very rare cases like the particle in a box, the harmonic oscillator, particle on a ring and the hydrogen atom [31], all of the electronic simulation methods are techniques that include different approximations. These methods can be classified into two broad groups as wavefunction based methods and density based methods.

Wavefunction based methods require determination of ground-state wavefunction in the first place. With the aid of this information, they calculate the ground-state energy of a quantum many body system.

An important wavefunction based electronic simulation method coined as the Hartree-Fock (HF) method makes the assumption that the wavefunction can be approximated by a Slater determinant of N spin-orbitals. HF method uses the Fock operator given in Eq. 1.4 on this wavefunction to obtain the solutions of the Schrödinger equation in the form given in Eq. 1.5. For each *i* in Eq. 1.5, there is an equivalent equation defining a system of Schrödinger-like, one-particle equations.

$$\hat{F} = \hat{h}_1 + \sum_i(\hat{J}_i - \hat{K}_i) \tag{1.4}$$

$$\hat{F}\phi_i = \epsilon_i \phi_i \tag{1.5}$$

The components of the Fock operator that are included in Eq. 1.5 are as follows: $\hat{h}_1$ is the Hamiltonian that is dependent only on one generalized coordinate that includes both spatial and spin degrees of freedom of one electron; $\hat{J}_i$ is the direct term which corresponds to the classical interaction of electrons (distributions) and $\hat{K}_i$ is the exchange term which introduces antisymmetry effects into the Fock operator. It should be noted that the exchange term arises from the concept of antisymmetry of fermionic systems and this term has no classical analogue. It has the effect of making the electrons of the same spin "avoid" each other [32] and this way the system obeys Pauli's exclusion principle: two fermions cannot occupy the same quantum state simultaneously.

In HF method, the equations are solved by an iterative algorithm due to the nonlinearities arising from the Hartree-Fock approximation used in defining the wavefunctions and this is the reason why this method is also called as Self-Consistent Field (SCF) method.

The HF approximation assumes the wavefunction as a single Slater determinant or a combination of a few Slater determinants but this approximation creates an error. This error is called as the correlation energy which is the difference between the true total energy and the HF energy of a system as given in Eq. 1.6.

$$E_{corr}^{HF} = E - E_{HF} \tag{1.6}$$

The origin of correlation energy is the repulsion between electrons which is not taken into consideration in Hartree-Fock calculations. Some examples to the wavefunction based methods that incorporate the calculation of correlation energy are the configuration interaction (CI) methods [33] and many body perturbation theory (abbreviated as MP2, MP3, MP4 where the numbers 2, 3, 4 represent the order of the correction to the energy that the method provides) [34]. There are other semi empirical electronic methods like zero differential overlap (ZDO), complete neglect of differential overlap (CNDO), intermediate neglect of differential overlap

(INDO) that simplify the Fock operator mathematically using different assumptions in order to lessen the amount of computational effort required to complete the SCF HF calculation [31].

In contrast to the wavefunction based methods, Density Functional Theory (DFT) uses the electronic density $n(r)$ as the basic variable rather than trying to determine the wavefunction. DFT formalism is known as the Kohn-Sham formalism due to the elegant use of Kohn-Sham orbitals in defining the electronic density (Eq. 1.7) [35, 36].

$$n(\vec{r}) = \sum_n^{N_e} |\phi_n(\vec{r})|^2 \tag{1.7}$$

In the DFT formalism, the total energy is calculated as given in Eq.1.8.

$$E = -\frac{1}{2}\sum_n^{N_e} \int d\vec{r}\phi_n^*(\vec{r})\nabla^2\phi_n(\vec{r})d\vec{r} + \int n(\vec{r})V_{ne}(\vec{r})d\vec{r}$$

$$+ \frac{1}{2}\iint d\vec{r}d\vec{r}' \frac{n(\vec{r})n(\vec{r}')}{|\vec{r}-\vec{r}'|} + \Delta T + \Delta E_{ee} \tag{1.8}$$

where $n(\vec{r})$ is the electronic density, $\phi_n(\vec{r})$ represents the Kohn-Sham orbitals, $N_e$ is the total number of electrons, $V_{ne}$ is the potential representing nucleus-electron interaction, $\Delta E_{ee}$ is the difference between electron-electron interaction energy and the Hartree energy, $\Delta T$ is the difference between total kinetic energy and the single electron kinetic energy which is given as the first term at the right of Eq. 1.8.

The effects of exchange and correlation are included in the last two terms of Eq. 1.8. DFT definition of exchange-correlation functionals is the sum of these two terms, given in Eq. 1.9 [37, 38]. There is a great deal of exchange-correlation functionals approximating the calculations required in a DFT simulation like the local density approximation (LDA) and the generalized gradient approximation (GGA) and other methods (like hybrid XC functionals) are still being developed to balance computational effort with accuracy in electronic calculations [39,40].

$$E_{xc} = \Delta E_{ee} + \Delta T \tag{1.9}$$

# 1.4 A Novel Nanomaterial: Silicene Nanoribbon

## 1.4.1 Graphene and the Idea of Silicene

Graphene is a planar two dimensional sheet comprised of carbons formed in a honeycomb fashion, which has been used to elucidate properties of other important carbon based materials like fullerenes and carbon nanotubes. Two dimensional (2D) systems, such as graphene nanoribbons have become one of the most important materials in nanotechnology due to its crystallographic quality, stability under ambient conditions [41] and the massless Dirac fermion-like behavior of its charge carriers [42]. Uniqueness of most graphene nanoribbons in the world of materials lies in its linear energy dispersion relation close to the K point in the Brillouin zone which is a property that most materials do not have; they rather have a parabolic dispersion around the K point [43]. In the literature, linear energy dispersion of the graphene is coined as the Dirac cone because the three dimensional energy dispersion that is in the proximity of K point resembles the shape of a cone. The phrase "massless Dirac fermion-like behavior" refers to the behavior of the electrons in this conical region which obeys Dirac's equation for massless Dirac fermionic particles rather than the Schrödinger equation which is the equation that describes the behavior of regular electronic systems. The reason of why these particles are known as massless is due to the theoretical studies that have shown that the effective mass of the particles in the Dirac cone region approaches zero, and in the seminal study of Novoselov et al., they have observed the Dirac cone which proves evidence for the zero-mass interpretation but experimentally this is still a matter of confusion [44,45]. That study of Novoselov et al. was also very important since they have found a way of separating individual graphene planes by experimental means [45]. A material with such striking properties (like high electron mobility and very low resistivity at room temperature) has created the possibility of many novel applications [44–46].

The fact that silicon lies on the same column of the periodic table as carbon has previously evoked questions about whether possibility of a counterpart of graphene in terms of silicon can be possible or not [47]. Even though bulk form of silicon still maintains its importance in device applications, its 2D form, which is coined as silicene, has recently started to attract attention of the scientists in material science after the realization of its synthesis in Marseille (France) [48]. In this study, silicene was deposited on Ag(110) but at that time, these structures were named as silicon nanowires (SiNW) rather than as SiNRs since the hexagonal nature of the nanowire was not yet discovered (which has been shown in the STM images taken in their following studies which will be mentioned in the following sections). The same international group has been the leader of the studies conducted on silicene nanoribbons (SiNRs) since its birth and the same group studies SiNRs both experimentally and computationally. the electronic density.

In the second part of this section, experimental studies conducted on silicene nanoribbons in the recent years will be reviewed. Up to now, studies show that silicene synthesis has been accomplished by deposition on Ag(100), Ag(110) and Ag(111) surfaces and studies that have been carried out in these different surfaces will be given in different subsections. In the third part of this section, some of the many theoretical studies conducted in the field will be mentioned.

## 1.4.2 Experimental Studies on Silicene Nanoribbons

### 1.4.2.1 The Concept of Alloy Formation and Phase Separation

In order to understand deposition of Si atoms on Ag surfaces, which is actually the deposition of a semiconductor on metal, one has to understand the nature of metal deposition on other metals first. In order to make it easier, studies on two different metal-metal model systems, namely Ag/Cu(111) and Sb/Cu(111) systems have been analyzed [49].

During the dissolution of a thin film, deposition of metals on metals may lead to alloy formation. Alloy formation is affected by the interactions between substrate and deposit and the surface segregation tendency [50]. According to [49], most modern theories in the field explain that there are three driving forces that affect the surface segregation phenomenon:

(i) relative surface stress of pure elements
(ii) chemical interactions between substrate and deposit
(iii) size mismatch between substrate and deposit

The surface segregation leads to two different types of systems:

- *Phase separating system*: In this type of system, surface segregation leads to the formation at the surface of a pure plane of solute. Ag/Cu(111) metallic system is the model system representing this behavior [51,52].

- *Ordering system*: In this type of system, surface segregation leads to the formation of 2-D ordered surface alloys. Sb/Cu(111) metallic system is the model system representing this behavior [53,54].

In the case of metallic systems where metals are deposited on metals, crystallographic structural differences and the resulting chemical interactions do not have a crucial importance on the formation of the final structure since both the metal and the deposit is metal and they are similar in terms of these properties. Nevertheless, deposition of semiconductors on metal systems is a very different case since semiconductors and metals have very different crystallographic structures which result from the difference in the nature of bonding between the deposit and the substrate. In the literature, there are many studies that involve deposition of noble metals on semiconductor substrates [55-60] but the number of studies that are devoted to the deposition of semiconductors on metal surfaces is limited.

#### 1.4.2.2 Model systems describing Semiconductor Deposition on Metal Surfaces

Si/Cu(110) is the first system studied experimentally that can be given as an example to the deposition of a semiconductor on metal surface [61-63]. In these studies, Scanning Tunneling Microscopy (STM), Low Energy Electron Diffraction (LEED), and Photo-Electron Spectroscopy (PES) has been utilized to characterize the resulting Si/Cu(110) structures at different silicon coverages of 0.1 ML (indicating 1/10 of one monolayer of atoms), 0.5 ML, 0.55 ML and 0.8 ML and the images taken at these different coverages are given in the publication [64] by J.A. Martin-Gago et al. At 0.1 ML coverage, structured islands of Si can be observed whereas at 0.5 ML, the islands grow and coalesce to form extended alloy areas resulting in the final superstructure of c(2x2) surface alloy formed in substitutional Cu sites. Increasing the silicon coverage beyond 0.5 ML leads to the formation of linear atomic silicon chains on top of the surface alloy layer. This is a model system of a semiconductor on metal that shows alloy formation.

The prototype system of semiconductor on metal that shows phase separation is the Ge/Ag system due to the large surface segregation of germanium [49].

In the system of Ge/Ag(100), the dissolution kinetics of 1 ML coverage of Ag at three different temperatures: 250 C°, 264 C° and 320 C° have been studied in [65,66]. In their study, they have shown the variations of Ag and Ge in the surface with an Auger peak-to-peak intensity ratio versus time graph (Auger electron spectroscopy is a characterization technique that is used to obtain information about the outermost part of a material that is nearest to the surface). The results show that the behavior of this system resembles more to the behavior of metallic Sb/Cu system (the system that has tendency to order and to form surface alloy) than to that of metallic Ag/Cu system (the system that has tendency to phase separation) in terms of the dissolution kinetics: at first (at the beginning of annealing), a rapid dissolution is seen but then the dissolution speed lowers

down sharply to a plateau as shown in **Figure 1.1 b)**. However, despite the similarity in terms of the dissolution kinetics to the Sb/Cu model system, in terms of segregation, the system shows tendency towards phase separation at each of the temperatures given as the deposition continues with time.

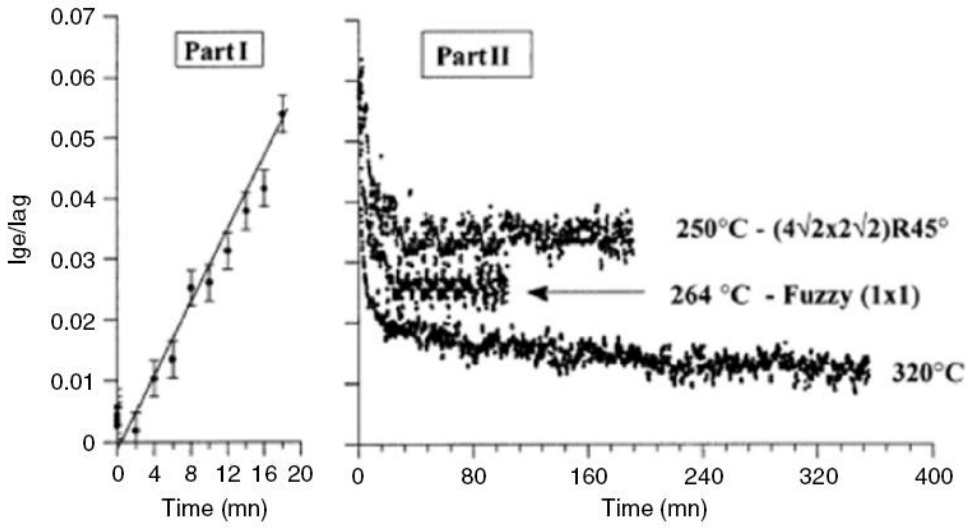


**Figure 1.1 a)** Deposition of Ge on Ag (100) at 1 ML, **b)** Dissolution kinetics in the bulk recorded at 250 C°, 264 C° and 320 C° just after deposition. Taken from [66].

In the system of Ge/Ag(110), which is studied by J. Dalmas et al. in [67], a c(4x2) superstructure is seen from the STM image as shown in **Figure 1.2**. In this study, the group has also obtained a LEED pattern which shows the presence of a c(4x2) superstructure seen in the STM image. **Figure 1.2** shows that segregation of Ge atoms leads to the phase separation by the help of which a perfect assembly of Ge atoms in a 2-D array is formed on the top of the Ag substrate. The studies made for the system of Ge/Ag(111) [68,69] show that at low coverages, the system forms an alloy of Ge atoms only with the outermost layer of Ag atoms (which has the c($\sqrt{3}$ x$\sqrt{3}$) superstructure) in contrast to the Ge/Ag(100) and Ge/Ag(110) systems where there is an obvious phase separation at the surface. But at higher coverages, as more Ge atoms are adsorbed on other Ge atoms, a superstructure c($\sqrt{3}$x 7) favoring phase separation starts to form and dominate the structure.

The comparison of Ge deposition on Ag structures of three different faces of low indices demonstrates the effect of Ge-Ge (deposit-deposit) covalent bonded interactions which tend favor phase separation and Ge-Ag (deposit-substrate) interactions which tend to favor the alloy formation on the final structure [49].

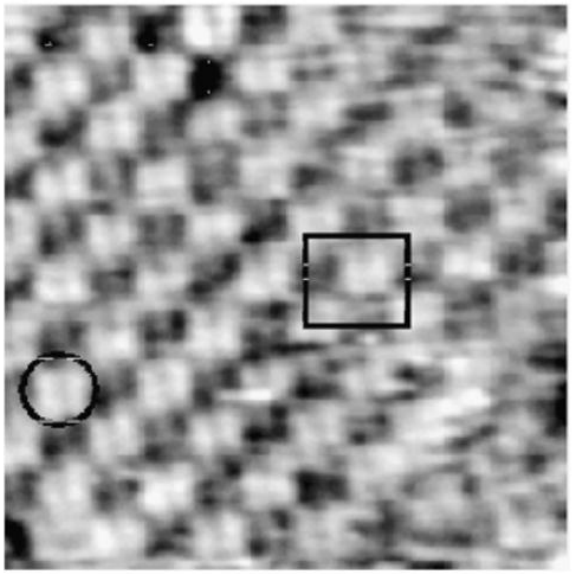

**Figure 1.2** Empty state STM image showing the perfect assembly of c(4x2) superstructure formed in a Ge/Ag(110) system. Taken from [67].

Similar to the Ge/Ag model system, Si/Ag system has a pronounced tendency towards phase separation [70-72]. Owing to this tendency towards phase separation, silicene nanoribbons could be formed on Ag substrates without any Ag impurity atoms. Deposition of Si atoms on different Ag substrates for the synthesis of silicene nanoribbons have been studied several times in the recent years by experimental means. In the following three subsections, experiments carried out on Si deposition on Ag(100), Ag(110) and Ag(111) will be reviewed.

#### 1.4.2.3 Silicene Nanoribbons on Ag(100) Surfaces

In the study conducted by Léandri et al. in 2007 [73], Si atoms are deposited on Ag(100) surface at 1 ML coverage which is heated to 230 C°. The STM image of

the final structure is shown at **Figure 1.3 a)**. In the STM image, there are two orthogonal domains which contain parallel Si stripes that are oriented either along [110] or the [-110] direction of the Ag surface and which are separated by border lines. In **Figure 1.3 b)**, a detailed image showing the parallel stripes at a higher magnification is given. In this figure, a rectangular unit cell that has sides of approximately 0.41 nm and 0.28 nm can be seen; in the unit cell, there are four protrusions that can be seen in height profiles (which can hardly be seen in Figure 1.3 b)). As shown in the figure, p(3x3) superstructure of Si formation occurs on the Ag surface layer.

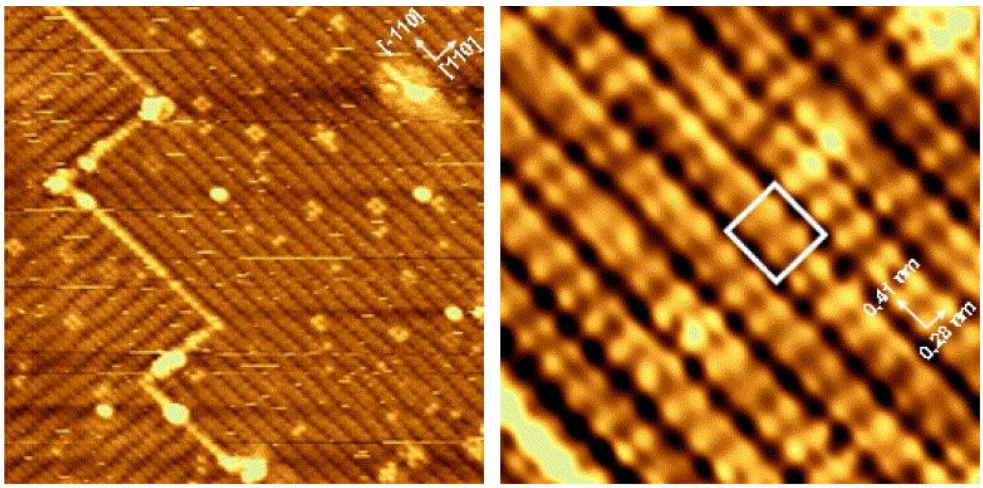


**Figure 1.3 a)** Filled state STM image of deposited Si on Ag (Left), **b)** Filled state STM image of the parallel stripes at one domain shown at a higher magnification (Right). In the images, the p(3x3) superstructure can be seen. Both images are taken from [73].

**Table 1.1** Atomic coordinates of the Si atoms of the p(3x3) superstructure. Taken from [73].The associated unit cell is (a=b=0.867 nm, c=0.409 nm, $\alpha = \beta = \gamma = 90°$).

| # | X | Y | Z |
|---|---|---|---|
| Si | 0.349 | 0.268 | 1.149 |
| Si | 0.315 | 0.512 | 0.903 |
| Si | 0.795 | 0.215 | 1.003 |
| Si | 0.840 | 0.467 | 0.833 |

When the coverage exceeds 1 ML, p(3x3) superstructure transforms into a combination of p(3x3) structure and the local p(7x4) superstructure as shown in **Figure 1.4 a)** which is a "complex" superstructure [73]. In **Figure 1.4 b)**, there is an atomic model proposed by Léandri et al. which is deduced from the observed structures. As can be noted from both the STM image and the model, there is a $7a_{Ag}$ periodicity in the width of the stripes of the SiNR whereas chains of the hexagons show the periodicity of $4a_{Ag}$ along the stripes.

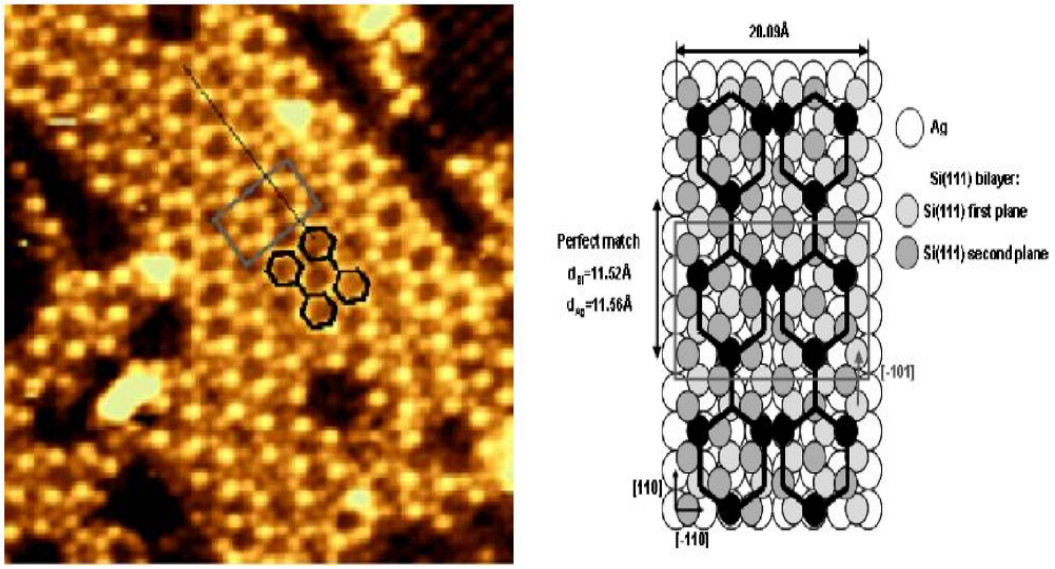


**Figure 1.4 a)** RT filled STM image (6.4 x 6.4 $nm^2$, V= - 1V, I = 1 nA) revealing the details of the ‘‘complex’’ structure: the local (7 x 4) unit cell is represented by the grey rectangle. The pattern of two joined chains of hexagons, describing the new stripes, is drawn in black. **b)** Tentative atomic model showing the stripes of the ‘‘complex’’ structure. White balls correspond to silver atoms, dark grey and light grey balls correspond to silicon atoms of the first and second silicon (111) bilayer; black balls point to silicon atoms sitting on top of silver atoms. The black pattern shows the two joined hexagon structure revealed by STM. Both images are taken from [73].

For the silicon adsorption on Ag(100) surfaces, the atomic model for the p(3x3) reconstruction at lower coverages (up to 1 ML) which has been put forward by Léandri et al. has been questioned in a Density Functional Theory (DFT) study by Guo-min He [74]. In this study, it is asserted that rather than the model that encompasses 1-D chains of four silicon atoms (tetramers) that has been adsorbed near hollow and bridge sites of the topmost Ag (100) surface layer, the model with a hexagonal atomic geometry at 1 ML coverage describes the geometry of the initial p(3x3) superstructure better since the primary model has instability issues [74].

In the same study, He has also considered the local p(7x4) superstructure proposed by Léandri et al. His calculations showed that a silicene-like layer with additional Si atoms located on the top of the already formed silicene-like layer is the most favorable structure as shown in **Figure 1.5**. In the figure, the grey balls represent the Ag atoms in the Ag (100) substrate layer; the blue balls represent the first layer of silicon atoms that form a silicene-like structure made up of hexagons whereas the red atoms are the extra Si atoms located on the top of other Si atoms.

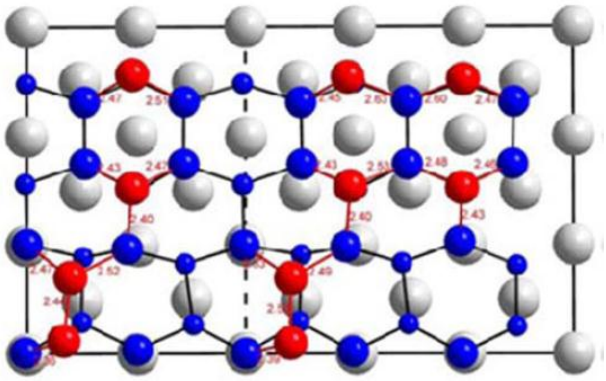

**Figure 1.5** Top view of the atomic model proposed by He for this ‘‘complex’’ structure; blue balls: Si atoms in the silicene-like layer, red balls: Si adatoms on top, white balls: Ag atoms of the Ag(1 0 0) surface. Taken from [74].

### 1.4.2.4 Silicene Nanoribbons on Ag(110) Surfaces

In [48], Léandri et al. reported the first synthesis of silicene on Ag(110) surfaces but as mentioned before, they did not use the name “silicene” for the resulting structure in that paper, they rather called these silicon deposits as silicon nanowires (SiNWs) since their first characterization results did not show any signs of a hexagonal structure. They have deposited silicon atoms of approximately 0.25 ML on a clean, nominally flat Ag(110) surface under ultra-high vacuum (UHV) conditions. They have made the characterization of the resulting structure by using STM images and obtaining LEED patterns of the structure. In **Figure 1.6 a)** and **Figure 1.6 b)**, two STM images at different resolutions of approximately 0.25 ML of Si deposited on Ag(110) at room temperature is shown.

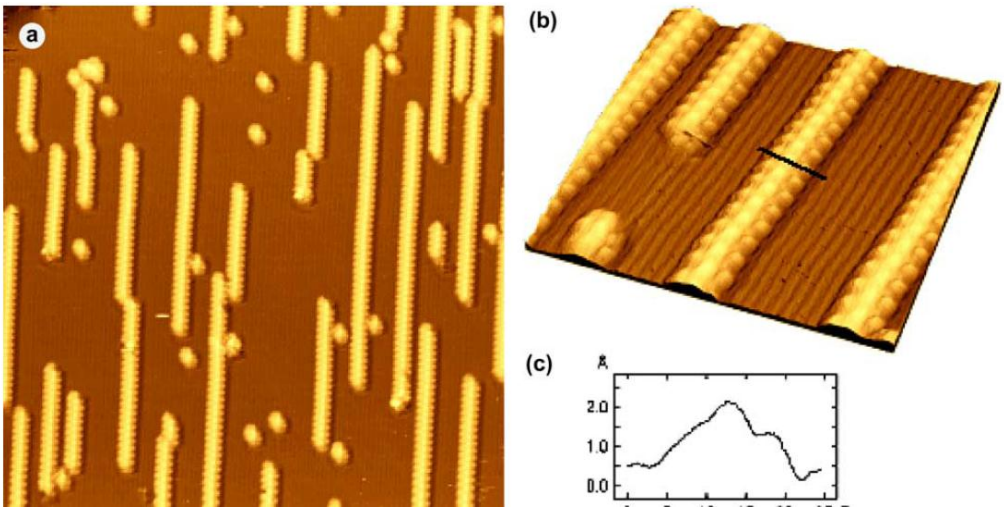


**Figure 1.6 a)** 42 x 42 $nm^2$ overview with Si nanowires and Si nanodots, **b)** 12.1 x 12.1 $nm^2$ zoom on the same structure shown at a, **c)** height profile along the black line in b). Taken from [48].

In their paper, the authors of [48] describe this initially deposited silicon structure as a SiNW of length that can go up to 30 nm with the aid of the self-assembly of silicon nanodots which can also be noticed in **Figure 1.6 a)**. In **Figure 1.6 b)**, it can be seen that these NWs are perfectly aligned along the [-110] direction on Ag(110) surface and they do not have a planar structure when adsorbed on Ag(110) surface, they rather have rounded protrusions which have a periodic distribution of $2a_2$ (which is equal to 0.577 nm) as can be seen from the same figure. Besides, the SiNWs (as they named it) have a definite same width of 1.6 nm which corresponds to four silver atomic distances ($4a_1$) along the direction of Ag[001] and a height of approximately 0.2 nm [48]. It should also be taken into consideration that in **Figure 1.6 c)**, the height profile indicates the asymmetry in height along the line perpendicular to the SiNW length. As will be mentioned in the following paragraphs, in a more detailed study [76], they have made further attempts to enlighten the reasons behind the formation of asymmetric height profile perpendicular to the direction of growth (namely [100] direction).

After annealing at 230 C° for about 10 nm, the authors of [48] found out that the silicon nanodots that were in the STM images that are taken before annealing which are seen in **Figure 1.6 a)** and **Figure 1.7 a)** disappear as shown in **Figure 1.7 b)**. In [49], this is considered as an evident consequence of 1-D diffusion of the silicon nanodots that only occur along [-110] direction, not in the perpendicular [100] direction which is shown with a black line in **Figure 1.6 b)**. This behavior of SiNW growth towards [-110] direction is also confirmed by a similar study in which the silicon growth on Ag(110) at 200 °C is studied under ultrahigh vacuum and both the STM images and the LEED patterns of the resulting structures indicate the presence of 5 x 2 periodicity in 1-D SiNWs as shown in **Figure 1.8** [75].

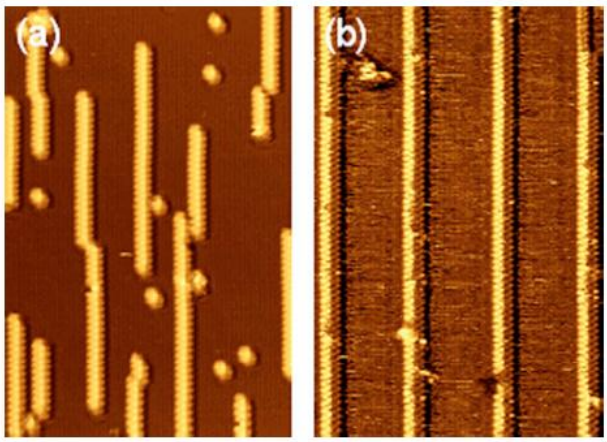


**Figure 1.7** STM images (24.3 x 36.1 $nm^2$) of a low coverage of Si deposited at RT on a Ag(110) surface. **a)** Before annealing; V=−1.7 V filled states, $I_t$=1.1 nA, **b)** After annealing at 230 °C. V=−0.4 V, $I_t$=0.7 nA. Taken from [48].

A more detailed analysis of the SiNW structures deposited on Ag(110) has been made by De Padova et al. in [76]. In their previous studies [48,75], presence of an asymmetry in the height profile along the [100] direction was shown and in this study, the group elaborated on the details of the structures that they have obtained. In **Figure 1.9**, a 3D view of a previous STM image is shown where a dip is noticeable on the right side of the SiNW whereas on other images in the same study [76] or previous studies [48, 75], the same dip formation occurred on the left side of the

SiNW. While this effect could be attributed to an artifact caused by the scanning tip of the STM equipment, the authors tried to describe this situation with an analogy of magnetism (a magnetic spin analogy), where these different symmetry breaking NWs are considered as different "magnetic-like" domains of opposite "spins" which can be considered as a chiral coupling between right handed SiNRs and left handed SiNRs. The two different so-called "spins" are shown in **Figure 1.9**.

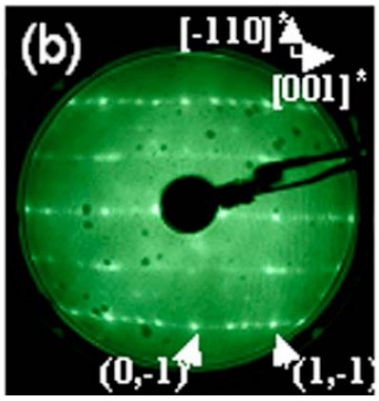


**Figure 1.8** 5 x 2 LEED pattern taken at 68 eV primary energy. Taken from [75].

Until more detailed experimental studies with STM equipment that have higher viewing capabilities and resolution are employed to shed light on the internal structure of these so-called SiNWs, the very fact that these structures should be termed as silicene nanoribbons (SiNRs) rather than SiNWs could not be comprehended. In their seminal paper, B. Aufray et al. have shown that the actual geometry of the final structure possesses hexagons which can easily be seen on the STM image obtained [77]. The black line in **Figure 1.10 a)** marks the hexagons noticed in the structure. They have also performed ab-initio DFT calculations in order to compare the findings which are shown in **Figure 1.10 b)** and **Figure 11** with the experimental results. In the theoretical part of their study, they have tried to examine the detailed structure of the SiNR and the substrate and looking at the side view of the final relaxed structure (shown in **Figure 1.11 a)**), they found out that the

Si atoms do not reside at the same height and they rather form an arc with a height of 2.06 $\dot{A}$ which has a perfect agreement with the experimentally observed height of $2\dot{A}$.

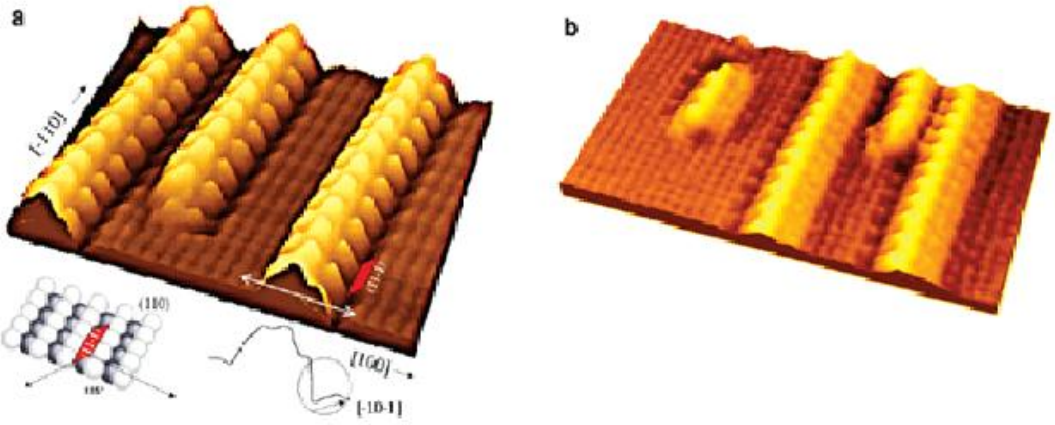


**Figure 1.9 a)** 3D view of 10.2 x 10.2 $nm^2$ filled-states STM image: dip asymmetry at right-side. **b)** 3D view of 10.2 x 10.2 $nm^2$ filled-states STM image: dip asymmetry at left-side.Taken from [76].

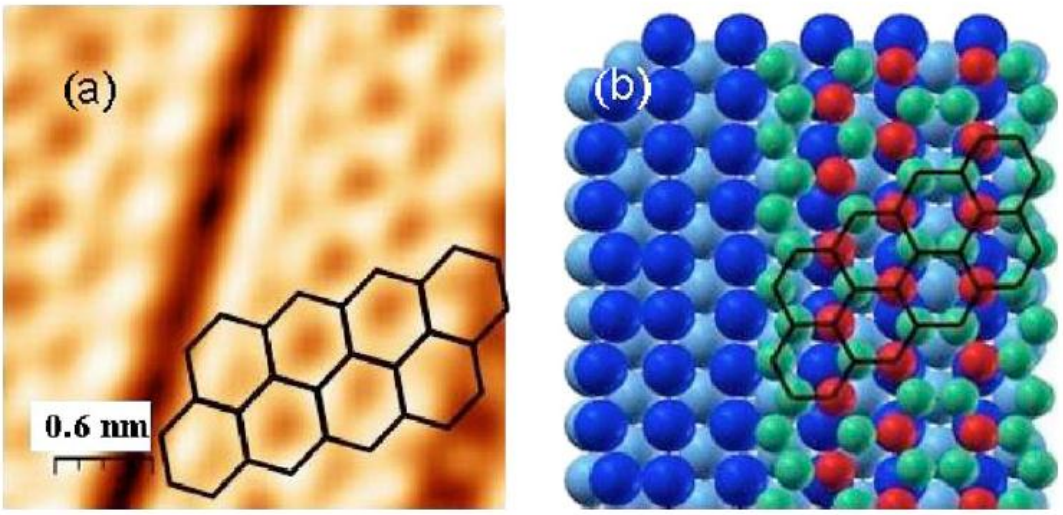


**Figure 1.10** Details of the atomic structure of silicon NRs: **a)** high resolution filled state STM image revealing honeycomb arrangement (few honeycombs are drawn on the image); **b)** ball model of the corresponding calculated atomic structure (large dark balls (blue)) representing Ag atoms in the first layer; top most Si atoms are represented by small dark balls (red) while others represented by light small balls (green), the whole forming hexagons (highlighted on the silicon NR). Taken from [77].

In the theoretical study made by A. Kara et al. in [78], they state that the asymmetry seen in the height of the SiNR structure along the [100] direction is reflected in the electronic structure of the system based on the energy density profile that has been obtained from the ab-initio calculations of [77] (shown in **Figure 1.11 b)**). The arc (of 2.06 $\dot{A}$ height) mentioned in the previous paragraph is also found in this study (which is shown in **Figure 1.12**) [78]. This arc-shaped structure is made up of silicon atoms that have entered into the channels of Ag(110) (apparently without forming an alloy) so that it would provide a better grip of Si atoms to the substrate surface and a bump due to the Ag layers under the SiNR. The dips which have been noticed at the edges of the SiNRs in previous publications mentioned [48,75,76,77] are called as “gutters” by the authors of [78] and based on the energy profiles at the location of these gutters, the authors have attempted to explain the nature of the extreme anisotropic SiNR growth along the [-110] direction: according to them, it

can be argued that Si atoms either directly coming from the gas phase or diffusing within the SiNR arrives at the ribbon edge and then moves to the end of the SiNR, thereby contributing to the elongation of the SiNR. According to the authors, the so-called gutter effect is the primary responsible factor in the formation of very long SiNRs [78]. Even though this explanation seems very satisfactory for describing the elongation of SiNRs, it still cannot explain why the SiNRs always have a magic width of 1.6 nm as shown in the experimental studies in the recent years [48,75,76,77].

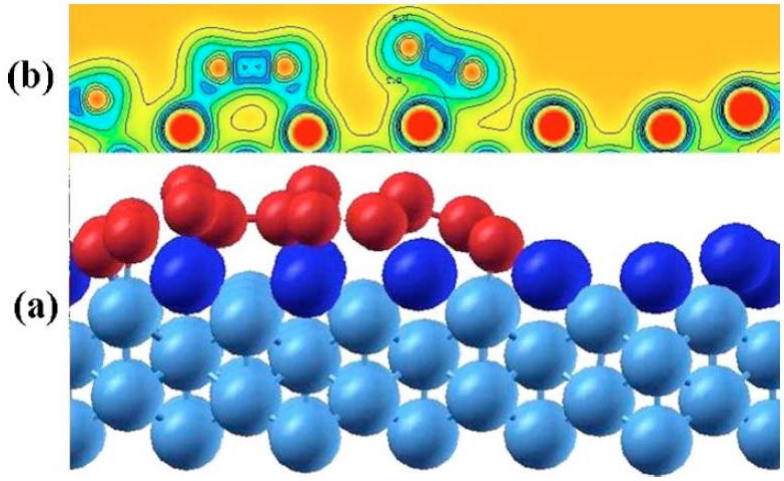


**Figure 1.11** Calculated atomic and electronic structures of graphene-like silicon NRs: a) ball model in cross section (large dark balls (blue): first layer Ag atoms and Si atoms are small dark balls (red)); (b) charge density in cross section. Taken from [77].

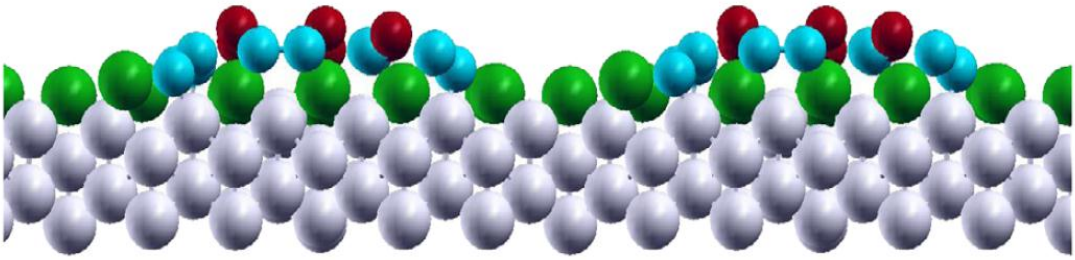

**Figure 1.12** Side view of SiNRs on Ag(110) showing the arched structure of the ribbons. Grey balls represent bulk Ag atoms; green balls represent surface Ag atoms; light blue balls represent first layer of Si atoms; red balls represent Si atoms on top of other Si atoms. Taken from [78].

#### 1.4.2.5 Silicene Nanoribbons on Ag(111) Surfaces

As shown in the STM images in **Figure 1.13** [79], the deposition of 1 ML of silicon on the Ag(111) substrate which is held at a temperature of 250 °C under UHV conditions was shown to produce a highly ordered epitaxial honeycomb silicene structure.

In [79], the authors mention the fact that extreme caution should be taken during the experiment to keep the temperature of the substrate between 220°C and 250°C and besides, the rate of silicon deposition should never exceed 0.1 ML per minute. In addition to this, they strictly assert that adjustment of the amount of silicon required to produce a single monolayer is very crucial for the success of the experiment.

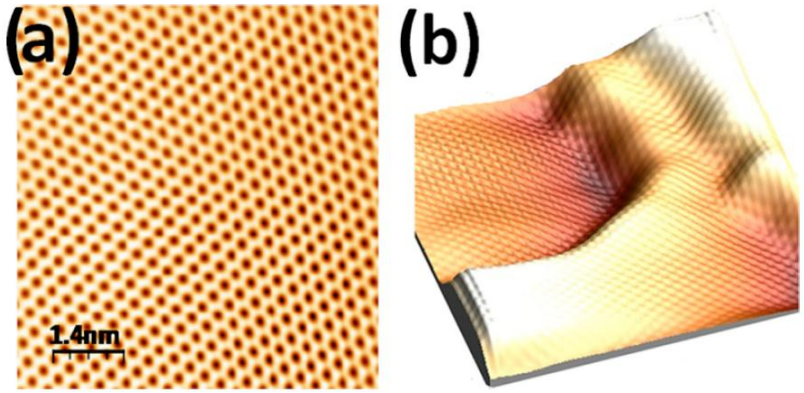


**Figure 1.13 a)** Large-scale, filled-state STM image showing the graphene like structure of one monolayer of silicon deposited on a close packed silver surface, Ag(111). **b)** 3D STM image showing Ag(111) steps covered by the silicene film (11x11 $nm^2$). Taken from [79].

#### 1.4.2.6 Oxidation Studies on SiNRs

In many areas of physics and technology, the oxidation of silicon has always had a great deal of importance because in microelectronics devices, the interface between silicon and silicon dioxide plays an important role. Now, in the era of nanotechnology, where the devices of microelectronics have been sized down to smaller and smaller scales, this role has become more and more pronounced than before [80]. The attempts to analyze the oxidation in SiNRs will be discussed in this section.

In the articles by De Padova et al. [81,82] and Kara et al. [83] the oxidation process of SiNRs have been coined as “burning match oxidation mechanism” of SiNRs. They have described this behavior like a propagating flame front where there is a strong resistance towards oxidation at the edges of the SiNR unlike graphene which shows strong edge reactivity. Oxidation occurs but it happens very slowly towards one dimension.

In [81], the authors have started their studies by synthesizing SiNRs on the top of Ag(110) surface layer in a massively parallel fashion as described in [48,75] and characterizing them by scanning tunneling microscopy/spectroscopy (STM/STS) and high resolution (HR) Si 2p core-level photoelectron spectroscopy (PES) under UHV conditions. After synthesis and characterization, the SiNR on Ag(110) is exposed to increasing doses of oxygen. At the beginning of oxygen adsorption, the oxidation process occurs only at the SiNW edges. Then, at higher doses, this process develops like a burning match along the [-110] direction, keeping the one dimensional orientation of the NWs as shown in **Figure 1.14**. In addition to this, the presence of several oxidation states is shown with the aid of 2p core-level PES measurements.

De Padova et al. has then concentrated on their attempts in tuning the oxidation properties of SiNR structures by intentionally creating local surface defects on their structures by $Ar^+$ sputtering [82] since oxidation of SiNR starts at very high oxygen exposure values. In this study, they have found that in order to initiate oxidation of a silicene grating, an oxygen exposure of 1000 L should be attained. But after $Ar^+$ sputtering, SiNR exhibits all the oxidation states as shown in **Figure 1.15** which shows the 2p core level PES results at 80L of oxygen exposure. This property of SiNRs enables the silicene gratings and possibly SiNR sheets to be used for future nanometric devices [83].

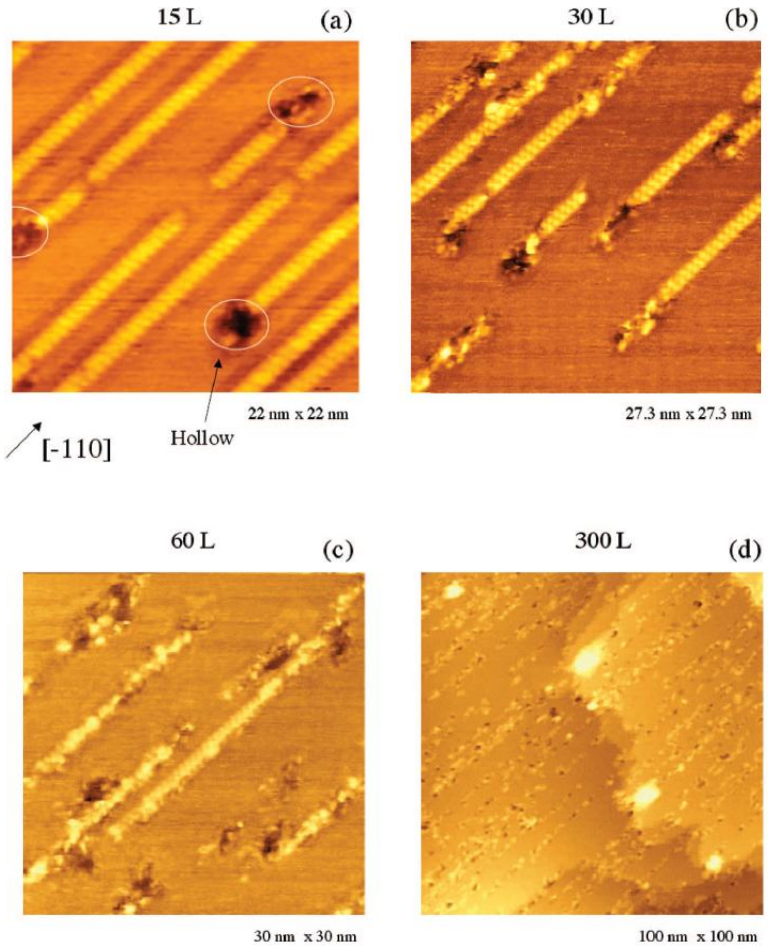


**Figure 1.14** Filled-states STM images of Si NWs on Ag(110) at different oxygen doses. **a)** 22 × 22 $nm^2$ at 15 *L*. **b)** 27.3 × 27.3 $nm^2$ at 30 *L*. **c)** 30 × 30 $nm^2$ at 60 *L*. **d)** 100 × 100 $nm^2$ at 300 *L*. Taken from [81].

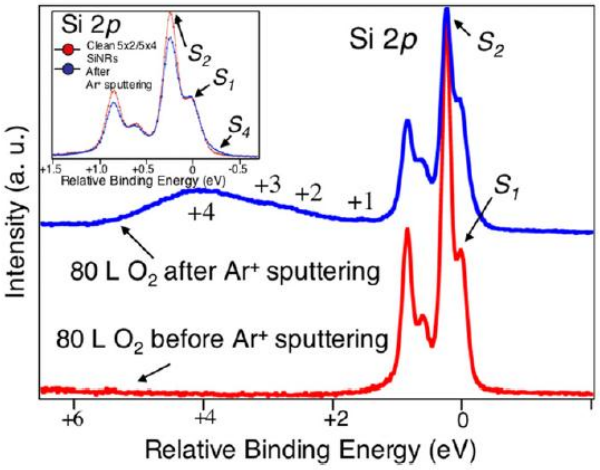


**Figure 1.15** Si 2p core level spectrum of the silicene grating with 80 *L* of oxygen exposure, before and after Ar+ sputtering. Inset: Si 2p spectra before (clean spectrum) and after Ar+ sputtering. Taken from [82].

### 1.4.3 Theoretical Studies on Silicene Nanoribbons

As previously discussed in **Section 1.4.1.4**, He applied Density Functional Theory (DFT) to study silicene growth via Si adsorption on Ag(110) surface with the Alder-Ceperley form of Local Density Approximation (LDA) as the exchange-correlation functional [74]. This study was divided into two parts. In the first part, He has studied eight several Si coverages ranging from 0.25 ML to 2 ML for several different Si configurations in order to find the configuration with the lowest energy at all coverages. In the second part, He used a larger unit cell (2 x 5) to consider many different atomic arrangements. The results of this study show that at low Si coverage, the Si-Ag bonds are slightly more favorable than the Si-Si bonds and there exists an attractive interaction between the Si adatoms. At high Si coverages, the Si-Si bond structure with proper arrangement becomes energetically more favorable because of the weakening of the Si-Ag bonds and the attractive interaction between the Si adatoms. His calculations showed that a silicene-like layer with additional Si atoms

located on the top of the already formed silicene-like layer is the most favorable structure as shown in **Figure 1.5**.

Cahangirov et al. have published on of the most important papers in the field of theoretical silicene studies [84]. Different from He's study [74], Cahangirov et al. studied free standing (standalone) silicene and germanene (which is the 2-D hexagonal ribbon structure made up of Ge atoms) using Density Functional Theory. They have studied three different honeycomb structures of silicene which are mainly planar (PL), low-buckled (LB) (the buckling distance, $\Delta = 0.44\ \dot{A}$) and high-buckled (HB) ($\Delta = 2.0\ \dot{A}$) silicene structures. They have made structural optimization for these structures and then they have obtained energy bands, density of states and phonon dispersion graphs for these different structures. They have found that planar SiNR sheets are slightly unstable when compared to the other two structures and low buckled (LB) configuration shows the most stable structure as shown in **Figure 1.16**. In addition to this, they have also found that similar to graphene, the charge carriers of these puckered structures can behave like massless Dirac fermions due to their $\pi$ and $\pi^*$ bands which are crossed linearly at the Fermi level [84].

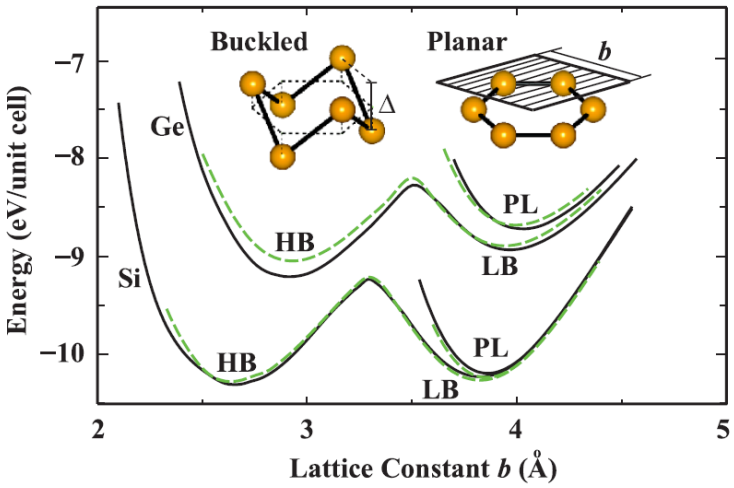


**Figure 1.16** Energy versus hexagonal lattice constant of 2D Si and Ge are calculated for various honeycomb structures. Black (dark) and dashed green (dashed light) curves of energy are calculated by LDA using PAW potential and ultrasoft pseudopotentials, respectively. Planar and buckled geometries together with buckling distance Δ and lattice constant of the hexagonal primitive unit cell, b are shown by inset. Taken from [84].

Theoretical studies by Topsakal and Ciraci [85] has focused on magnetic and electronic properties of silicene nanoribbons (SiNRs) by performing DFT calculations on these honeycomb structures along with two other crucial 2-D honeycomb structures; graphene and boron nitride under uniaxial tension. Primarily, they have calculated elastic constants of the zigzag and armchair edged forms of these materials. A density of states (DOS) analysis reveals that armchair nanoribbons of these materials have zero band gaps under strain, so the massless Dirac fermion behavior can be attained in a semiconducting nanoribbon [85]. Under plastic deformation, honeycomb structures are shown to change irreversibly in a very few steps of strain application. They have found that the plastic deformation of these materials leads to the formation of suspended atomic chains.

Song et al. [86] have investigated the electronic properties of zigzag and armchair SiNR structures with H-terminated and bare forms by DFT calculations. In

this study, they have concentrated on the effects of edge shape (zigzag or armchair models) and width on the structural and electronic properties of SiNRs. They have found that Si-H bond is always 1.50 Å in all models, but the Si-Si bonds on the edge are contracted upon relaxation. Their findings show that in H-terminated zigzag models, direct band gaps of shorter width models are very small and band gap becomes zero as the width increases whereas H-terminated armchair models are shown to be semiconductors. In another study, the same group has investigated the electronic and magnetic properties of SiNRs with monovacancy or a divacancy. They have found that the presence of either a monovacancy or a parallel oriented divacancy converts an armchair direct semiconductor SiNR to an indirect semiconductor, while the presence of a divacancy in a SiNR sheet with a slanting orientation alters the character of the nanoribbon to a metallic one. Their investigation on the magnetic properties of SiNRs shows that adding any type of these vacancies to the nonmagnetic armchair SiNR does not render it magnetic [87].

Dzade et al. have investigated the possibility of incorporating many different transition metals into SiNRs such as Ti, Nb, Ta, Cr, Mo and W and they also have studied the magnetic properties of $CrSi_2$ [88] which is shown to form a 2D magnet exhibiting a strong piezomagnetic coupling.

Given that carbon materials are not compatible with the present MEMS technology, the possibility of replacing conventional MEMS technology with silicon based nanotechnology will surely call the attention of the electronics industry towards the research of silicene as an exciting promise of prolonging the validity of Moore's Law [82]. Potential future applications of SiNR honeycomb structure encompass a wide range of applications from the future emergence of the silicon based nanotechnology to the ultrasensitive chemical sensors coined as electronic noses, biological and cancer markers, improvement of the solar cell technology, and the field of fuel cells, namely hydrogen storage all of which underlines the value of this new golden material [82].

# CHAPTER II

# METHOD OF CALCULATION

## 2.1 The Theory Underlying Molecular Dynamics Simulation

### 2.1.1 Formulating the Problem: Origins of Molecular Dynamics in Classical Mechanics

#### 2.1.1.1 Newton's Laws of Motion

As mentioned in **Section 1.2.2**, computational research methods in nanotechnology provides an alternative way of research for scientists by enabling them to make calculations of the properties of nanomaterials rather than directly synthesizing them and observing their properties by measurements. Classical molecular dynamics simulation technique takes Newton's laws of motion as a basis and with the help of these fundamental classical laws, the MD simulation software determines future positions of a system of atoms or molecules, the forces that act on the particles in this system and energies of these particles.

In 1687, the famous physicist and mathematician Sir Isaac Newton published his groundbreaking book *Philosophiae Naturalis Principia Mathematica*, in which the three fundamental laws of classical motion are stated. These laws are basically;

1. When there are no external forces, a body will either be at rest or move along a straight line with a constant velocity v.

2. The action of an external force F on a body produces an acceleration aequal to the force divided by the mass m of the body:

$$\mathbf{a} = \frac{\mathbf{F}}{\mathrm{m}} \qquad \mathbf{F} = \mathrm{m}\mathbf{a} \tag{2.1}$$

3. If body A exerts a force on body B, then body B exerts an equal and opposite force on body A. That is, if $\mathbf{F}_{AB}$ is the force body A exerts on body B, then the force $\mathbf{F}_{BA}$ exerted by body B on body A satisfies

$$\mathbf{F_{AB}} = -\mathbf{F_{BA}} \tag{2.2}$$

The derivative operation in mathematics shows the change in a quantity with respect to the change of some other quantity. Considering that velocity v(t) of a particle is defined as the change of that particle's position r(t) with respect to time and acceleration a(t) is defined as the change of that particle's velocity with respect to time, it is easy to show that.

$$\mathbf{v}(\mathrm{t}) = \frac{\mathrm{d}\mathbf{r}}{\mathrm{dt}} \tag{2.3}$$

$$\mathbf{a}(\mathrm{t}) = \frac{\mathrm{d}\mathbf{v}}{\mathrm{dt}} = \frac{\mathrm{d}^2\mathbf{r}}{\mathrm{dt}^2} \tag{2.4}$$

Here, the particle's position **r**(t) is known as the trajectory of the particle which is a function of time. Trajectory is a vector combination of three dimensional position functions x(t), y(t) and z(t) if the vectors are given in Cartesian coordinates [90,91].

Having defined acceleration in terms of trajectory in Eq. 2.4, it would be more useful to use the Newton's second law according to this definition.

$$\mathbf{F} = \mathrm{m}\frac{\mathrm{d}^2\mathbf{r}}{\mathrm{dt}^2} \tag{2.5}$$

In this form, the second law of Newton has included the first law as well. In other words, when there are no external forces, the second derivative of trajectory in Eq. 2.5 with respect to time is zero and this can only be possible if the velocity is either constant or zero. This is the equation of motion which is solved every time separately for each particle in one step of a molecular dynamics simulation run.

### 2.1.1.2 The Phase Space

In order to visualize the classical motion, positions and velocities or positions and momenta are can be drawn on the same graph. As mentioned, sometimes momenta can be utilized in lieu of velocities due to the reasons that will be mentioned in the following sections. Particle momenta in Cartesian coordinates are related to the velocities by Eq. 2.6.

$$\mathbf{p}_i = m_i \mathbf{v}_i = m_i * \frac{d\mathbf{r}}{dt} \tag{2.6}$$

Hence, the classical motion of an N-particle system can be described by specifying the full set of 6N functions, $\{\boldsymbol{r}_1(t), ..., \boldsymbol{r}_N(t), \boldsymbol{p}_1(t), ..., \boldsymbol{p}_N(t)\}$. At any instant t in time, all of the information about the system is specified by 6N numbers (or 2dN in d dimensions). These 6N numbers can be considered as a single point in a 6N-dimensional space called "**phase space**". A general point in the phase space as given in Eq. 2.7 is also known as the phase space vector [90].

$$x = (\mathbf{r}_1, ...\mathbf{r}_N, \mathbf{p}_1, ..., \mathbf{p}_N) \tag{2.7}$$

### 2.1.1.3 Lagrangian and Hamiltonian Formalisms

The straightforward formation of equation of motion given in Eq. 2.5 is also called as Newtonian formalism. Due to the fact that phase space describes the system in terms of position-momenta or position-velocities, it is natural to seek for an algebraic description of a system in terms of position-momentum or position-velocity variables. In fact, what is necessary here is a "generator" or an "operator" that takes

these variables as inputs and produces an equation of motion. Here, the formal structure sought is embodied in the Lagrangian and Hamiltonian formalisms.

Lagrangian operator $\mathcal{L}$ is defined as the difference between kinetic and potential energies expressed in terms of positions and velocities as given in Eq 2.8. Here (and also in the rest of this thesis), dot notation$\dot{r}_1$ and$\ddot{r}_i$ is employed to represent velocity and acceleration of a single particle respectively.

$$\mathcal{L}(\mathrm{r}_1, \mathrm{r}_2, \ldots\ldots\ldots \mathrm{r}_\mathrm{N}, \dot{\mathrm{r}}_1, \dot{\mathrm{r}}_2 \ldots\ldots \dot{\mathrm{r}}_\mathrm{N}) = \mathrm{K}(\dot{\mathrm{r}}_1, \dot{\mathrm{r}}_2 \ldots\ldots \dot{\mathrm{r}}_\mathrm{N}) - \mathrm{U}(\mathrm{r}_1, \mathrm{r}_2, \ldots\ldots\ldots \mathrm{r}_\mathrm{N}) \quad (2.8)$$

where the kinetic energy is given by Eq. 2.9.

$$\mathrm{K}(\dot{\mathrm{r}}_1, \dot{\mathrm{r}}_2 \ldots\ldots \dot{\mathrm{r}}_\mathrm{N}) = \frac{1}{2}\sum_{\mathrm{i}=1}^{\mathrm{N}} \mathrm{m_i}\dot{\mathrm{r}}_\mathrm{i}^2 \quad (2.9)$$

$$\frac{\partial \mathcal{L}}{\partial \dot{\mathrm{r}}_\mathrm{i}} - \frac{\mathrm{d}}{\mathrm{dt}}\left(\frac{\partial \mathcal{L}}{\partial \mathrm{r}_\mathrm{i}}\right) = 0 \quad (2.10)$$

The Lagrangian operator serves as a generator through the Euler-Lagrange equation given in Eq. 2.10. When the forces are conservative, the right side of Eq. 2.10 is zero. In Lagrangian formalism, the forces are conservative. In other cases like introduction of $N_c$ constraint conditions to the system, right side of Eq. 2.10 becomes non-zero and it has to be modified according to the applied constraint condition.

Substituting Eq. 2.9 into Eq. 2.10, one derives Eq. 2.11 and Eq. 2.12

$$\frac{\partial \mathcal{L}}{\partial \dot{\mathrm{r}}_\mathrm{i}} = \mathrm{m_i}\dot{\mathrm{r}}_\mathrm{i} \quad (2.11)$$

$$\frac{\mathrm{d}}{\mathrm{dt}}\left(\frac{\partial \mathcal{L}}{\partial \mathrm{r}_\mathrm{i}}\right) = \mathrm{m_i}\ddot{\mathrm{r}}_\mathrm{i} \quad (2.12)$$

The strength of the Lagrangian formalism lies in the fact that the equations of motion can be written in an arbitrary coordinate system, which might not be easy to write down directly from Newton's second law and these equations can be derived straightforwardly via the Euler–Lagrange equation. Lagrangian formulation of

classical mechanics is based on Euler–Lagrange (Newton) equations of motion, which represent a system of 3N second order differential equations, written for a set of variables that describe the position of a physical system of interest where N represents the number of particles in the system.

An alternative way to formulate the problem of particle motion is the Hamiltonian formulation that presents an equivalent description of particle motion in terms of 6N first-order equations written for independent variables describing the position and velocity of the system [91]. It is possible to derive Hamiltonian equations from Lagrangian equations using various differential calculus principles like reduction of order and change of variables and techniques likes Legendre transform. A very basic form of the Hamiltonian operator is given in Eq. 2.13. Hamiltonian operator is comprised of two parts: first part on the right side is the kinetic energy part that represents energy of the particles due to the motion and the second part on the right side is the potential energy that represents the interaction between different particles in the system. In empirical molecular dynamics simulation technique, this part is approximated by empirical potentials which will be discussed in **Section 2.1.3.2.** Eq. 2.13 and the following equations, $\mathbf{q}_1$,.....$\mathbf{q}_N$ represent the transformed coordinates from Cartesian coordinates $\mathbf{r}_1$,.....$\mathbf{r}_N$ and $\mathbf{p}_1$,.....$\mathbf{p}_N$ are the momenta of these N particles.

$$\mathcal{H}(q_1, \ldots . q_{3N}) = \sum_{i=1}^{N} \frac{p_i^2}{2m_i} + U(r_1, \ldots . r_{3N}) \tag{2.13}$$

$$\dot{q}_\alpha = \frac{\partial \mathcal{H}}{\partial p_\alpha} \tag{2.14}$$

$$\dot{p}_\alpha = - \frac{\partial \mathcal{H}}{\partial q_\alpha} \tag{2.15}$$

Given the Hamiltonian, the equation of motion for the system can be derived as given in Eq. 2.14 and 2.15. It should be noted that the total Hamiltonian is

conserved (i.e. the total energy is conserved which is in fact the first law of thermodynamics).

Newtonian, Lagrangian and Hamiltonian formulations of equation of motion are different ways of formulating the problem of motion at the microscopic scale. As mentioned before, molecular dynamics is a technique based on solutions of equation of motion for each single atom and at the first sight, it seems impossible to obtain any macroscopic property given that one mole of atom contains Avogadro's number of particles ($N_A$=6.02*$10^{23}$) since with the present computational technology, it is not possible for any computer (or a cluster) to solve that number of differential equations. At this point, statistical mechanics (or statistical thermodynamics) comes into play and establishes the link between microscopic and macroscopic properties, so that an appropriate formulation of the solution becomes possible.

## 2.1.2 Formulating the Solution: Use of Statistical Mechanics in Molecular Dynamics

### 2.1.2.1 The Ensemble Method

As mentioned in the previous section, in order to predict any macroscopic observable, only a very large quantity of microscopic information may seem to be sufficient, but, in fact, lesser amount of information is enough owing to the fact that many microscopic configurations of a system lead to the same macroscopic properties. For instance, if the temperature of a system is related to an average of the kinetic energy of the individual particles that constitute the system, then there are many ways to assign the velocities of the particles consistent with a given total energy such that the same total kinetic energy and, therefore, the same temperature is obtained. However, each assignment corresponds to a different point in phase space and, hence, a different and unique microscopic state. If one starts with a set of points in phase space which are drawn from a thermodynamic equilibrium state as initial conditions and then launches a trajectory from each of these initial points in phase space, the resulting trajectories would all be unique in phase space. These similar trajectories lead to the same macroscopic dynamical observables in the long time

limit. One of the most important scientists that have laid the fundamental foundations of classical and statistical thermodynamics, J.W. Gibbs formed the basis of the ensemble concept upon this idea in 19$^{th}$ century. The content of this paragraph may be summarized as ergodic theory [90].

Ensemble method is a statistical procedure for calculating thermodynamic properties of a system by using an ensemble which is a collection of systems expressed by the same set of microscopic interactions that share a common set of macroscopic properties [90]. In other words, ensemble is a theoretical collection of a very large number of small systems each of which replicates the macroscopic thermodynamic system that is being studied [92]. In epitome, ensembles link the microscopic world of motion of individual atoms or molecules and their trajectories to the macroscopic properties of the system like internal energy, Gibbs free energy or entropy. This connection is given in Eq. 2.16 regardless of the type of ensemble. Here, $\alpha$ represents the microscopic phase function which may represent any thermodynamic property at microscopic scale, Z represents the number of members in the ensemble and A is the macroscopic equilibrium observable obtained by this statistical averaging procedure.

$$A =< a(x_\lambda) >= \frac{1}{Z}\sum_{\lambda=1}^{Z} a(x_\lambda) \tag{2.16}$$

In order to utilize Eq. 2.16, a general form for the microscopic phase function $a(x_\lambda)$ suitable for any type of ensemble should be put forward first so that Eq. 2.16 becomes a useful relationship in establishing the link between microscopic and macroscopic worlds.

A collection of microscopic states (i.e. microstates) moves through space and each point in this phase space evolves through time according to its respective trajectory (motion under the effect of a Hamiltonian). At any point in time, these points represent a volume in space and according to the Liouville's theorem; the amount of this volume is always constant. The collection of points will have different

distorted shapes due to the highly nonlinear and chaotic nature of dynamics; nevertheless the volume is conserved throughout time. This proves that Eq. 2.16 is applicable, in other words, ensemble averages can be performed at any point in time.

As mentioned before, an ensemble contains the microstates consistent with a given set of macroscopic observables but the distribution of these microstates within the phase space volume is not homogenous (for most of the time) and this distribution affects the way these microscopic properties are added. The function that gives this distribution is called as the phase space distribution function $f(x,t)$ given in Eq. 2.17. Summing up all the probabilities of finding a point in phase space by integrating the distribution function over the phase space, normalization constant is obtained (so, the function can be normalized).

$$\int dx f(x,t) = 1 \tag{2.17}$$

Now, it is possible to define an averaging procedure using the phase space distribution function so that distribution is taken into consideration while taking an average. So that Eq. 2.16 takes the form of Eq. 2.18.

$$\mathrm{A} = <\mathrm{a(x)}> = \int dx f(x,t) a(x) \tag{2.18}$$

It is obvious that the distribution at any point is a function of the trajectory of each point in phase space and since these points evolve under the effect of a Hamiltonian, this distribution function should be a functional of the Hamiltonian since Hamiltonian is a function and function of a function is called functional as given in Eq. 2.19. Form of this functional depends on the type of the ensemble used in calculation.

$$\mathrm{A} = <\mathrm{a(x)}> = \frac{1}{\mathrm{Z}} \int dx a(x) \mathcal{F}(\mathcal{H}(x)) \tag{2.19}$$

$$\mathrm{Z} = \int dx \, \mathcal{F}(\mathcal{H}(x)) \tag{2.20}$$

$$A =< a(x) >= \frac{\int dx a(x) \mathcal{F}(\mathcal{H}(x))}{\int dx \mathcal{F}(\mathcal{H}(x))} \quad (2.21)$$

In Eq. 2.19, Z represents the partition function which is defined as the number of microscopic states in the phase space accessible within a given ensemble as given in Eq. 2.20. As its name implies Z is the function that partitions microscopic states to macroscopic states. Placing Eq. 2.20 into Eq. 2.19, the equation that connects microscopic and macroscopic identities is obtained which is given in Eq. 2.21.

Another definition of the partition function that is given in Eq. 2.22 can be derived with the help of probability theory, quantum mechanics and classical thermodynamics. According to the quantum mechanics perspective, molecular partition function indicates how particles in an assembly are partitioned among the various energy levels of an atom or molecule [92].

$$Z = \sum_i \exp(-\varepsilon_i/kT) = \sum_j g_j \exp(-\varepsilon_j/kT) \quad (2.22)$$

In Eq. 2.22, every value of $i$ represents a different energy state and $\varepsilon_i$ represents the energy at every $i^{th}$ state. Another version of this equation given at the rightmost is the one that employs $j$ energy levels and the number of degeneracies ($\varepsilon_j$) per energy level. Eq. 2.22 is based on quantum mechanics; i.e. the probability of presence of a particle in any energy level or state is taken into consideration.

The concept of partition function is very useful in comprehending the distribution of points in a given phase space or in other words, the distribution of particles in different energy levels and states. By dividing the possibility of finding a particle at an energy level k by the partition function, one can derive the Maxwell-Boltzmann distribution. The Maxwell-Boltzmann distribution provides a description of the distribution of particle speeds in gases, where the particles do not constantly interact with each other but move freely between short collisions. While the Maxwell-Boltzmann distribution is generally considered as the distribution for molecular speeds, it may also refer to the distribution for velocities, momenta, and

magnitude of the momenta of the molecules as well, each of which will have a different probability distribution function.

$$\frac{N_k}{Z} = \frac{g_k exp(-\varepsilon_k/kT)}{\sum_j g_j exp(-\varepsilon_j/kT)} \tag{2.23}$$

Here, the form of the functional in the numerator and denominator of the expression at the rightmost of Eq. 2.21 is the key point in defining the relationship between the microscopic and the macroscopic worlds and this functional takes a form according to the type of ensemble used. There are many different types of ensembles used in simulating different systems: the microcanonical ensemble, canonical ensemble, grand canonical ensemble, isobaric ensembles and many others.

### 2.1.2.2 Different Types of Ensembles

#### 2.1.2.2.1 The Microcanonical Ensemble

This ensemble pertains to a collection of systems in an isolated container of fixed volume V in which fixed number of particles N have a fixed total energy of E as shown in **Figure 2.1**. The microcanonical ensemble is composed of η isolated systems (N, V, E) for which the total number of particles, N, the volume, V, and the total energy E are the replicated thermodynamic properties.

This collection of systems follows Hamilton's equation of motion. As mentioned in **Section 2.1.1**, a system that obeys Hamilton's equation must conserve the total Hamiltonian. Therefore, the functional $\mathcal{F}(\mathcal{H}(\mathrm{x}))$ must restrict x to those microstates for which $\mathcal{H}(\mathrm{x}) = \mathrm{E}$ [90]. In other words, in the microcanonical ensemble, all of the points must lie on the $\mathcal{H}(\mathrm{x}) = \mathrm{E}$ constant energy hypersurface. The function that implements this constraint into the averaging procedure is the Delta-Dirac function $\delta(\mathcal{H}(\mathrm{x}) - E)$. For the microcanonical ensemble, Eq. 2.21 takes the form of Eq. 2.24.

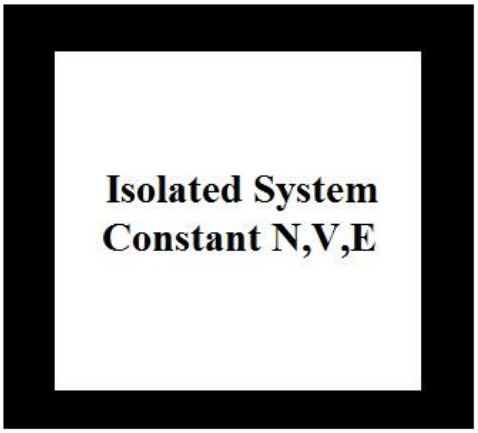


**Figure 2.1** Microcanonical ensemble represents a closed, isolated system.

$$A =< a(x) >= \frac{\int dx a(x)\mathcal{F}(\mathcal{H}(x)-E)}{\int dx \mathcal{F}(\mathcal{H}(x)-E)} = \frac{\int dx a(x)\delta(\mathcal{H}(x)-E)}{\int dx \delta(\mathcal{H}(x)-E)} \quad (2.24)$$

**2.1.2.2.2 The Canonical Ensemble**

Microcanonical ensemble is the most basic ensemble from which all the other ensembles are derived. Carrying out molecular dynamics simulations is possible with microcanonical ensemble but experiments in real life cannot be carried out under the condition of constant total energy. There should be some other ensembles that have different sets of thermodynamic control variables so that conditions of the common experimental setups are better demonstrated in the simulations. Canonical ensemble is one of the most important ensembles that have this property.

The canonical ensemble pertains to a collection of systems in an isolated container of fixed volume V in which fixed number of particles N have a fixed temperature T. As given in **Figure 2.2**, this ensemble replicates thermodynamic properties of a system (System 1) that is in thermal contact with a thermal reservoir (System 2). In the microcanonical ensemble, neither heat nor mass could be transferred between the system and the surroundings whereas in canonical ensemble heat transfer between two systems is possible but mass transfer is not allowed. In this

study, canonical ensemble has been utilized to investigate the properties of silicene nanoribbons.

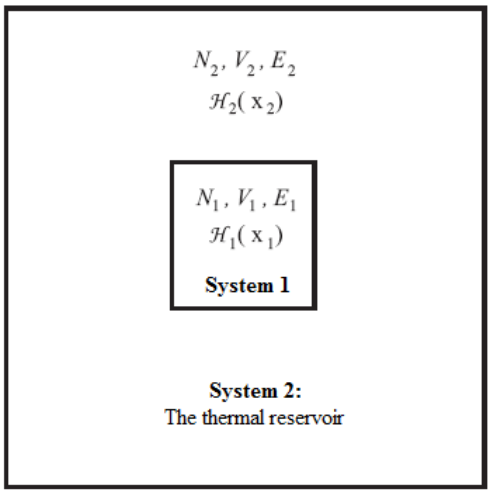


**Figure 2.2** Canonical ensemble replicates the properties of a system (System 1) in contact with a heat reservoir (System 2). The system 1 has fixed number of atoms N, fixed volume V and fixed temperature T.

#### 2.1.2.2.2.1 Thermostats in Isothermal Ensembles

Contrary to the microcanonical ensemble, the total energy in the canonical ensemble does not have a fixed value and the temperature of the system should be kept constant which is made possible with the aid of a thermostat which is a special type of algorithm for isothermal ensembles that has the capability of keeping the temperature constant during a molecular dynamics simulation. There are essentially three ways to control the temperature in a MD simulation:

1. Velocity scaling (e.g. simple velocity scaling and the Berendsen thermostat)
2. Addition of stochastic forces and/or velocities (e.g., the Langevin, Andersen and Dissipative Particle Dynamics thermostats)
3. Using “extended Lagrangian” formalisms (e.g., the Nosé-Hoover thermostat)

Each of these types of thermostats has their respective advantages and disadvantages, depending on the application [93].

#### 2.1.2.2.2.1.1 Simple Velocity Scaling and Berendsen Thermostat

Velocity scaling schemes do not strictly follow the canonical ensemble but in practice they deviate slightly from the canonical ensemble (the extent of deviation can be measured with the comparison between velocity distribution function with a Gaussian distribution function). In simple velocity scaling, particle velocities are chosen randomly and rescaled to maintain in a desired temperature given by the relation:

$$\frac{3}{2}Nk_BT = \frac{1}{2}\sum_i m_i v_i^2 \tag{2.25}$$

In velocity scaling, a dynamic scheme is obtained by calculating the velocities by scaling in such a way that the total kinetic energy is constant. In Eq. 2.26, the instantaneous temperature $T_i$ is the temperature that is measured immediately after a velocity update. Eq. 2.26 indicates that if the velocities are scaled by a factor $\lambda$, where

$$\lambda = \sqrt{\frac{T}{T_i}} \tag{2.26}$$

Then, the system is rescaled to the temperature$T$. In this study, simple velocity scaling is the thermostat utilized to keep the temperature constant during the molecular dynamics simulations.

Another popular velocity scaling thermostat is that of Berendsen [94]. Here, the scale factor $\lambda$ is given by Eq. 2.27.

$$\lambda = [1 + \frac{\Delta t}{\tau_T}\left(\frac{T}{T_0} - 1\right)]^2 \tag{2.27}$$

In Eq. 2.27, $\Delta t$ is the integration time step, $T_0$ is the setpoint temperature and $\tau_T$ is a constant called the ``rise time" of the thermostat. The rise time is a measure of the strength of the coupling of the system to a theoretical heat bath. As $\tau_T$ goes higher, the coupling becomes weaker; i.e. the larger $\tau_T$, the more amount of time is required to attain a temperature $T_0$ after an instantaneous change from some previous $T_0$. It should be taken into consideration that the Berendsen thermostat can jeopardize the validity of the simulation by introducing the flying ice cube effect which is a numerical integration artifact that leads to unphysical translations and rotations of the simulated system [95].

**2.1.2.2.2.1.2 Stochastic Thermostats**

Stochastic velocity scaling schemes have the advantage that these thermostats can easily be implemented within any molecular dynamics code, nevertheless, their lack of time reversibility and the fact that these thermostats are not deterministic which are properties that prove important in some advanced MD techniques. The simplest thermostat which follows the canonical ensemble correctly is the Andersen thermostat [96]. First, some prescribed number of particles is selected, and their momenta (actually, their velocities) are obtained with the help of a Gaussian distribution at that prescribed temperature as given in Eq. 2.28.

$$p = \left(\frac{\beta}{2\pi m}\right)^{\frac{3}{2}} \exp\left[\frac{-\beta p^2}{(2m)}\right] \tag{2.28}$$

Andersen thermostat is designed to mimic collisions with bath particles at a specified temperature$T$. The strength of the coupling to the heat bath is specified by a collision frequency, $\upsilon$. For each particle, a random variate is selected between 0 and 1. If this variate is less than $\upsilon\Delta t$, then that particle's momenta are reset.

There are other types of thermostats mentioned in the literature that can be classified under the title of “stochastic thermostats” like Langevin thermostat [97] and Dissipative Particle Dynamics thermostat [98,99].

#### 2.1.2.2.2.1.3 A Deterministic Thermostat: The Nosé-Hoover Thermostat

In Nosé-Hoover thermostat, the extended Lagrangian formalism that leads to a deterministic trajectory is used for keeping the temperature constant; in other words, randomization is not applied to the forces or velocities as in the stochastic thermostats [99]. In this case, the expression “extending the Lagrangian formalism” is used in terms of adding the thermostat as a constraint to the right side of the Euler-Lagrange equation (**Eq. 2.10**) which is mentioned in **Section 2.1.1**.

The fundamental logic behind the Nosé-Hoover thermostat is the utilization of a friction factor in order to control particle velocities. Actually, this friction factor is the scaled velocity, $\upsilon\varepsilon_1$, of an additional and dimensionless degree of freedom,$\varepsilon_1$ . $\varepsilon_1$has an associated ``mass", $Q_1$, which effectively determines the strength of the thermostat. With this additional degree of freedom, the equations of motion sample a canonical ensemble. This additional degree of freedom is the end point of a chain of similar degrees of freedom, each with their own mass. The main advantage of the Nosé-Hoover chain thermostat over stochastic thermostats is that the dynamics of all degrees of freedom are deterministic and time-reversible. The importance of these properties will be discussed in **Section 2.1.3.1.**

#### 2.1.2.2.2.2 Energy Fluctuations in Isothermal Ensembles

When temperature is kept constant, as in isothermal ensembles like canonical ensemble, fluctuations occur in total energy or internal energy. Due to the fact that there is no conservation of total Hamiltonian $\mathcal{H}$(x) in the canonical ensemble, fluctuation in energy needs to be quantified. In this study, the program code executing the molecular dynamics simulations of silicene also calculates the fluctuations in different components of energy and the total energy and finally, it

prints them out. Energy fluctuations can be quantified by using the standard statistical measure of variance as given in Eq. 2.35 [90].

$$\Delta E = \sqrt{< H^2(x) > - < H(x) >^2} \qquad (2.35)$$

$\Delta E$ is a measure of the width of the energy distribution graph, which is the root-mean-square deviation of H(x) from its average value. It should be taken into consideration that in the thermodynamic limit (in very large systems) where the number of particles goes to infinity, the difference in energy $\Delta E$ tends to become zero, so this means that the canonical ensemble approaches to the microcanonical ensemble in large systems and this is a proof of the fact that the choice of ensembles does not affect the results in such a case [90].

**2.1.2.2.3 The Grand Canonical Ensemble**

The canonical ensemble by which a system having the capability to transfer heat but not mass is replicated represents a combined system of a container tank placed in a heat sink. The grand canonical ensemble represents a more interactive system thermodynamically in which both heat and mass transfer is possible between two subsystems and where the control variables (i.e. fixed identities) are the chemical potentialμ, the temperature $T$ and the volume of the system $V$. In **Figure 2.3**, a system that has the mentioned properties of the grand canonical ensemble is shown. The system in the figure is composed of two systems in contact with a common thermal reservoir at fixed temperature T.

The grand canonical ensemble is very useful since it represents the conditions under which the real experiments are conducted much better when compared with microcanonical and canonical ensembles and it also gives direct access to the equation of state. One of the control variables of the grand canonical ensemble,the chemical potential $\mu$ is defined as the driving force for the mass transfer of species. In **Figure 2.3**, it can easily be seen that keeping $\mu$ leads to fluctuations in the particle number in System 1 in the grand canonical ensemble like the way keeping

temperature T constant leads to fluctuations in total energy in the canonical ensemble [90].

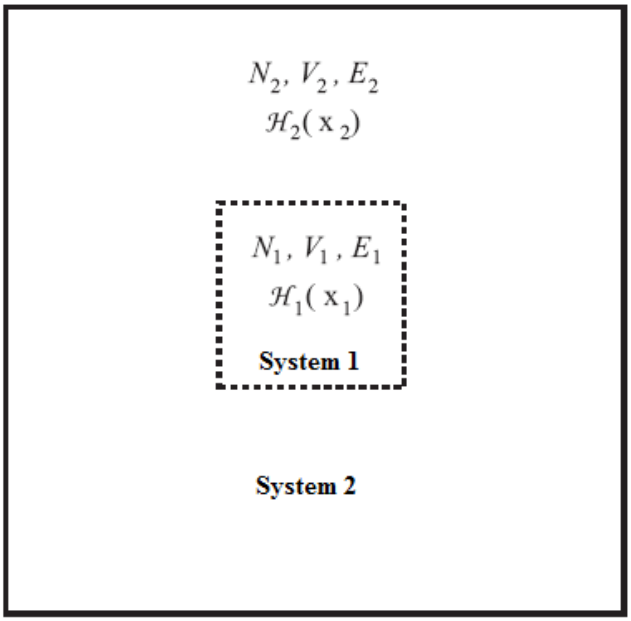


**Figure 2.3** Two systems in contact with a common thermal reservoir at temperature T. System 1 has $N_1$ particles in a volume $V_1$; system 2 has $N_2$ particles in a volume $V_2$. The dashed lines indicate that systems 1 and 2 can exchange particles.

#### 2.1.2.2.4 The Isobaric-Isothermal Ensemble

This ensemble replicates the properties of a piston cylinder system in which the number of particles (N), the pressure (P) and the temperature (T) are fixed. In a system where pressure and temperature is fixed, volume of the system is allowed to fluctuate. This type of ensemble becomes very useful in investigating structural phase transitions of solids under an external applied pressure or mapping the crystal structures of complex molecular systems in which anisotropic (i.e directionally dependent) effects take place [90]. Isobaric-isothermal ensemble is also very useful in simulating biological membranes, amorphous materials, and interfaces [100].

A comparison of different types of ensembles mentioned in this section is given in Table 2.1. Availability of a great number of various types of ensembles enables researchers to create simulations of experiments conducted under diverse conditions.

**Table 2.1** A comparison of different types of ensembles in terms of their control variables and the systems they represent.

| **Type of Ensemble** | **Constants in Different Ensembles** | | | | | | **System Represented by the Ensemble** |
|---|---|---|---|---|---|---|---|
| | **N** | **P** | **V** | **T** | **E** | **μ** | |
| Microcanonical | + | | + | | + | | Isolated container |
| Canonical | + | | + | + | | | Container in a thermal sink |
| Grand Canonical | | | + | + | | + | Permeable container in a thermal sink |
| Isothermal-isobaric | + | + | | + | | | Piston-cylinder system |

### 2.1.3 Solving the problem of motion: Molecular Dynamics Simulations

In **Section 2.1.1**, various formulations of the problem of motion that has been realized by Newton, Lagrange and Hamilton and the origins of molecular dynamics in classical mechanics have been discussed. The equation of motion deals with the motion of particular atoms or molecules at the microscopic level and in **Section 2.1.2**, the gap between the microscopic and macroscopic realms has been established with the aid of statistical mechanics and the concept of ensemble that enables a small number of atoms or molecules to represent very large systems at macroscopic level so that the information at atomic level obtained by any of the formalisms mentioned in **Section 2.1.1** can become useful. This section focuses on the essence of molecular dynamics simulations and use of this technique in bringing numerical solutions to the equations of motion. As mentioned in **Section 2.1.2**, different conditions in a real laboratory can be simulated with the choice of a proper ensemble.

#### 2.1.3.1 Integrating the equations of motion

The equation of motion is a differential equation which can be solved by integration that can only be realized numerically since it is impossible to do so by analytical means. Numerical methods for numerical integration of equation of motion can be classified into two groups: Verlet Type Algorithms (The Verlet Algorithm, Velocity Verlet Algorithm, Leap-Frog Algorithm) and Predictor Corrector Algorithms (Nordsieck-Gear Algorithm). G.Ciccotti and H.G. Hoover have classified these two types of equation of motion solving integrator methods as open (or predictor) and closed (or predictor-corrector) methods [107]. According to their definition, open methods present the types of algorithms where the positions, velocities, acceleration and other information about the system can be predicted only with the aid of the previous information whereas closed methods first predict a new value with a predictor formula and then use a function of the predicted value as a measure of correcting the predicted value [108].

Numerical integrators generate phase space vectors at discrete times which are multiples of a basic time parameter coined as the time step, $\Delta t$. The choice of time step is important for a given molecular dynamics simulation since very small time steps may extend the duration of the execution of the program whereas very long time steps may cause instability and inaccuracy in numerical integration. In this manner, a “right choice” is a function of many variables, one of which is surely the interactions between the particles in the system. A rule-of-thumb for appropriate choice of time steps for different systems is given in Table 2.2. As mentioned, the length of an appropriate time step choice depends on the type of motion present within the system.

**Table 2.2** Heuristics for time steps for different systems that show different types of motion (taken from A. Leach [31]).

| System | Types of motion present | Suggested Time Steps |
|---|---|---|
| Atoms | Translation | $10^{-14}$ |
| Rigid Molecules | Translation and rotation | $5*10^{-15}$ |
| Flexible Molecules, rigid bonds | Translation,rotation,torsion | $2*10^{-15}$ |
| Flexible Molecules, flexible bonds | Translation,rotation,torsion,vibration | $10^{-15}$ or $5 * 10^{-16}$ |

#### 2.1.3.1.1 Verlet type Algorithms

##### 2.1.3.1.1.1 Verlet Method

The easiest way to obtain a numerical integration scheme is to use a Taylor series expansion as given in Eq. 2.36 and neglect the rest of the series after the third term.

$$r_i(t+\Delta t) \approx r_i(t) + \Delta t\dot{r}_i(t) + \frac{1}{2}\Delta t^2\ddot{r}_i(t) + .. \approx r_i(t) + \Delta t V_i(t) + \frac{\Delta t^2}{2m_i}F_i(t) + .. \qquad (2.36)$$

When a similar expansion for $r_i(t-\Delta t)$ is written and added to $r_i(t+\Delta t)$, eventually the Verlet Algorithm given in Eq. 2.37 is attained. Like any other differential equation, solution of equation of motion also requires a set of initial coordinates $r_1(0), ..., r_N(0)$ and initial velocities $v_1(0), ..., v_N(0)$. By inputting these initial coordinates and velocities to a molecular dynamics code involving Verlet algorithm, a solution is obtained for the equation of motion [101].

$$r_i(t+\Delta t) = 2r_i(t) + r_i(t-\Delta t) + \frac{\Delta t^2}{m_i}F_i(t) \qquad (2.37)$$

#### 2.1.3.1.1.2 The Velocity Verlet Method

Even though phase space is composed of both positions and momenta (or velocities), the Verlet Algorithm generates only positions. Velocity Verlet method uses Eq. 2.36 for position evolution and Eq. 2.38 for velocity evolution [102].

$$V_i(t + \Delta t) = V_i(t) + \frac{\Delta t^2}{2m_i}[F_i(t) + F_i(t + \Delta t)] \tag{2.38}$$

#### 2.1.3.1.1.3 The Leap-Frog Algorithm

The Leap-Frog Algorithm is very similar to Verlet and Velocity-Verlet algorithms in the sense that this algorithm evolves velocities at half integer time steps and utilizes them to compute new positions. Primarily, the velocities are calculated at time $t + \Delta t/2$ (Eq. 2.39) and afterwards these velocities are used for the calculation of positions at time $t + \Delta t$ (Eq. 2.40). In this manner, velocities leap over the positions like a frog and this is why this algorithm is called as the leap-frog algorithm [103].

$$r_i\,(t + \Delta t) = r_i(t) + \Delta t\, V(t + \Delta t/2) \tag{2.39}$$

$$V_i(t) = \frac{1}{2}[V(t - \Delta t/2) + V(t + \Delta t/2)] \tag{2.40}$$

The finite difference methods mentioned here has the property of time reversibility. A deterministic simulation having the property of time reversibility satisfies the same dynamical equations as the original process, i.e. reversible dynamics; the equations are invariant or symmetric under a change in the sign of time as in the Eqns. 2.36, 2.37, 2.38, 2.39 and 2.40.

Nevertheless, there are other methods that are claimed to be more accurate than the algorithms in this section that do not satisfy any of these two properties, thereby, if those algorithms are applied to Hamiltonian systems in which the total energy is conserved, this leads to significant drifts in the total energy. Energy is a constant in microcanonical ensemble but in other ensembles where the total energy is not constant, energy may not be conserved. Energy drift is mainly a consequence of

energy fluctuations on a very small time scale and energy drift accrues due to the numerical integration artifacts arising from the utilization of the time step $\Delta t$. Energy drift occurs in MD simulations where symplectic Verlet type integrators are utilized but it is a very crucial potential problem that needs to be considered especially when the non-symplectic numerical schemes like the Nordsieck-Gear algorithm (that will be mentioned in the following section) are used in solving the equation of motion [104]**.**

**2.1.3.1.2 Predictor-Corrector Methods**

Predictor corrector methods constitute a widely used group of algorithms of numerical integration in numerical analysis. Predictor corrector methods are composed of two steps: in the first step, namely the prediction step, calculation of a rough approximation of the desired quantity is made and in the correction step, the initial approximation is refined. In this study, Nordsieck-Gear predictor corrector algorithm has been included in the molecular dynamics code as a means of solving the equation of motion.

Nordsieck-Gear algorithm [21,103] is an integration scheme based on Taylor expansion of the positions, velocities and further derivatives as shown in Eq. 2.41.

$$r(t+\Delta t) = r(t) + \Delta t v(t) + \frac{1}{2}\Delta t^2 a(t) + \frac{1}{6}\Delta t^3 q_3(t) + \ldots\ldots\ldots + \frac{1}{k!}\Delta t^k q_k(t) + \ldots.$$

$$v(t+\Delta t) = v(t) + \Delta t a(t) + \frac{1}{2}\Delta t^2 q_3(t) + \frac{1}{6}\Delta t^3 q_4(t) + \cdots \frac{1}{(k-1)!}\Delta t^{k-1} q_k(t) + \ldots.$$

$$a(t+\Delta t) = a(t) + \Delta t q_3(t) + \frac{1}{2}\Delta t^2 q_4(t) + \frac{1}{6}\Delta t^3 q_5(t) + \cdots \frac{1}{(k-2)!}\Delta t^{k-2} q_k(t) + \ldots.$$

$$q_i(t+\Delta t) = q_i(t) + \Delta t q_{i+1}(t) + \frac{1}{2}\Delta t^2 q_{i+2}(t) + \cdots + \frac{1}{(k-i)!}\Delta t^{k-i} q_k(t) + \ldots \quad (2.41)$$

i=3,4,5,….. where $q_k(t) = \frac{\partial^k}{\partial t^k} r(t)$

Now the position (i.e. $0^{th}$ derivative of r) $r^{(0)}$ and its scaled derivatives $r^{(k)}$ with

$$r^{(0)} = r,\ r^{(1)} = \Delta t v(t),\ r^{(2)} = \frac{1}{2}\Delta t^2 a(t),\ \ldots\ldots\ldots\ldots\ldots\ r^{(k)} = \frac{q}{k!}\Delta t^k(t) \quad (2.42)$$

Now, a simple Taylor series predictor gets the following form:

$$\begin{bmatrix} \tilde{r}_{n+1}^{(0)} \\ \tilde{r}_{n+1}^{(1)} \\ \tilde{r}_{n+1}^{(2)} \\ . \\ . \\ . \end{bmatrix} = \mathrm{P} \begin{bmatrix} r_n^{(0)} \\ r_n^{(1)} \\ r_n^{(2)} \\ . \\ . \\ . \end{bmatrix} \tag{2.43}$$

where P represents the Pascal triangle matrix with the binomial coefficient in its columns given in Eq. 2.44.

$$\mathbf{P} = \begin{bmatrix} 1 & 1 & 1 & 1 & 1 & 1 & \cdots \\ 0 & 1 & 2 & 3 & 4 & 5 & \cdots \\ 0 & 0 & 1 & 3 & 6 & 10 & \cdots \\ 0 & 0 & 0 & 1 & 4 & 10 & \cdots \\ 0 & 0 & 0 & 0 & 1 & 5 & \cdots \\ 0 & 0 & 0 & 0 & 0 & 1 & \cdots \\ \vdots & \vdots & \vdots & \vdots & \vdots & \vdots & \ddots \end{bmatrix} \tag{2.44}$$

In Eq. 2.43, it is shown that the matrix on the left side contains the predicted values of positions, velocities, accelerations and further derivatives. As a result of the missing introduction of the equations of motion, the predictor generates not the exact values for the position and its derivatives. However, with the aid of the predicted position $\tilde{r}_{n+1}^{(0)}$, calculation of the forces of n+1$^{th}$ time step and thus, the correct accelerations $a_{n+1}$ can be realized. Comparing correct acceleration with the predicted (scaled) acceleration $\tilde{r}_{n+1}^{(2)}$ (from Eq. 2.43) gives a measure for the error of the predictor step as shown in Eq 2.45. :

$$\vec{\varepsilon}_{n+1} = \frac{1}{2}\Delta t^2 a_{n+1} - \tilde{r}_{n+1}^{(2)} \tag{2.45}$$

Since the amount of error is calculated in Eq. 2.45, this error is utilized in order to improve the predicted values in the corrector step as shown in Eq. 2.46.

$$\begin{bmatrix} r_{n+1}^{(0)} \\ r_{n+1}^{(1)} \\ r_{n+1}^{(2)} \\ . \\ . \\ . \end{bmatrix} = \begin{bmatrix} \tilde{r}_{n+1}^{(0)} \\ \tilde{r}_{n+1}^{(1)} \\ \tilde{r}_{n+1}^{(2)} \\ . \\ . \\ . \end{bmatrix} + \begin{bmatrix} C_0 \\ C_1 \\ C_2 \\ . \\ . \\ . \end{bmatrix} \vec{\varepsilon}_{n+1} \tag{2.46}$$

In Eq. 2.46, the error is calculated with a corrector vector and it is added to the predicted values that are shown in Eq. 2.43. The values of the corrector vector are chosen according to the expansion *i* of the Taylor series that are given in Eq. 2.41. Generally, the Nordsieck-Gear algorithm works fine within the range *i*=3-8 since in that range, the corrector vectors can be found [108]. In **Table 2.3**, the $C_0$,$C_1$,$C_2$…. values for the Nordsieck-Gear corrector vector is given.

**Table 2.3** Nordsieck/Gear corrector vectors. Taken from [27,109]

| ***i*** | $\mathbf{c_0}$ | $\mathbf{c_1}$ | $\mathbf{c_2}$ | $\mathbf{c_3}$ | $\mathbf{c_4}$ | $\mathbf{c_5}$ | $\mathbf{c_6}$ | $\mathbf{c_7}$ |
|---|---|---|---|---|---|---|---|---|
| 3 | 0 | 1 | 1 | | | | | |
| 4 | 1/6 | 5/6 | 1 | 1/3 | | | | |
| 5 | 19/120 | 3/4 | 1 | 1/2 | 1/12 | | | |
| 6 | 3/20 | 251/360 | 1 | 11/18 | 1/6 | 1/60 | | |
| 7 | 863/6048 | 665/1080 | 1 | 25/36 | 33/144 | 1/24 | 1/360 | |
| 8 | 275/2016 | 19087/30240 | 1 | 137/180 | 5/16 | 17/240 | 1/120 | 1/2520 |

It should be taken into consideration that the Nordsieck-Gear algorithm is a self-starting algorithm that requires nothing but initial positions and velocities as an input. In addition to this, according to a comparison made by Berendsen and Van Gunsteren in [109], in terms of accuracy, energy drift and mean square fluctuations, it has been demonstrated that the Nordsieck/Gear algorithm is the numerical integration algorithm that has the highest accuracy with respect to deviations from the exact trajectory. The Nordsieck-Gear algorithm is central to the molecular dynamics code that has been utilized throughout the course of this study and constitutes the core of the software used as will be shown in **Section 2.3**.

### 2.1.3.2 Calculation of Forces

In Eq. 2.13, it has been shown that the Hamiltonian operator is made up of two parts: Kinetic energy part and the potential energy part. Kinetic energy is the energy that a particle possesses due to its motion whereas potential energy is a function of the arrangement of the particles of the system i.e. the way the particles within a system interact. While describing the Hamiltonian, a definition has been made for the kinetic part of the Hamiltonian operator; however a discussion of the potential energy function has been intentionally left to this separate section.

As mentioned before, the simulation method used throughout this study is the empirical molecular dynamics where the word "empirical" signifies "importing experimental information" to the code by using empirical potentials to represent the interaction of the particles within the system rather than starting from scratch and calculating all the possible interactions likewise of the way it is done in ab-initio molecular dynamics calculations.

A summary of the empirical potential energy functions (PEFs) are given in two review articles by S. Erkoc [110, 111]. These empirical PEFs have been formed for different type of atoms and molecules and the choice of potential is crucial in obtaining a realistic result in simulation. The importance of choosing a proper potential is prominent also in terms of the computational cost since force calculation is generally what takes most of the time (even more time than numerical integration) during a molecular dynamics simulation. As an example, given that a molecular dynamic simulation lasts for N steps, the number of numerical integration operation carried out is N whereas the number of operations required for pairwise potentials is N(N-1)/2 and for three-body effects it is N(N-1)(N-2)/6 [28,31]. This shows why the greatest computational effort in molecular dynamics simulations is devoted to force calculations, especially to Van der Waals type non-bonded interactions which may include pairwise effects and three or four body effects depending on the empirical potential energy function used.

Force calculation is possible only after the potential energy has been calculated. Calculation of the forces is made by deriving all the forces from the potential U as shown in Eq. 2.47.

$$\boldsymbol{F}_i = -\frac{\partial}{\partial \boldsymbol{r}_i} U(\boldsymbol{r}_1, \dots \dots \dots \boldsymbol{r}_N) \tag{2.47}$$

The molecular dynamics code used in this study makes the force calculation via the Pearson et al. potential [112] which is defined as the linear combination of a two body potential called as the Lennard-Jones potential [113] and a three body potential named as Axilrod-Teller potential [114]. Each of these potential have their own parameters that must be discreetly defined in order to execute a realistic simulation.

In the two-body Lennard-Jones potential [115] given in Eq. 2.48, there are two adjustable parameters which are namely the collision diameter $\sigma$ (the separation distance where the energy is zero) and the well depth $\epsilon$. In **Figure 2.4**, a graphical illustration showing a description of the parameters is given.

$$U_2(\boldsymbol{r}_\mathrm{i}, \boldsymbol{r}_\mathrm{j}) = U_\mathrm{ij} = 4\epsilon \left[ \left( \frac{\sigma}{\boldsymbol{r}_\mathrm{ij}} \right)^{12} - \left( \frac{\sigma}{\boldsymbol{r}_\mathrm{ij}} \right)^{6} \right] \tag{2.48}$$

where $\boldsymbol{r}_i$ is $\left| \boldsymbol{r}_i - \boldsymbol{r}_j \right|$.

Another possible description of the Lennard-Jones potential can be made in terms of the separation at which the energy passes through a minimum $r_m$ which is $\boldsymbol{r}_m = 2^{1/6}\sigma$ as given in Eq. 2.49.

$$U_2(\boldsymbol{r}_\mathrm{i}, \boldsymbol{r}_\mathrm{j}) = U_\mathrm{ij} = \epsilon \left[ \left( \frac{\boldsymbol{r}_\mathrm{o}}{\boldsymbol{r}_\mathrm{ij}} \right)^{12} - 2 \left( \frac{\boldsymbol{r}_\mathrm{o}}{\boldsymbol{r}_\mathrm{ij}} \right)^{6} \right] \tag{2.49}$$

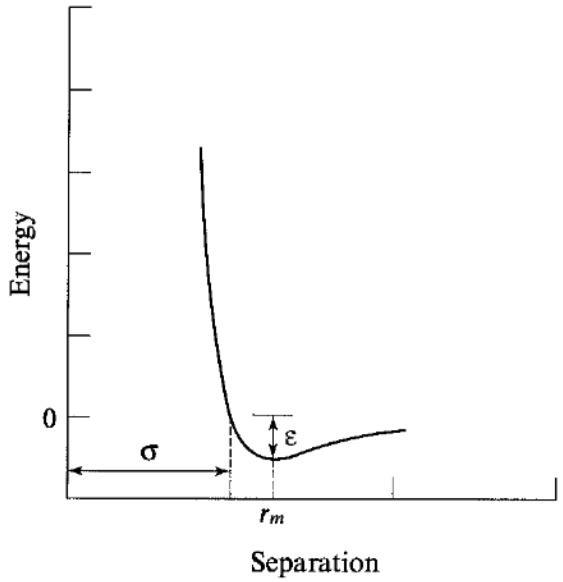


**Figure 2.4** The Lennard-Jones potential (taken from [31]).

The Lennard-Jones potential and other two body potentials only calculate pairs of interaction sites, nevertheless, the total interaction between two molecules can be affected by the presence of a 3rd molecule or more molecules. With the presence of a three-body empirical potential energy function, one can implement these effects into the molecular dynamics code [31]. The Axilrod-Teller potential is a three body potential that includes these effects. In order to better understand the nature of this interaction, a hypothetical triangle may be drawn between the three particles under investigation as shown in **Figure 2.5**. The Axilrod-Teller potential [114] is a function of the distances between these three particles, the angles of this hypothetical triangle (internal angles) and the empirical parameter Z as given in Eq. 2.50. The parameter Z is a common characteristic of the three particles under investigation and like the well depth $\epsilon$ and minimum energy separation $r_m$ that are included in Lennard-Jones potential, inputting this parameter into the molecular dynamics code is a must for carrying out the calculations.

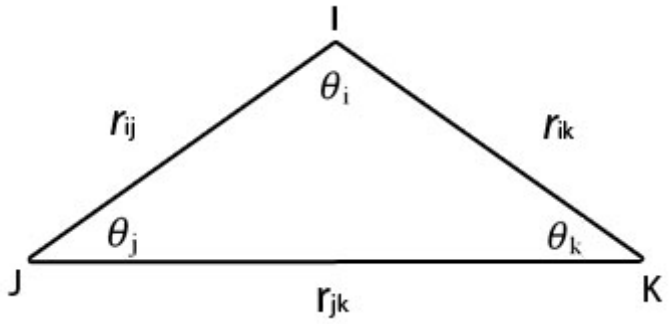


**Figure 2.5** Calculation of the three-body Axilrod-Teller contribution.

$$U_3(r_i, r_j, r_k) = W_{ijk} = Z\,\frac{(1+3\cos\theta_i\cos\theta_j\cos\theta_k)}{(r_{ij}r_{jk}r_{ki})^3} \qquad (2.50)$$

The Pearson et al. potential [112] which is the total interaction energy function Φ for N particles is a linear combination of the two body Lennard-Jones potential $U_2(r_i, r_j)$and Axilrod-Teller potential as $U_3(r_i, r_j, r_k)$given in Eq. 2.51.

$$\Phi = \sum_{i<j} U_2\,(r_i, r_j) + \sum_{i<j<k} U_3(r_i, r_j, r_k) \qquad (2.51)$$

The two parameters required for the calculations of two-body interactions are $\epsilon_o$=2.817 eV and $r_o$= 2.295 Å (the equilibrium interatomic distance for Si dimer) and the Z parameter required for the calculation of three-body interactions is Z = 3484 eV $Å^9$ [112].The present PEF is one of the reliable empirical potentials used for silicon in the literature [115]. These parameters satisfy absolute mechanical and thermodynamic stability of the diamond cubic structure [116], as well as surface [116] and cluster properties [117] of silicon. Although there are many other potential energy functions developed for silicon, it is not practical to test all the functions available in the literature in the context of this study. The comparison of the present PEF for silicon with other available PEFs for silicon is discussed in detail in the Ref [118].

### 2.1.3.3 Periodic Boundary Conditions

In some molecular dynamics simulations, surface interaction of the atoms with the container walls dominates all the interactions in such small systems and

obtaining clear information about the behavior of the bulk portion of the matter would not be likely. As an instance, in order to hold 500 atoms at a liquid density, a cube must have an edge length of about 8.5 atomic diameters; nevertheless, interactions between the wall and the fluid extend 4 to 10 atomic diameters from each wall [119].

Periodic boundary replicates the particles and their positions in a cell to other replicate cells. This replication may be realized along only one dimension or two or three dimensions. For instance, in the two-dimensional example given in **Figure 2.6**, each box have eight neighboring boxes; if the replication is done in three dimensions, each box would have 26 nearest neighbors. Computation of the coordinates of the particles that are in image boxes can be performed simply with the addition or subtraction of integral multiples of the box sides. Throughout the course of the simulation, whenever a particle leaves the box from one side, then it is replaced by an image particle that enters from the opposite side, as illustrated in **Figure 2.6**.

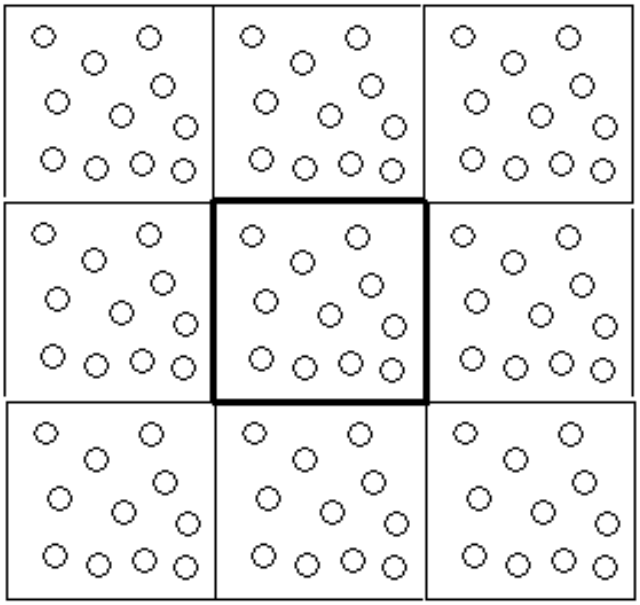

**Figure 2.6** Periodic boundary conditions in two dimensions.

Even though application of periodic boundary conditions (PBC) is crucial for many applications, there are some drawbacks of periodic boundary conditions that

should be kept in mind during use. The first drawback is that when the range of the fluctuations is greater than the length of the image cell which may cause problems since in certain situations such as the solutions that are at conditions near the gas-liquid critical point; the presence of PBC jeopardizes the accuracy of the simulation. Another drawback arises when the interactions in the system have greater range than the cell in the system under investigation. This is a very important problem to tackle in simulating systems where long range interactions are dominant. Evaluation of the extent of this drawback can be analyzed with imposing periodic boundaries of different size and shapes [31].

#### 2.1.3.4 Lowering the Computational Cost

As mentioned in the previous sections, force calculation is the most time consuming part of the molecular dynamics simulation and in some cases it may be extremely cumbersome if the interactions between all the atoms of a system is calculated regardless of the distance between them. The cut-off radius $r_c$ defines a hypothetical circle around each atom in which all the interactions are calculated regularly and out of which all the interactions are discerned.

Another popular way to deal with the non-bonded interactions is to apply minimum image convention where each atom 'sees' just one image of every other atom in the system (which is repeated many times in the presence of a periodic boundary) and all the calculations are made with the closest atom or image. Here, this puts a constriction over the cutoff radius since if the cutoff is too large, then a particle may see its own image or the same molecule twice or more. This limits the cutoff in such a way that it should not be bigger than one full length of the cell.

At first sight, cut-off radius seems to decrease the number of calculations that need to be performed by the computer; however it turns out that its effect would not be a dramatic as expected. This is because the computer has to calculate the distance between every pair of atoms in the system since a decision should be made over whether these atoms are close enough to calculate their interaction energy or not and

unfortunately, calculation of N(N-1) distances would take a comparable amount of time as calculating the total interaction energy without a cut-off radius [31].

A bookkeeping scheme known as the Verlet Neighbor List [101] has been devised to overcome this problem. For every atom $i$, a list of neighboring atoms that lie within a distance $r_L$ of $i$ is kept in such a way that the list identities those atoms that contribute to the force on atom $i$. This Verlet neighbor list is utilized over several consecutive time steps, and it is updated periodically. In the molecular dynamics code that has been utilized in this study, the user has the liberty to define the frequency of neighbor list updates which directly affects the computational cost of the simulation. Generally, the list distance $r_L$ should be slightly larger than $r_c$as a precaution. The following equation can be considered as a rule of thumb for Verlet Neighbor List distance: $r_L = r_C + 0.3$ [119].

## 2.2 The Strategy Followed Throughout the Study

In this study, mechanical and structural properties of two dimensional silicene nanoribbon sheets (SiNRs) have been investigated with the molecular dynamics simulation technique. This study is composed of two different consecutive parts. In the first part, SiNR sheets have been relaxed under 72 different conditions to understand their properties at equilibrium and in the second part, strain has been applied to these models in order to investigate the mechanical properties of SiNR sheets, namely the way these materials respond to strain application.

In the first part of this study, primarily, silicene nanoribbons (SiNRs) have been defined with initial positions of the silicon atoms in a honeycomb fashion with zig-zag edges. Width definition of SiNRs has been made in terms of the number of arrays (nA). Six different nA structures of SiNRs has been used where n=1-6. Also SiNR models with three different lengths in terms of the number of hexagons (mH) has been considered where m=10, 20, 40. These predefined initial working cells have been studied both at 1 K° and 300 K° temperatures and both with periodic boundary (denoted as PB) and without periodic boundary (denoted as NoPB). In the present study, a total of 72 separate SiNR models have been considered. During the

calculations, the initial nearest-neighbor distance for the silicon atoms is taken as a=2.35 Å which is the bulk Si dimer distance [120]. Throughout this study, for the working cell, such a notation (nA,mH) has been used where n=1-6, m=10, 20, 40. An example for the initial unrelaxed working cell model (6A, 10H) is shown in **Figure 2.7**.

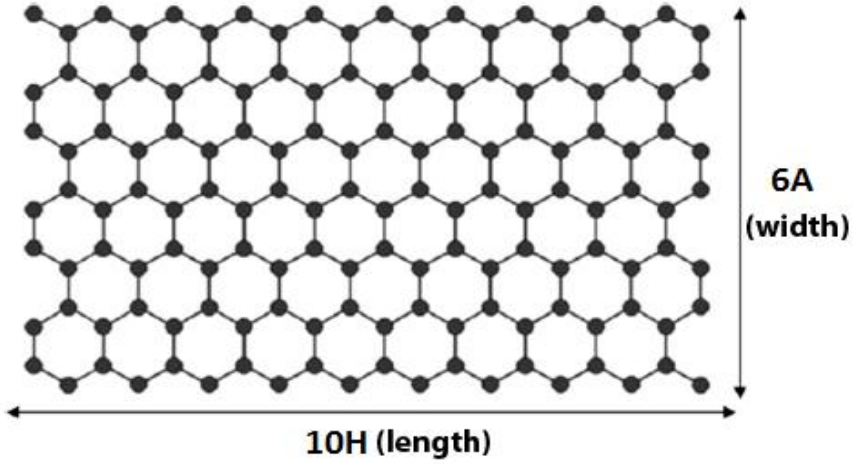


**Figure 2.7** (6A,10H) model of SiNR sheet defined as an initial model for the calculation. PB has been applied along the length.

In the second part of the study, an appropriate working cell has been generated for SiNR models by defining the initial positions of the silicon atoms in a planar honeycomb monolayer fashion as described in **Figure 2.8**. Although recent *ab-initio* calculations on 2D honeycomb structures of silicon show that buckled configuration of silicene is slightly more stable with respect to planar form [121], planar models has been chosen as the starting models because strain application would eventually transform the buckled configuration into planar form. In order to skip a few strain application steps, simulations have been initialized with planar models.

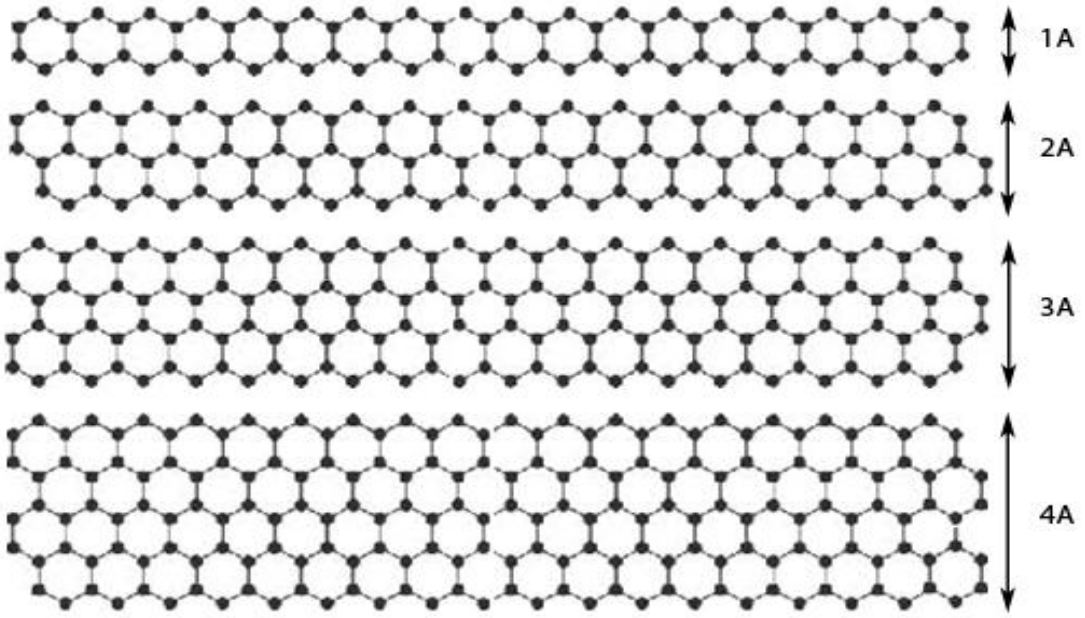


**Figure 2.8** The initial models of SiNR that have been used in the present study which are denoted as nA where n=1-4.

Zigzag nanoribbon models have been taken since relaxed SiNRs with periodic boundary along one-dimensional (1D) honeycomb structure would finally evolve into a triangular net, based on the experience from the first part of the study as discussed in **Section 3.1** and in [85]. For this reason, starting with different chiralities (armchair or zigzag) would not make any difference in the result.

In the second part of the study, width of the SiNRs is defined in terms of the number of arrays of hexagons (nA) where n=1–4. Length of all of the models is 81.4 A°, which corresponds to 20 hexagons of silicon atoms per one array. These pre-defined initial working cells have been studied at two different temperatures: 1 K° and 300 K° in order to understand the effect of the application of uniaxial stress with and without temperature effects better. 300 K° temperature has been chosen since the potential applications of SiNRs like electronics and signal detectors are expected to work at room temperature as mentioned in **Section 1.4**. In all models, a periodic boundary, which is defined according to the length of the model, has been utilized. Length of periodic boundary has been modified at each step according to the amount of applied strain. Strain has been applied to SiNR models in two different modes:

slow strain (5% strain per step) which is denoted as S and fast strain (10% strain per step) which is denoted as F. An example for the nomenclature utilized throughout the present study is; 1A-1K-S represents the model of 1A width, at 1 K° temperature, strained in slow strain mode. Strain has been applied to SiNR models in consequent steps in both S and F modes. In the first step, calculations have started with one of the initial models shown in **Figure 2.8** and the calculations mentioned are carried out by classical MD simulation technique. Firstly, initial models of varying widths (nA where n=1–4) are relaxed. After relaxation of the initial model, strain has been applied to the material along its length by multiplying the final positions of all atoms by a factor of 1.05 for the slow strain case (5%) and 1.1 for the fast strain case (10%). Then, the models are relaxed once more again until they come to equilibrium in terms of energy. This procedure has been continued until fragmentation is observed. Images of the structures obtained at each step have been taken, so that development of fragmentation in SiNR models could be analyzed thoroughly.

## 2.3 The Molecular Dynamics Code Used

The Molecular Dynamics Simulation code that has been used throughout this study is written in FORTRAN programming language by T. Halicioğlu in 1981 and this code's double precision version has been produced by Ş. Erkoç. Solution of the equations of motion of the particles in the code is realized by considering the Nordsieck–Gear algorithm [21, 106] and $7^{th}$ order predictor–corrector formalism [28]. For all energy and force calculations, the time step used in the molecular dynamics code was taken as $0.74 \times 10^{-15}$ s with a cut-off radius of 7.0 $\dot{A}$. The time step is calculated using Eq. 2.52 which is derived from the conservation of energy of a dimer (which is Si dimer) [122].

$$\Delta t = \sqrt{\frac{m r_0^2}{2\epsilon_0}} \tag{2.52}$$

In the simulations, the canonical ensemble (NVT) has been utilized. The temperature has been kept constant throughout the procedure of the simulation by

rescaling the velocities of the particles in the system. The MD runs have been realized on a single processor PC with Linux operating system. Systems simulated are relaxed in the range of 100000 to 25000000 time steps depending on the size of the model and the temperature considered.

In order to make a successful run with this program, the user needs two files: an executable md1x file (or FORTRAN code and a compiler that creates an executable file from this FORTRAN code) and md1x.inp file which includes the input. In **Figure 2.9**, a figure that shows the interface of the input file of the molecular dynamics code where the user can enter various information about the calculation that is about to start is given.

```
*** Si (silicene) nanoribbons 1L ***
 NRUN , IO , ISCALE
 1000000 , 1 , 2
 NSAVE1 , NSAVE2 , NPER
 100 , 5000000 , 100
 IUPDT1 , IUPDT2 , IUPPER
 0 , 5000000 , 100
 ICOOR1 , ICOOR2 , ICOPER
 5000 , 5000000 , 5000
 NTSFIN , IROL , IAVE
 5000000 , 100 , 500
TIME= 3600.00
 IC , MOVE , IPBC
 1 , 40 , 1
CUT=  7.00     TEMP= 300.0 DT= 0.740E-15
 2.817 , 2.295 , 3484.0 , 28.0855 , 1.0 , 4
  2.035 , 0.0   , 0.0 , 4.070 , 7.050 , 0.0 , 10 , 1 , 1 , 0
  0.0   , 1.175 , 0.0 , 4.070 , 7.050 , 0.0 , 10 , 1 , 1 , 0
  0.0   , 3.525 , 0.0 , 4.070 , 7.050 , 0.0 , 10 , 1 , 1 , 0
  2.035 , 4.70  , 0.0 , 4.070 , 7.050 , 0.0 , 10 , 1 , 1 , 0
  0 , 40.70 , 0.0 , 0.0 , 1.0
```

**Figure 2.9** The input file for the program: md1x.inp.

As shown in **Figure 2.9**, the interface of md1x.inp enables the user to define many things about the system under investigation: the number of simulation run steps (NRUN), start point, end point and frequency of saving the output file (NSAVE1,NSAVE2,NPER), start point, end point and the frequency of updating

Verlet Neighbor List (IUPDT1,IUPDT2 and IUPPER), number of moving atoms (MOVE), cutoff radius (CUT), temperature (TEMP), time step (DT), epsilon (shown as 2.817 for silicon in the figure, which is the well depth parameter of the Lennard-Jones potential), $r_o$ (shown as 2.295 for silicon in the figure, which is the minimum energy separation parameter of the Lennard-Jones potential), Z (shown as 3484.0 for silicon in the figure, which is a parameter of the Axilrod-Teller potential), AMASS (shown as 28.0855 for silicon in the figure, which is the atomic mass of silicon), initial coordinates of the atoms (that can be defined with the aid of a pattern), periodic boundary for three dimensions (shown as 40.70, 0.0, 0.0 which means periodic boundary is available only on the –x direction).

The program gets the information mentioned above from the input file md1x.inp in the INPUT subroutine and uses this information as an initial matrix at the rightmost side of the Eq. 2.43 and multiplies it with the Pascal triangle matrix in Eq. 2.44 to obtain the predictor matrix in the PRDICT subroutine. This matrix includes predicted positions, velocities, accelerations and further derivatives. Then, with this predicted values, force calculation is realized separately, first, Lennard-Jones interactions (in TWO subroutine) and then Axilrod-Teller interactions (in THREE3 subroutine) have been computed. At the end, force calculation is realized with the aid of the total interaction energy in the FORCE subroutine. After than that, kinetic energy of the particles is calculated in the KINET subroutine and here, the velocity scaling thermostat comes into play to sustain constant temperature which is the case in the canonical ensemble. VALUES subroutine finds the total energies and writes the rolling averages to md1x.ene (the frequency of taking rolling averages is inputted in IROL part of the md1x.inp as can be seen in **Figure 2.9**) and the statistical averages to md1x.sta (the frequency of taking statistical averages is inputted in IAVE part of the md1x.inp as can be seen in **Figure 2.9**). In the VALUES subroutine, energy fluctuations are also calculated with a modified version of the formula given in Eq. 2.35, given here in Eq. 2.53:

$$< (< \mathcal{H}(x) - < H(x) >)^2 > = < (\mathcal{H}^2(x) - 2\mathcal{H}(x) < H(x) > + < H(x) >^2) >$$

$$= < \mathcal{H}^2(x) > - 2 < \mathcal{H}(x) >< H(x) > + < H(x) >^2$$

$$= < \mathcal{H}^2(x) > - < H(x) >^2 \qquad (2.53)$$

In the KORECT subroutine, the accelerations and the predicted values are subtracted as in Eq. 2.45 to find the error and use this error to correct the predicted value as in Eq. 2.46. The coefficients in **Table 2.3** are coded into the program. With the corrected values, REPOS subroutine repositions coordinates, NEIGH subroutine applies a Verlet Neighbor list to define the neighbors within the cutoff radius of 7.00 A°. At the end of one step, the coordinates, forces and energies are printed in md1x.out which is the output file of the program. The program does not go on to termination until the number of run steps is equal to NRUN defined by the user in md1x.inp. As expected, output file of the program (md1x.out) is a very long file even for calculations with a very small number of steps so a very small portion of the output file is shown here for the sake of demonstration in **Figure 2.10**. A summary of the theory of the principles behind the molecular dynamics simulation is given in **Appendix A** whereas a chart of the molecular dynamics code used in this thesis is given in the **Appendix B**.

PERIODIC PRINTING OF COORDINATES, FORCES AND ENERGIES FOR STEP NO.- 25000

| ATOM NO. | COORDINATES (IN ANGSTROM) | | | FORCES (EV/ANG.) | | | ENERGIES (IN EV.) | | |
|---|---|---|---|---|---|---|---|---|---|
| | X | Y | Z | X | Y | Z | EPOTEN | EKINET | ETOTAL |
| 1 | 39.67595 | 2.86316 | 0.00000 | -0.3566E+00 | -0.4539E+00 | -0.2615E-07 | -4.97047 | 0.03211 | -4.93836 |
| 2 | 35.05211 | 2.60368 | 0.00000 | 0.1822E+01 | -0.4380E+00 | 0.2096E-07 | -4.78149 | 0.11900 | -4.66249 |
| 3 | 31.68954 | 5.22994 | 0.00000 | 0.4952E+00 | -0.2470E+00 | -0.9316E-09 | -2.71275 | 0.06046 | -2.65230 |
| 4 | 28.11905 | 3.57624 | 0.00000 | -0.2578E+01 | -0.1547E+00 | 0.1984E-08 | -4.29444 | 0.08428 | -4.21015 |
| 5 | 23.48197 | 4.05089 | 0.00000 | 0.3751E-02 | -0.1014E+01 | 0.1572E-07 | -4.20297 | 0.02288 | -4.18009 |
| 6 | 18.86174 | 4.22004 | 0.00000 | -0.2821E+01 | -0.8599E-01 | -0.1223E-07 | -4.14154 | 0.07403 | -4.06751 |
| 7 | 14.22680 | 3.84964 | 0.00000 | 0.1458E+01 | 0.1189E+00 | -0.6441E-08 | -4.31053 | 0.00023 | -4.31030 |
| 8 | 9.60714 | 3.62124 | 0.00000 | 0.1419E+01 | -0.1118E+00 | 0.6382E-08 | -4.45824 | 0.03655 | -4.42169 |
| 9 | 4.97657 | 3.91798 | 0.00000 | 0.1570E+01 | -0.4184E+00 | -0.2091E-07 | -4.58692 | 0.01755 | -4.56937 |
| 10 | 0.42042 | 4.69670 | 0.00000 | 0.2534E+00 | -0.9012E+00 | 0.2884E-08 | -3.47635 | 0.01250 | -3.46385 |
| 11 | 37.37786 | 2.62545 | 0.00000 | -0.1120E+01 | 0.1052E+01 | -0.9321E-08 | -4.67135 | 0.00192 | -4.66943 |
| 12 | 32.84821 | 3.17167 | 0.00000 | -0.1091E+01 | -0.2913E+00 | -0.2479E-08 | -4.87227 | 0.00172 | -4.87055 |
| 13 | 30.36273 | 3.32565 | 0.00000 | 0.2322E+01 | 0.2536E+00 | -0.3018E-08 | -5.09305 | 0.00198 | -5.09106 |
| 14 | 25.82835 | 3.75616 | 0.00000 | -0.1079E+01 | 0.1434E+00 | -0.2987E-08 | -4.37382 | 0.00420 | -4.36962 |
| 15 | 21.14716 | 4.18736 | 0.00000 | 0.2796E+01 | -0.3344E+00 | -0.8560E-08 | -4.20764 | 0.03845 | -4.16918 |
| 16 | 16.52017 | 3.97533 | 0.00000 | 0.1228E+01 | 0.1876E+00 | 0.1700E-07 | -4.39847 | 0.15534 | -4.24314 |
| 17 | 11.96143 | 3.75622 | 0.00000 | -0.3647E+01 | -0.4316E+00 | -0.1531E-08 | -4.28302 | 0.00300 | -4.28002 |
| 18 | 7.28761 | 3.70724 | 0.00000 | -0.2412E+00 | -0.7928E-01 | 0.5030E-08 | -4.51860 | 0.07906 | -4.43954 |
| 19 | 2.70279 | 4.27666 | 0.00000 | -0.2904E+00 | -0.5832E+00 | 0.1000E-07 | -4.39649 | 0.00762 | -4.38887 |
| 20 | 1.26644 | 2.24484 | 0.00000 | -0.4454E+00 | -0.4504E+00 | 0.1538E-07 | -5.10692 | 0.02958 | -5.07734 |
| 21 | 36.29364 | 0.41577 | 0.00000 | 0.3469E+00 | 0.1140E+01 | 0.4588E-08 | -4.79767 | 0.04340 | -4.75427 |
| 22 | 33.64370 | 0.63871 | 0.00000 | -0.5224E+00 | 0.8285E+00 | -0.3305E-07 | -4.86456 | 0.05991 | -4.80464 |
| 23 | 29.10406 | 1.24178 | 0.00000 | -0.1420E+01 | -0.4513E+00 | -0.1010E-07 | -4.44297 | 0.14301 | -4.29996 |
| 24 | 24.52523 | 1.67837 | 0.00000 | -0.1127E+01 | 0.3519E+00 | 0.1352E-07 | -4.47861 | 0.03064 | -4.44797 |
| 25 | 19.97155 | 2.00296 | 0.00000 | 0.8000E+00 | -0.4444E+00 | 0.1071E-07 | -4.52164 | 0.06701 | -4.45464 |
| 26 | 15.39512 | 1.63786 | 0.00000 | 0.1230E+01 | 0.2332E+00 | 0.6139E-08 | -4.27350 | 0.10473 | -4.16877 |
| 27 | 10.78203 | 1.38419 | 0.00000 | -0.7517E-02 | 0.8301E+00 | 0.1230E-07 | -4.22569 | 0.06002 | -4.16567 |
| 28 | 6.14048 | 1.55050 | 0.00000 | -0.1368E+01 | -0.3826E+00 | -0.5931E-08 | -5.07586 | 0.03785 | -5.03801 |
| 29 | 3.64354 | 1.93394 | 0.00000 | 0.1215E+01 | 0.3407E+00 | 0.7390E-08 | -5.27132 | 0.00079 | -5.27053 |
| 30 | 0.13611 | 0.01326 | 0.00000 | -0.2352E+01 | 0.1405E+01 | -0.1039E-07 | -4.27898 | 0.00562 | -4.27336 |
| 31 | 38.60501 | 0.56916 | 0.00000 | 0.2023E+01 | -0.6571E+00 | 0.1834E-07 | -4.72866 | 0.04482 | -4.68385 |
| 32 | 34.83184 | -1.34387 | 0.00000 | -0.5076E+00 | -0.1224E+01 | 0.3682E-08 | -2.83687 | 0.03955 | -2.79732 |
| 33 | 31.40143 | 1.10227 | 0.00000 | 0.7510E+00 | 0.2803E+00 | 0.3101E-07 | -4.62997 | 0.03318 | -4.59679 |
| 34 | 26.78631 | 1.35434 | 0.00000 | 0.1587E+01 | 0.3655E+00 | -0.5270E-08 | -4.23674 | 0.00697 | -4.22977 |
| 35 | 22.23588 | 1.76362 | 0.00000 | 0.7808E+00 | 0.8097E+00 | -0.1928E-07 | -4.28371 | 0.00927 | -4.27445 |
| 36 | 17.71432 | 1.84397 | 0.00000 | -0.1895E+01 | -0.1632E+00 | -0.4546E-08 | -4.37899 | 0.00220 | -4.37679 |
| 37 | 13.09939 | 1.55559 | 0.00000 | -0.9769E+00 | -0.2363E+00 | -0.1376E-07 | -4.34270 | 0.06930 | -4.27340 |
| 38 | 8.44529 | 1.41832 | 0.00000 | 0.7813E+00 | 0.2809E+00 | -0.5066E-08 | -4.31532 | 0.00761 | -4.30771 |
| 39 | 4.73597 | -0.32987 | 0.00000 | -0.4154E+00 | 0.1225E+01 | 0.1773E-07 | -3.55952 | 0.00512 | -3.55440 |
| 40 | 2.39505 | -0.08694 | 0.00000 | 0.1379E+01 | -0.2918E+00 | -0.1880E-07 | -4.42534 | 0.01575 | -4.40959 |

EPT1- -175.82595 EPT2- 0.00000 EPT3- 0.00000 EPTT- -175.82595

**Figure 2.10** A small part from the output file for the program: md1x.out.

# CHAPTER III

# RESULTS AND DISCUSSION

In this study, mechanical and structural properties of silicene nanoribbons (SiNRs) are analyzed using the molecular dynamics simulation technique. In the first part of this study, each of 18 different SiNR models (models made up of 6 different width and 3 different length sizes) are relaxed at 1 K° and 300 K° temperatures. These models are relaxed both under presence and absence of periodic boundaries. In the second part of the study, 5% (slow strain mode) and %10 (fast strain mode) of constant strain has been applied to 4 different SiNR models (models made up of 4 different width sizes) at 1 K° and 300 K° temperatures.

## 3.1 Relaxation of Silicene Nanoribbons

In order to study the structural properties of the silicene nanoribbons (SiNRs), molecular-dynamics simulation has been utilized to show how the silicon honeycomb structure alters while it attains the state of equilibrium as given in [123]. The effects of width and length changes are discussed in separate subsections; **Section 3.1.1** and **Section 3.1.2**. Some of the SiNR models are eventually wrapped up to show tubular structures which are discussed at the last subsection of this part; **Section 3.1.3**.

### 3.1.1 Effect of width change on the final structure

First, silicene nanoribbons (SiNRs) have been defined with initial positions of the silicon atoms in a honeycomb fashion with zig-zag edges as shown in **Figure 2.7**. The number of arrays (nA) are utilized in the width definition of SiNRs. In defining

the width, six different nA structures of SiNRs has been used where n=1-6. The number of hexagons (mH) are used as a measure in the length definition of the SiNR models under investigation where m= 10, 20, 40. These unrelaxed working cells have been studied both at 1 K° and 300 K° temperatures and both with periodic boundary (denoted as PB) and without periodic boundary (denoted as NoPB). The initial nearest-neighbor distance for the silicon atoms is taken as a=2.35 Å [120] during the course of the study. An example for the nomenclature used in this part is as follows: 6A-10H-300K-PB stands for the SiNR sheet made up of 6 arrays of atoms per 10 hexagons in each array (in the initial configuration) that has been simulated at 300 K° temperature in the presence of a periodic boundary.

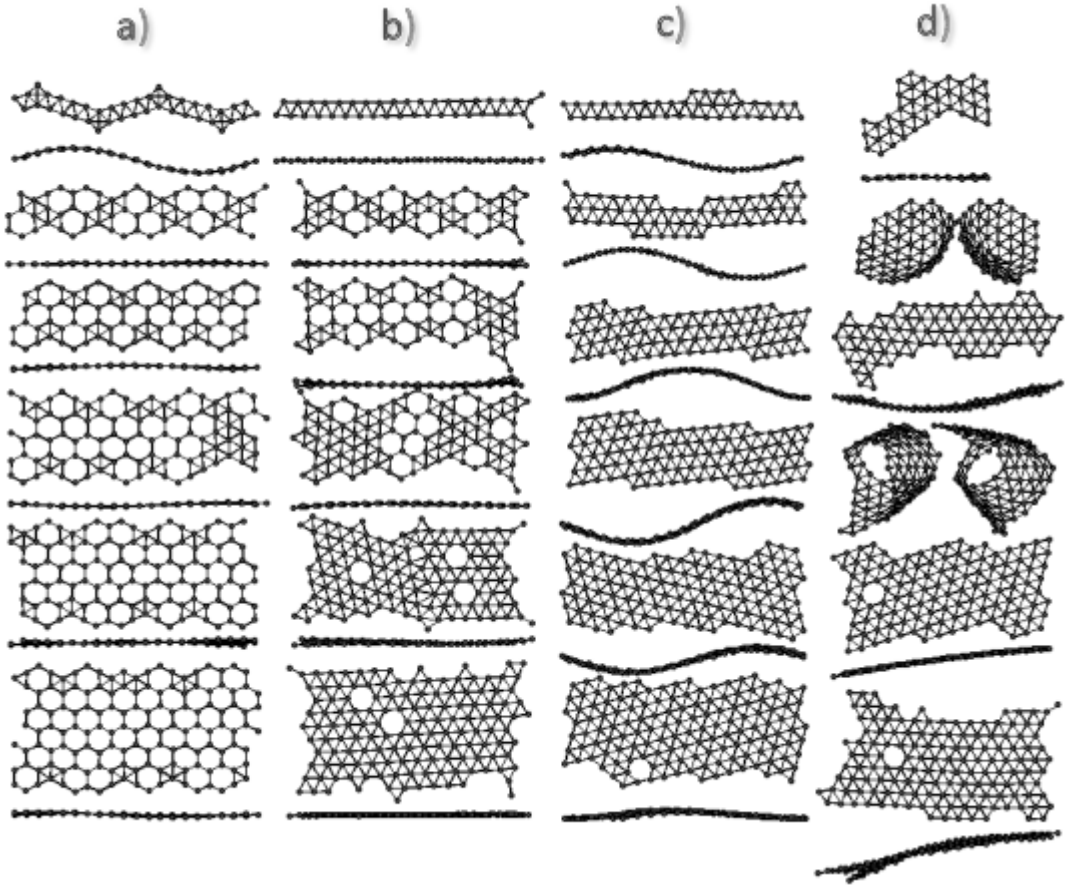


**Figure 3.1** Top and side views of different 10H structures of increasing nA numbers where n=1-6 are shown from the top row to bottom one. These structures are **a)** 1K, PB; **b)** 1K, NoPB; **c)** 300K, PB; and **d)** 300K, NoPB.

We have primarily focused on models of same length such as 10H which is the shortest model in terms of length so that we could comprehend the effect of increasing width. In addition to keeping the length constant, we should keep the temperature constant as well in each investigation and we should look at models with and without periodic boundary separately.

In 10H models at 1 K°, or in short 1K-10H, with periodic boundary conditions, increasing number of n in nA structures from 1 to 6 leads to the reduction in triangularization of the honeycomb hexagon structure. Triangular portions of the SiNR are localized to the edges. If we look at, for example, 1A-10H-1K-PB model in **Figure 3.1 a)**, we can see that the whole model is composed of triangles, however as we gradually increase the number of arrays and thereby the width of the model, we see that the percentage of the hexagons within the whole structure increases and as can be seen in n = 5 model or its n = 6 counterpart, these structures are mostly comprised of hexagons. For the n = 1 model, the bond distances at the edges of the molecule is in the range of 2.28–2.30 Å whereas for n > 1 models, this range represents the bond length of the connecting bonds at the edges between honeycombs to the angular grooves, so this might suggest that triangular structures tend to form mostly at edges since these triangles remain at edges as the width increases. The sides of the honeycombs having no connection with the triangular portions of the SiNR in all models except 1A (n = 2–6) show a typical bond length in the range of 2.25–2.27 Å which is within the bond length range of optimized silicene clusters given as 2.20-2.29 Å in [126]. In triangular portions of the SiNR, this value increases to a range of 2.36–2.48 Å. Even though the presence of triangles generally demonstrates a regular pattern, irregular bonds can also be encountered rarely with a bond distance up to 2.51 Å.

In 1 K-10H models without the restriction of periodic boundary or namely finite models as in **Figure 3.1 b)**, we see a reverse trend involving a reduction of the presence of the hexagons in terms of percentage. This is probably due to the fact that the presence of periodic boundaries prevents triangularization in the whole SiNR

excluding the edges. When the SiNR is left free of the boundaries as in this case, we see that triangularization starts at the sides of the SiNR with the increasing n, leaving a small amount of hexagons in the middle at higher n numbers such as 5A and 6A. In 300 K-10H models with periodic boundary as shown in **Figure 3.1 c)**, we can no longer encounter hexagons excluding n = 6 case where one hexagon was left, probably due to its requirement for much longer time steps of calculation than we have applied. At the edges of the SiNRs, longer bond lengths in the range of 2.30–2.39 Å is seen, but at the inner parts of the sheet, towards the center, bond lengths become much longer varying in the range of 2.36–2.50 Å. From the general trend of models, we can also infer that a tendency towards shrinkage along the length which may lead to irregularities in width along the length is present. This could not have been possible in this case regarding the presence of the periodic boundary. Due to this fact, rather than shrinkage along the length, twisting of the sheet occurs as can be noticed at the side view images of the SiNRs provided below its top views.

Similar behavior in terms of triangularization is encountered in finite models at 300 K as well which is the effect of temperature. From the present findings, one can clearly infer that SiNRs no longer show hexagonal honeycomb structure at room temperature. In 300 K-10H models without periodic boundary, we could not identify a general trend in accordance with increasing width as can be seen from **Figure 3.1 d)**. In n = 2 model, we have come up with such a structure that shows likelihood to fold at its sides in order to form a tubular structure but it could not due to its short length and width at the same time. In 4A-300 K-NoPB models, we encounter the only folded (and exceptional in this manner) m = 10 model among all 10H models which represent the tendency of the SiNR to form a tubular form even in such a short model in terms of length. It is very surprising that only n = 4 model forms a tubular structure while the others (thinner or thicker ones) did not. For models shorter than 20H, the requirement for silicon nanotube formation may be related to a specific aspect ratio which can be considered as a golden ratio when provided, results in transformation into tubular forms. Ranges of bond distances are generally similar to the ones encountered in PB models. Only for the tube forming 4A-10H-300 K-NoPB

model, at the connection points of the folded two sides of the sheet, the bond distances arise up to 2.60 Å. We will mention more about the folding mechanism and the resulting silicon nanotube structures at 300 K-NoPB models in **Section 3.1.3**. Under no-periodic boundary conditions, apart from the tendency of forming tubular structures, we have also encountered irregularity in terms of width. In the structures with PB, a 5A model is made up of five arrays as expected, but in the structures with NoPB, this is not so due to the shrinkage of bond lengths as can be recognized from **Figure 3.1 d)**.

### 3.1.2 Effect of length change on the final structure

The present findings show that, as well as the width change, different lengths may lead to dramatic changes in the final structures that have come to equilibrium. Here, we have taken 3A structures as an example. We have followed a similar strategy to that of the width change analysis made in **Section 3.1.1** by keeping the width constant at 3A and altering the length so that we could analyze the effect of length.

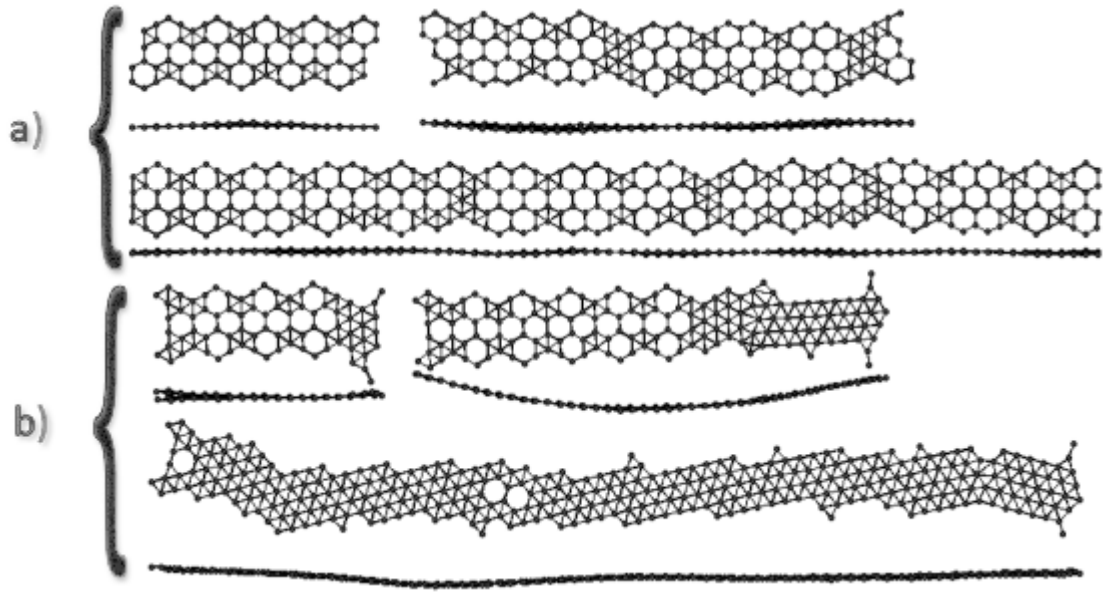


**Figure 3.2** Top and side views of different 3A structures of increasing mH numbers are shown where m=10, 20, and 40 at 1 K ° temperature: **a)** with periodic boundary; **b)** without periodic boundary. In each figure, 10H is at the top-left, 20H is at the top right and 40H is at the bottom.

In 1 K-PB structures, increasing number of m in mH where (m = 10, 20 and 40) results in structures that seem to follow a pattern as shown in **Figure 3.2 a)**. Instead of the effect of width change, we do not encounter with movement of triangularization starting from the edges of the SiNR, rather than that we see regular concentrations of triangularization occurring at different repeating points. No twisting action due to border restriction is seen neither, since side views demonstrate that SiNRs are nearly 1 atom thick, which is similar to the initial honeycomb SiNR structure in this manner. Bond distance lengths vary in a very narrow range between 2.25 Å and 2.27 Å at the edges whereas at the triangular portions of the SiNR distances increase up to 2.52 Å and this general trend does not change much at all as the length increases.

In the finite structures of 3A at 1 K in **Figure 3.2 b)**, regarding the fact that there are no more boundaries, we see that the formation of triangularization starts at

one edge and moves to the other side along the length. Especially in the 40H structure, there are only three hexagons left; two in the middle and one at the left side. Even though distance range at the edges and the regularly triangularized sections do not change much for the no boundary case, at the portions of the SiNR, where the movement of the triangularization has terminated, we can encounter with longer bond lengths in the range of 2.52–3.46 Å as seen in m = 10 and m = 20 cases. It looks as if somehow the movement of triangularization has been interrupted at that point due to the energetic reasons. In 40H case, the movement of triangularization has not terminated anywhere and this is the explanation of why bond distances of longer lengths are not encountered. Here, bond lengths are mostly in the range of 2.29–2.35 Å at the edges and 2.32–2.53 Å at the inner sections.

When we consider 300 K-PB and 300 K-NoPB structures in **Figure 3.3 a)** and **Figure 3.3 b)** altogether, we encounter with approximately complete triangularization of structure, which is again the effect of temperature as mentioned in **Section 3.1.1**. Here in the models with periodic boundaries, the SiNRs no longer show planar geometries, probably due to the energetic reasons since the SiNRs have the tendency to attain a more compact shape in order to get to a more ordered state in terms of energetics, but they could not, again due to the presence of boundaries. The images of 300 K-NoPB structures strongly support this fact as all of the 10H, 20H and 40H structures, in which there is an absence of boundaries, are more compact when compared to their counterparts with periodic boundaries. As mentioned before in the previous section, all of the SiNR models at 300 K that are equal to or longer than 20H length has shown tubular or curved structure formation which leads to the conclusion that change of length leads to the folding of the SiNR to a tubular form. For these structures, bond lengths vary in a range of 2.30–2.57 Å, again with shorter bonds at the edges and longer bonds at the inner portions.

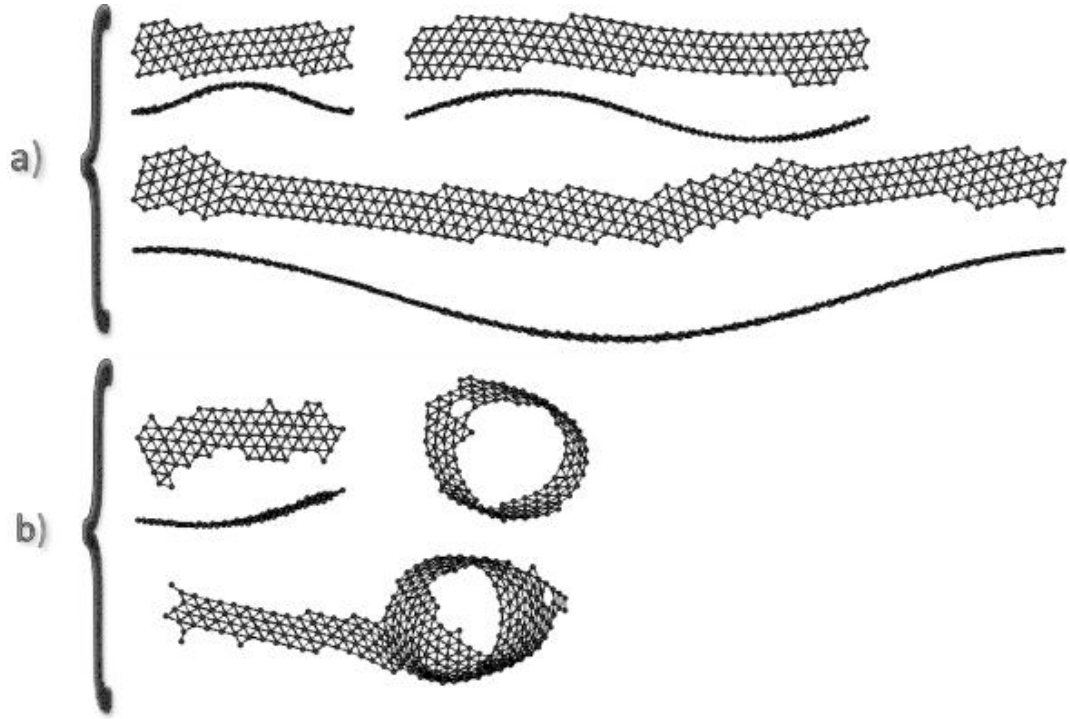


**Figure 3.3** Top and side views of different 3A structures of increasing mR numbers are shown where m=10, 20, 40 at 300 K° temperature: **a)** with periodic boundary; **b)** without periodic boundary. In each figure, 10H is at the top-left, 20H is at the top right and 40H is at the bottom.

### 3.1.3 Folding of silicene nanoribbons

In order to understand the nature of folding that we have encountered in all structures at 300 K that are of 20H and 40H in the absence of periodic boundaries, in addition to the exceptional 4A-10H-300 K-NoPB, we have analyzed the formation mechanism of these structures by utilizing some images taken at different stages of the calculation. We have shown, in **Figure 3.4**, the total potential energy versus number of MD steps graph as a guideline since the critical points of energy reduction with the elapsing time may give us clues about how the folding occurs into the final structure.

For the sake of demonstration, we have taken 6A-40H-300K-NoPB structure, the structure with the most number of atoms (560 atoms) as an example. As shown in**Figure 3.4 a)**, at earlier time steps around 200,000$^{th}$ step, the edges of the structure that has initially been straight has now been twisted after the first energy reduction at steps very close to the beginning. After the second energy reduction around 300,000$^{th}$ step, another image taken at 500,000$^{th}$ step reveals the fact that this reduction leads to the connection of these twisted edges resulting in a tubular silicon structure (See **Figure 3.4 b)**. This is a silicon nanotube which does not have a complete circular cross section, rather than that its cross section resembles an ellipse. These two reduction sections of the graph were very sharp leading to sharp changes in the resulting structure. After 1,200,000$^{th}$ step, we see a third but gradual reduction continuing till the 2,000,000$^{th}$ step where equilibrium has mostly been reached. In order to figure out what this means, we have obtained an image of 1,500,000$^{th}$ step as shown in **Figure 3.4 c)**, which shows that this reduction leads to a more regular tube shape in the structure. In order to enable better comparison we have included the image of the final structure at 5,000,000$^{th}$ step as shown in **Figure 3.4 d)**, which has come to equilibrium. As can be noted, the structures at 1,500,000$^{th}$ and 5,000,000$^{th}$ MD steps are very similar; the only difference is that the image taken at 5,000,000$^{th}$ step shows that the structure has a more tube-like form.

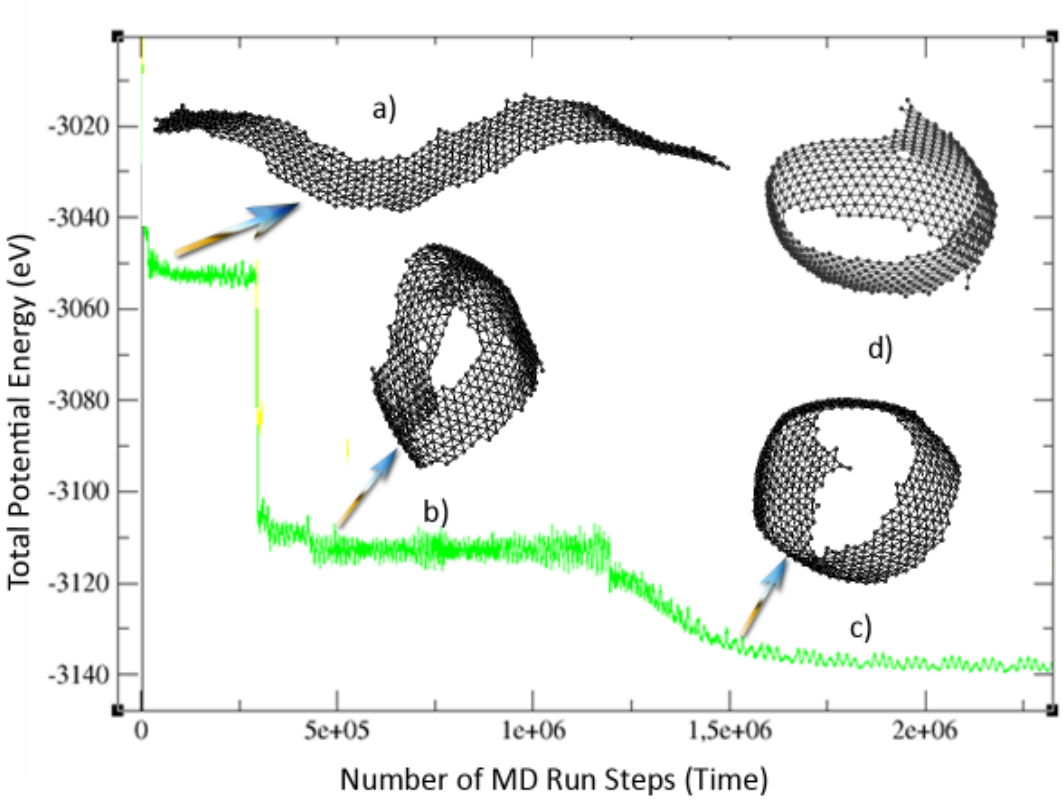


**Figure 3.4** The total potential energy versus number of MD steps for the model 6L-300K-40R-NoPB. Images showing the transformation of a finite length 6L-300K-40R-NoPB SiNR into a silicon nanotube at different MD run steps; **a)** at 200000; **b)** at 500000; **c)** at 1500000; **d)** at 5000000 (final step).

## 3.2 Strain Application to Silicene Nanoribbons

To understand mechanical properties of silicene nanoribbons, which may be important for device applications, we have investigated the structural behavior of silicene nanoribbons under uniaxial tensile strain. In practice, such materials may be used as a part of an electronic nanodevice. Such devices may be affected by various mechanical distortions during its operation, such as stretching, torsion, compression etc.. Among these mechanical effects, stretching (strain) is the most common external effect. For this reason, we have investigated uniaxial strain properties of silicene nanoribbons.

### 3.2.1 Fragmentation Mechanism

In the second part of the study given in [124], a tensile test has been realized on SiNR models of different widths at different temperatures by applying uniaxial strain along its length in both slow (S) and fast (F) strain modes where 5% and 10% strain have been applied to the material per one step respectively. We have continued applying strain until fragmentation of SiNR models took place so that fragmentation mechanism of SiNR and response of this material to the application of uniaxial load could be understood thoroughly. In order to comprehend fragmentation mechanism independent of any size changes, it would be a good idea to compare four different models of same size strained under different conditions. The present study commences with four different initial models of 81.4 Å length (width is denoted as nA where n=1–4) which is comprised of one or more hexagon arrays (four models of increasing width) as described in **Figure 3.5**.

Firstly, low temperature (1 K°) behavior of SiNR models has been investigated. The 1A-1K-F model, which is shown in **Figure 3.5**, is fragmented after seven steps of application of uniaxial strain whereas 1A-1K-S model (in **Figure 3.6**) is fragmented after 19 steps, which lasted longer.

In both models of 1A width, which are composed of two arrays of atoms, it is seen that SiNR models keep on elongating by transforming into one single array of atoms from two arrays of atoms. Here the material shows necking behavior rather than an immediate direct fragmentation. This shows that SiNRs can be very ductile under load application.

The difference between two models (**Figure 3.5** and **Figure 3.6**) shows the effect of strain modes (S or F), which is mostly seen at the number of points where necking starts. In 1A-1K-F model (**Figure 3.5**), it can be seen that there are many necking initiation points whereas in 1A-1K-S model (**Figure 3.6**), there are only two points of necking initiation. Looking carefully at how these atomic points develop

into a fragment in the following steps, it is obvious that in both models, necking starts from these points and spreads toward both sides without easily leading to fragmentation. In 1A-1K-F model, it can be realized that the material has fragmented at step #8 from a point where a necking region, which has started at step #3 as a single atomic point, has developed. In this model, there exist other points where necking has started at earlier steps and spread around along the entire SiNR in a greater extent but fragmentation has occurred at a single array of atoms closer to the side of the SiNR where uniaxial strain has been applied. Besides, in 1A-1K-S model in **Figure 3.6**, a smoother fragmentation mechanism has been encountered with respect to the 1A-1K-F model. In 1A-1K-S model, necking into one single array of atoms has completely occurred along the length of the SiNR before fragmentation as can be seen at step #18, whereas in 1A-1K-F model, there are still regions of two atomic arrays at the step of fragmentation. In 1A-1K-S model, the number of necking initiation points is lower and their occurrences develop slowly and gradually as the straining continues to further steps. Therefore, this leads to a smoother mechanism of fragmentation in 1A-1K-S model in comparison to the 1A-1K-F model. In both models, fragmentation develops with a mechanism of diffusion (which is a sort of dislocation) of second array of atoms toward the first array (toward the necking initiation point developed at the first array) that is located below. Atoms belonging to the second array dislocate toward that region more, as more uniaxial strain is applied.

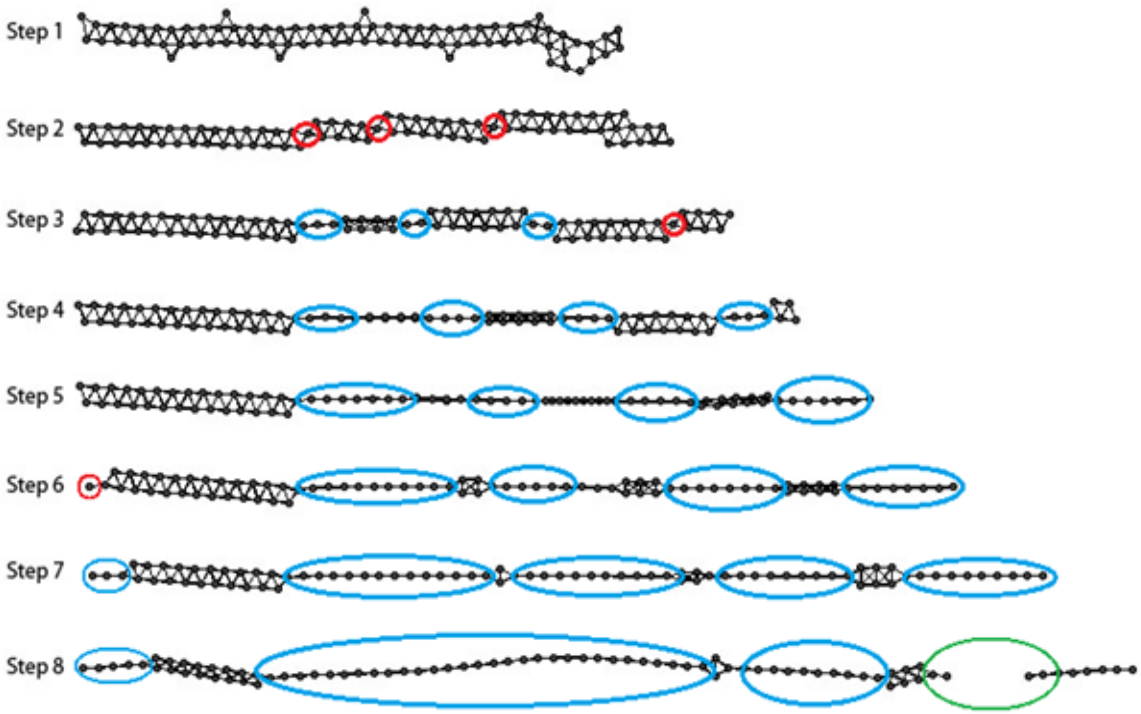


**Figure 3.5** Behavior of 1A-1K-F model SiNR under uniaxial strain. Fragmentation has occurred at the 8$^{th}$ step of %10 strain application. Red color indicates necking initiation points, blue color indicates regions of necking development and green color indicates fragmented regions.

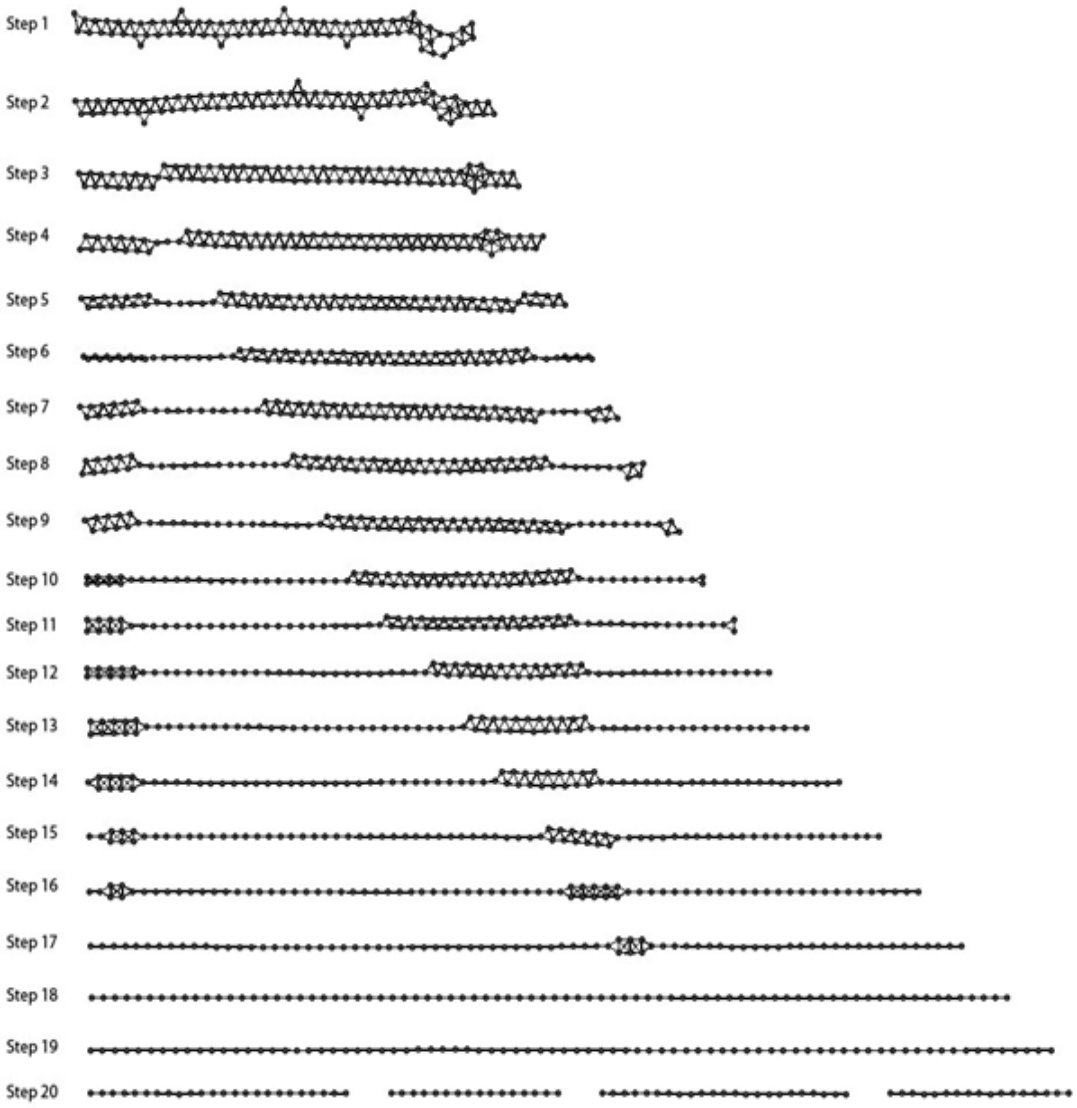


**Figure 3.6** Behavior of 1A-1K-S model SiNR under uniaxial strain. Fragmentation has occurred at the 20$^{th}$ step of %5 strain application.

Along with the studies realized at 1K temperature, models at 300K temperature have also been studied. As it can be seen from **Figure 3.7**, it took 10 steps to fragment the 1A-300K-F model and it took 19 steps to fragment the 1A-300K-S model, which is shown in Fig. 5. When both models are analyzed together, it can be seen that necking starts from one single point nearby the central region of the SiNR model. In 1A-300K-F model, additional necking initiation points arise from both edges whereas in 1A-300K-S model, a very smooth necking behavior is

encountered. In 1A-300K-S model, necking starts from a necking initiation point as in the other model compared and spreads toward both edges, so the 2D SiNR has completely transformed into a 1D atomic chain at step #18, which is the last step before fragmentation. In both models, fragmented pieces of SiNR form curvy structures as the ones that have been discussed thoroughly in **Section 3.1.3** where no periodic boundary is applied at 300 K° temperature. In that section and in [122], we have stressed that SiNR models meeting certain geometry conditions have shown tendency to develop into three dimensional curvy structures like silicon nanotubes.

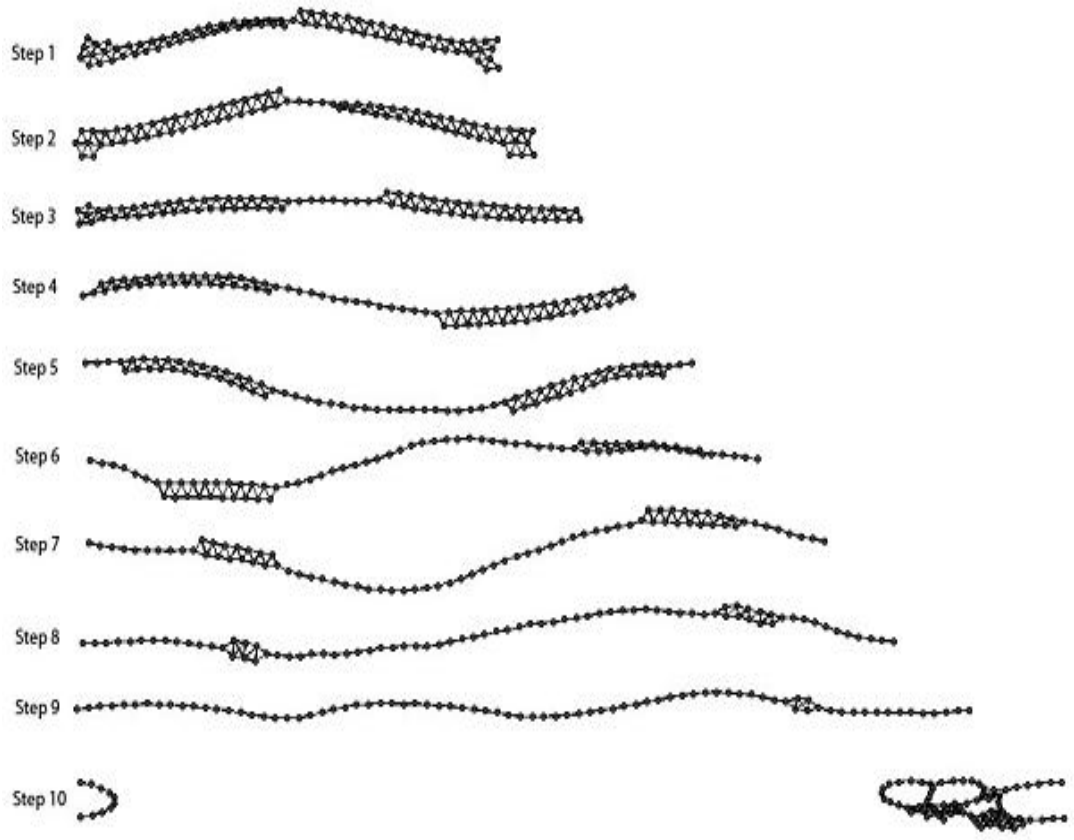


**Figure 3.7** Behavior of 1A-300K-F model SiNR under uniaxial strain. Fragmentation has occurred at the 10th step of %10 strain application.

We have studied these SiNR models at 300K temperature in order to understand how this material behaves under room temperature. In addition to this, comparison of the results of such a study with 1K studies would give information

about the effect of temperature to the results of the tensile test as well. In the models at 1 K° (**Figure 3.5** and **Figure 3.6**), it is seen that there are more necking initiation points than that of the models at 300K (**Figure 3.7** and **Figure 3.8**). This leads to the fact that in 300K models, it is a little bit harder to fragment the material. This could be due to the result of increased viscoelasticity (i.e., capability to resist fragmentation under strain) that SiNR models attain as a result of additional temperature increase. The smaller number of necking initiation points lead to a smoother fragmentation mechanism as it develops at the further steps and as mentioned before, especially in 1A-300K-S model, necking starts from the middle and spreads to both ends of the material gradually. As in all other materials, temperature increases ductility of SiNRs as well and fragmentation at 300 K° in S mode is smoother than its counterpart in 1K. In the first part of the study, it has been mentioned that SiNR sheets have a tendency to wrap at 300 K° in contrast to 1 K° models probably due to the presence of periodic boundaries. Here the same trend is seen during the course of the tensile test as in the other models.

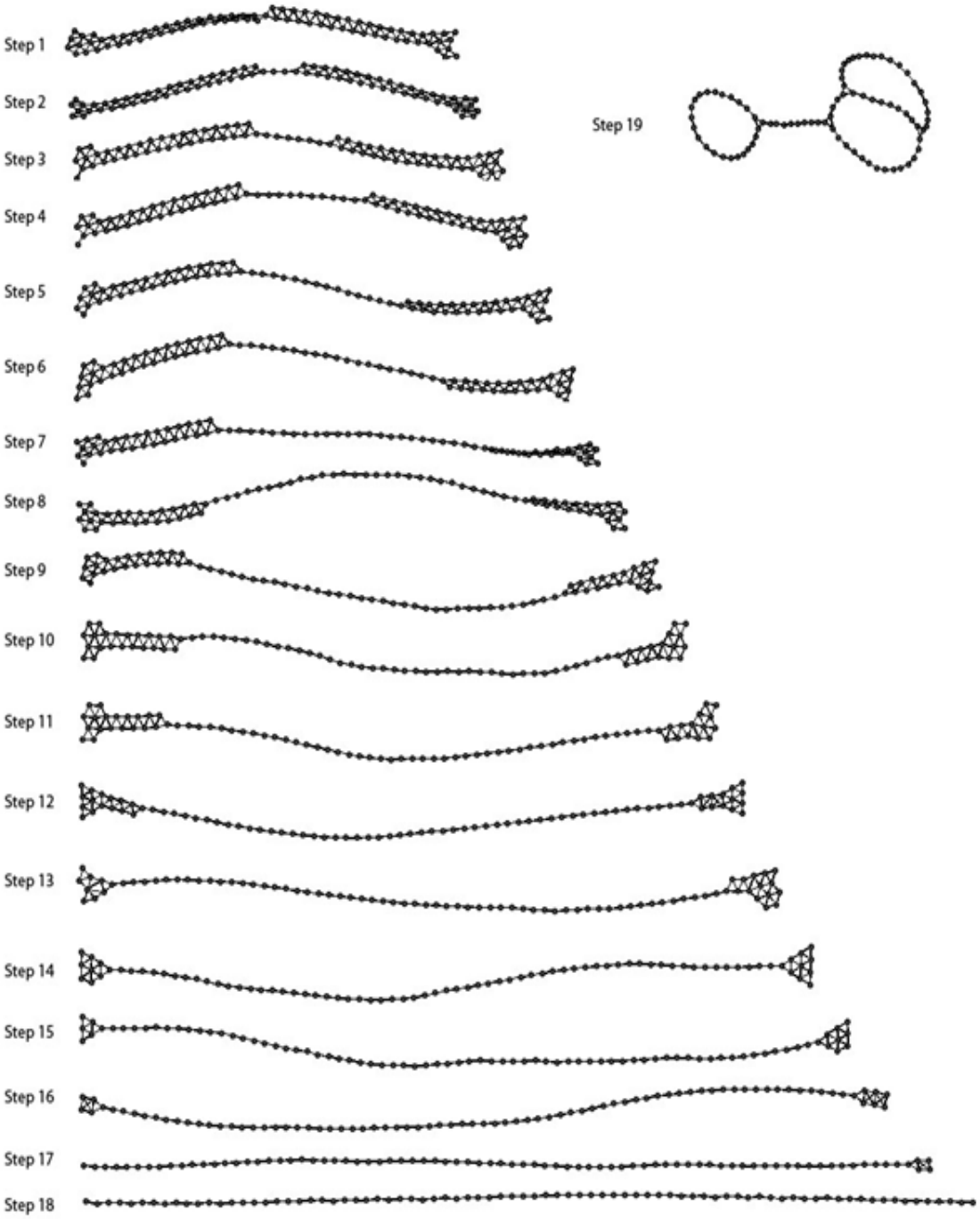


**Figure 3.8** Behavior of 1A-300K-S model SiNR under uniaxial strain. Fragmentation has occurred at the 19th step of %5 strain application.

### 3.2.2 Effect of increasing width

Along with changing temperature and applying tensile test in two different strain modes, models of larger widths than 1A-1K-F (**Figure 3.5**) are also studied, such as 2A-1K-F (**Figure 3.9**), 3A-1K-F (**Figure 3.10**), and 4A-1K-F models (**Figure 3.11**) to investigate whether the general trends that we have encountered in 1A models apply to thicker models or not.

In general, similar necking and fragmentation characteristics are observed in these models. As expected, thicker models demanded more steps of strain application before fragmentation occurs. The number of steps taken and the amount of elongation attained has been summarized in **Table 3.1**. As mentioned before, application of fast strain (10%) leads to a higher number of necking initiation points which occur at earlier steps. This leads to fragmentation, which occurs before complete necking along the length of the material leaving regions of two atomic arrays in 1A-1K-F model. Increasing the width by one more array of atoms results in a great deal of increase in the number of necking initiation points in 2A-1K-F model (**Figure 3.9**), whereas in thicker models such as 3A-1K-F model (**Figure 3.10**) and 4A-1K-F model (**Figure 3.11**), same trend of increase in the number of necking initiation points continue, but in a lesser extent.

**Table 3.1** The percent of elongation values that the SiNR models have attained one step before the fragmentation. Entries in the parenthesis show the number of steps of strain application required to fragment the SiNR models considered.

| **Elongation (%)** | | **1A** | **2A** | **3A** | **4A** |
|---|---|---|---|---|---|
| **1 K** | **F(%10)** | 94.87 (8) | 245.23 (14) | 317.72 (16) | 359.50 (17) |
| | **S(%5)** | 152.70 (20) | 207.15 (24) | 376.49 (33) | 508.14 (38) |
| **300 K** | **F(%10)** | 135.79 (10) | 245.23 (14) | 359.50 (17) | 455.99 (19) |
| | **S(%5)** | 165.33 (19) | 255.57 (27) | 376.49 (33) | 479.18 (37) |

Another common point in the thicker models is that, fragmentation occurs near the border of the regions between two array of atoms and one array of atoms (atomic chains) rather than breaking in the midst of a region of one atomic array where necking has developed to an extent. In thicker models, necking spreads faster than it occurs in thinner models, as an instance, a necking initiation point may easily evolve into a 1D line of six, seven, or more atoms in the following step in thicker models. Thinning dislocations of thicker models follow a similar pattern. For example, the 4A-1K-F model in **Figure 3.11** is comprised of five arrays of atoms after first relaxation and in the following steps, it gradually elongates and thins to four arrays of atoms and then to three and so on until it becomes fragmented. In the light of this information, we can conclude that in thicker SiNR models, which are formed of many arrays of atoms, the topmost arrays move in a dislocation motion toward the necking initiation points or necking initiation regions from where a necking initiation point would form in a few more steps. From this, it can be comprehended that SiNR has no brittle behavior even under fast mode of strain application but occurrence of thinning dislocations at very early steps, which are not reversible, reveal that the yield strength of the material is not very high. Thereby, it

can be concluded that SiNR models are neither strong in terms of yield strength, nor they are resilient.

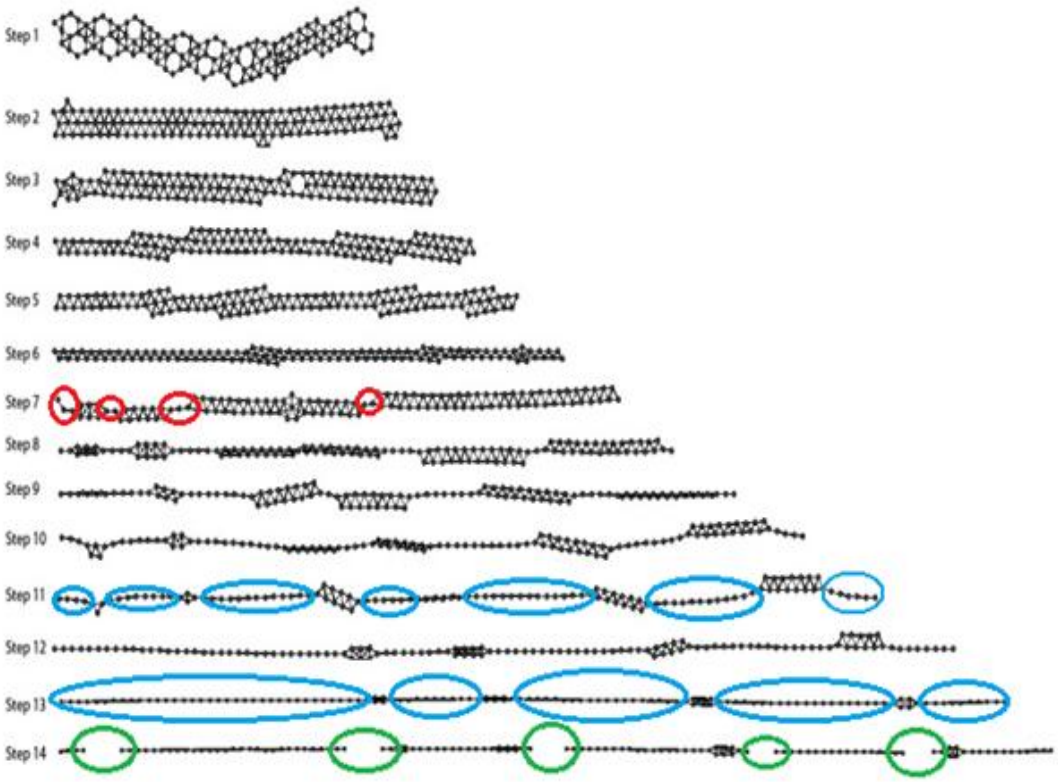


**Figure 3.9** Behavior of 2A-1K-F model SiNR under uniaxial strain. Fragmentation has occurred at the 14$^{th}$ step of %10 strain application. Red color indicates necking initiation points, blue color indicates regions of necking development and green color indicates fragmented regions.

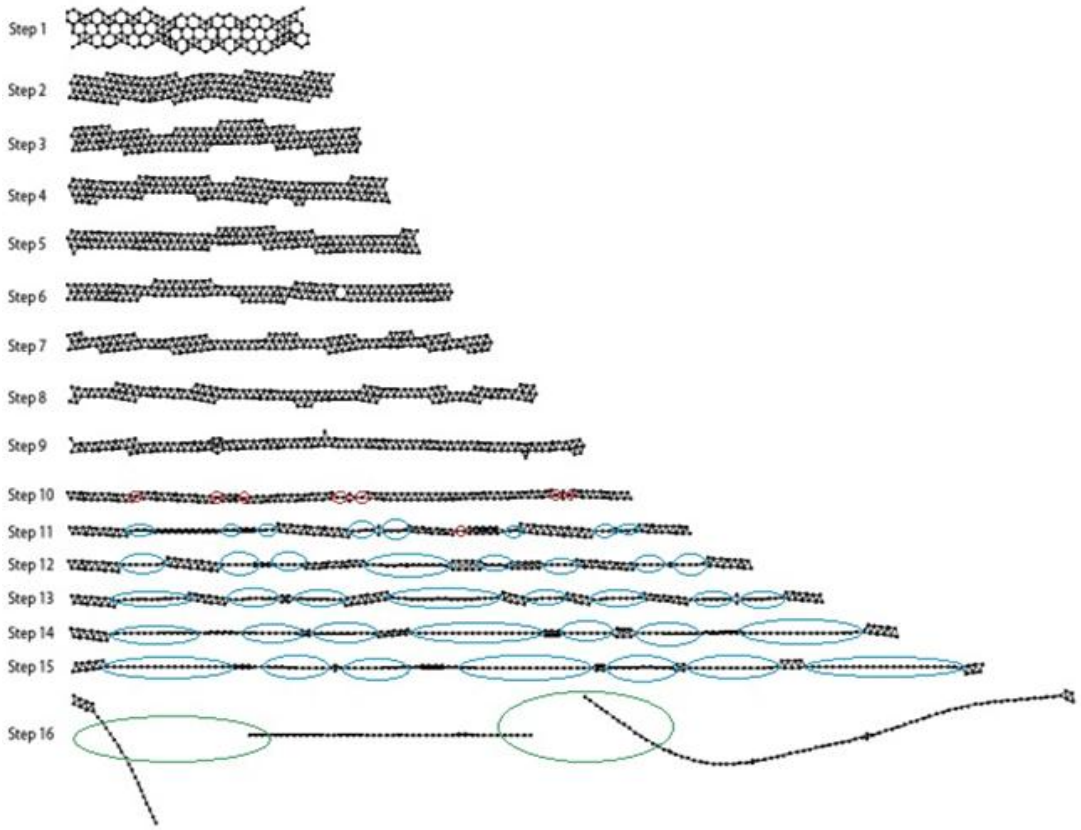


**Figure 3.10** Behavior of 3A-1K-F model SiNR under uniaxial strain. Fragmentation has occurred at the 16$^{th}$ step of %10 strain application. Red color indicates necking initiation points, blue color indicates regions of necking development and green color indicates fragmented regions.

It has been observed that similar necking and fragmentation behavior at 300K counterparts of the previous four models occur: as in 1A-300K-F (**Figure 3.7**), 2A-300K-F (**Figure 3.13**), 3A-300K-F (**Figure 3.14**), and 4A-300K-F (**Figure 3.15**) models. The only difference here is that at 300 K° temperature, fragmented pieces of SiNR form curvy structures and these structures resemble more to a silicon nanotube as the width increases. In addition to this, a comparison of these four models reveals that more regions of two atomic arrays can be encountered at the last step before fragmentation and the number of such regions increase as the SiNR gets thicker.

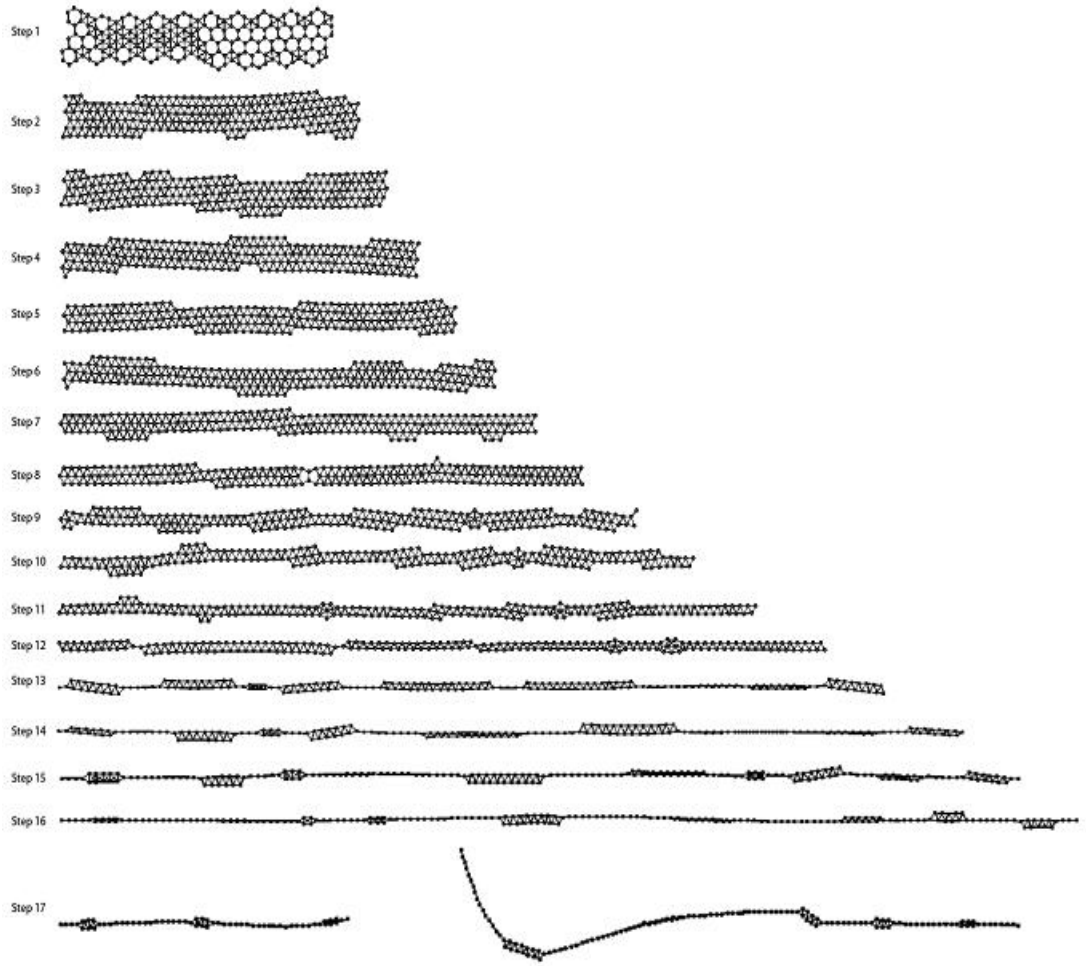


**Figure 3.11** Behavior of 4A-1K-F model SiNR under uniaxial strain. Fragmentation has occurred at the 17$^{th}$ step of %10 strain application.

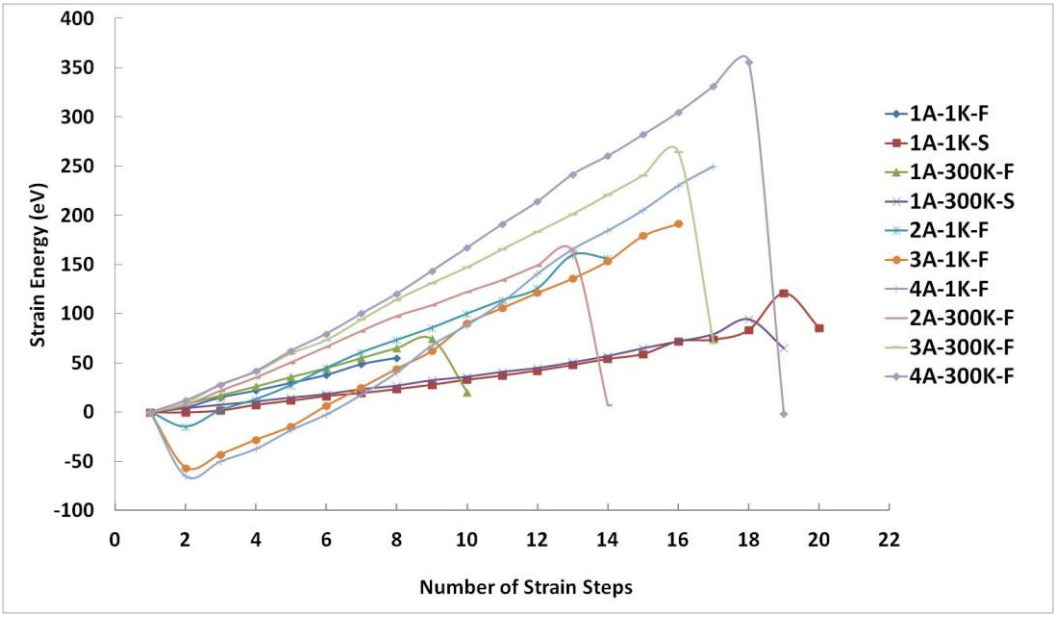


**Figure 3.12** Strain energies of different SiNR models with respect to the increasing amount of strain.

Silicon is a very interesting material: its nanostructures show quite different structural and physical properties with respect to their bulk counterparts; even it shows very interesting structural properties at nanoscale whether periodic boundary is applied or not [122]. Furthermore, temperature has a very important effect on SiNR structures: as mentioned before, it has a greater viscoelasticity (and thereby toughness), in other words, it absorbs more energy under heat treatment since silicon diffusion is promoted due to the increased kinetic energy. This characteristic is clearly seen in strain energy versus strain energy graph given in **Figure 3.12**.

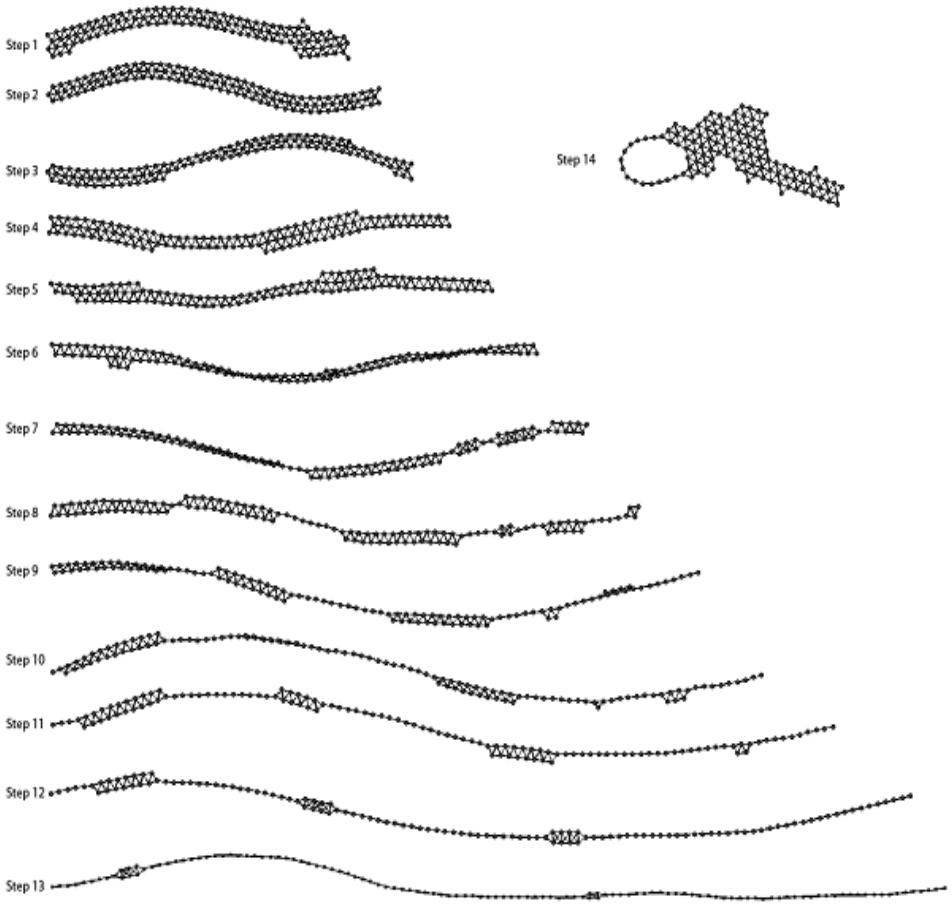


**Figure 3.13** Behavior of 2A-300K-F model SiNR under uniaxial strain. Fragmentation has occurred at the 14$^{th}$ step of %10 strain application.

Here, we define the strain energy ($E_s$) as the difference between the total energy of the system at a strain step n ($E_n$) and the total energy of the system before strain application ($E_0$), namely, $E_s$-$E_n$=$E_0$. These findings show quite similar trends as obtained in graphene nanoribbons [125].

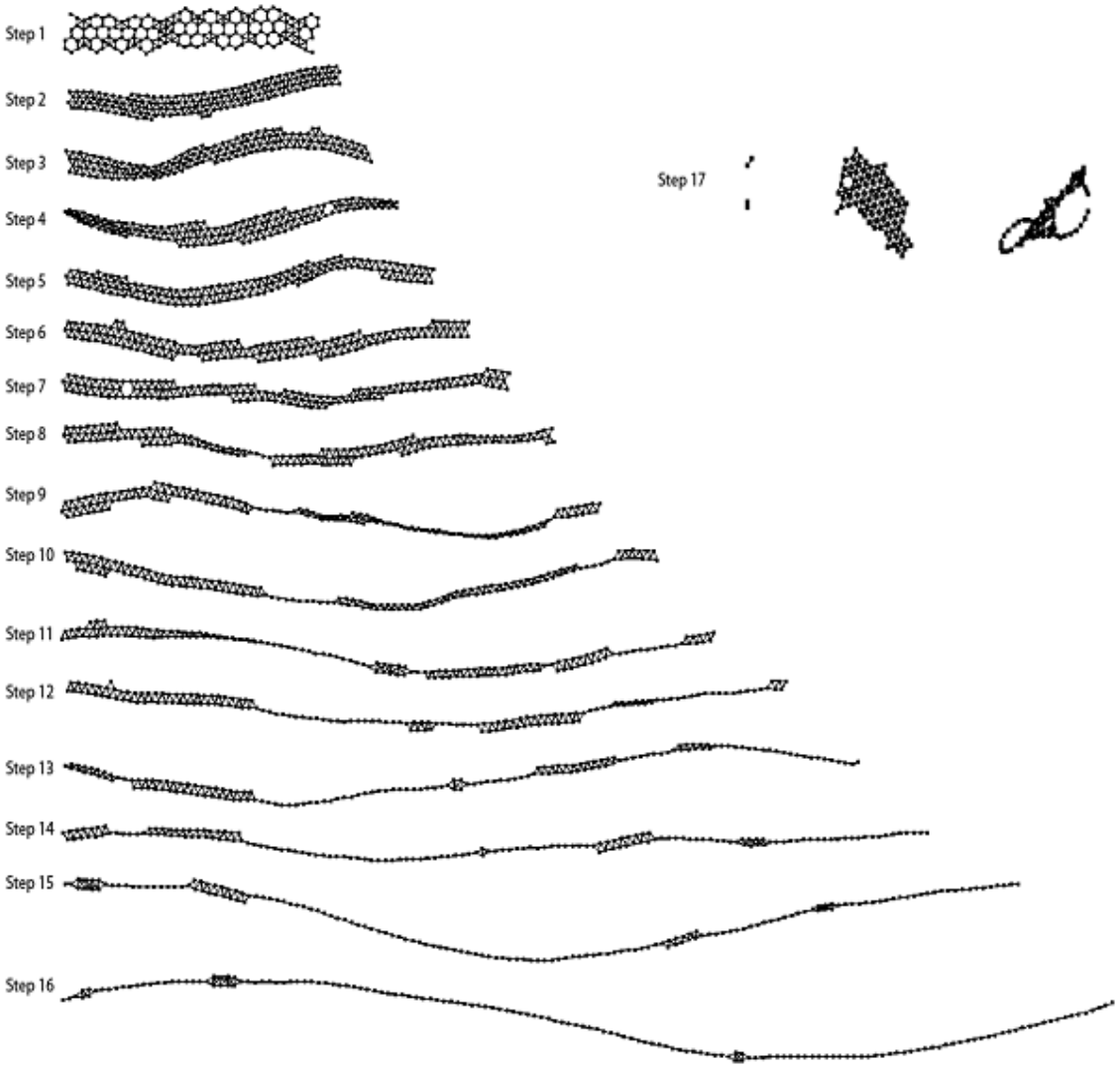


**Figure 3.14** Behavior of 3A-300K-F model SiNR under uniaxial strain. Fragmentation has occurred at the 17th step of %10 strain application.

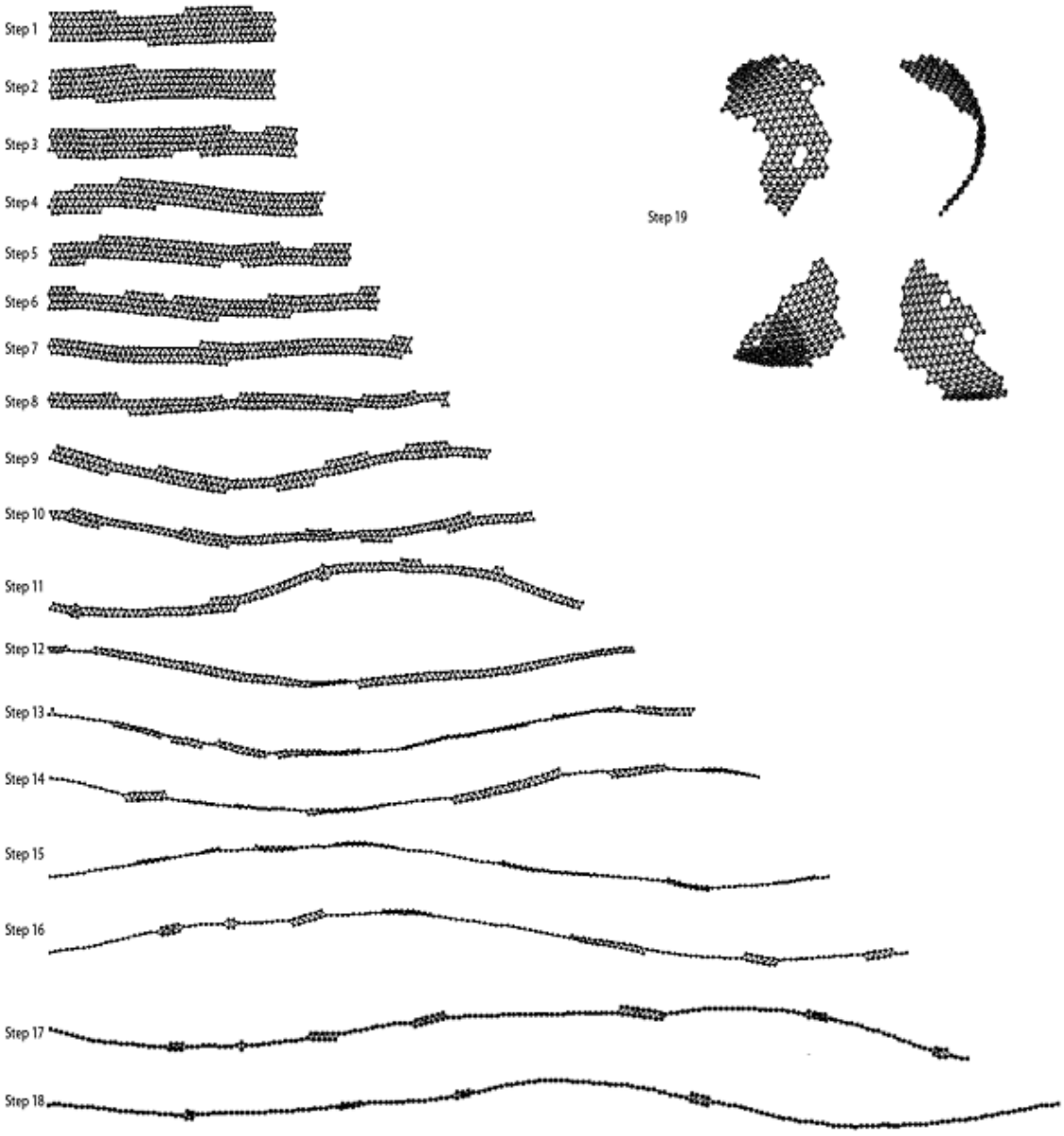


**Figure 3.15** Behavior of 4A-300K-F model SiNR under uniaxial strain. Fragmentation has occurred at the 19th step of %10 strain application.

# CHAPTER IV

# CONCLUSION

Silicene nanoribbons (SiNRs), which are two dimensional honeycomb structures made up of only silicon atoms, are a very recently developed group of materials derived from the idea of graphene nanoribbons, which may find a great deal of applications in a wide range of areas.

In the first part of this work, we have applied molecular dynamics simulations on this novel material in order to comprehend its structural properties. We have made calculations of SiNRs of six different widths, three different lengths, two different temperatures and two different cases in terms of the presence of boundaries, one with periodic boundary and one without; as a whole 72 different models have been considered.

The effect of increasing width of a SiNR depends on the temperature and presence or absence of boundaries. Even though at 1 K°, there were a varying number of the honeycombs, at room temperature, they are all replaced by triangles. At 1 K°, PB models show triangularization only at edges and the percentage ratio of triangles decrease as the width increases. At NoPB models, the trend is reverse, showing the movement of the triangularization starting from one edge towards the other. Presence of periodic boundary generally leads to twisting action, since the SiNR wouldshrink otherwise but it cannot for the boundaries avoid the movement of atoms at the rightmost and leftmost edges, this is the response that the material gives to the restriction of boundaries. At 300 K°, there is complete triangularization of the

whole structure in both PB and NoPB models, where NoPB models end up in tubular forms rather than straight sheets of SiNRs.

The effect of increasing length of a SiNR depends as well on the other two factors; temperature and the presence of boundary. At 1 K-PB, triangular portions are equally distributed among the hexagonal honeycombs. But when the boundary is lifted off, we see that extending the SiNR along the length leads to the movement of triangularization. At 300 K°, the whole SiNR is composed of triangles as mentioned, but what is so interesting here is that at NoPB case length increase leads to the folding of the SiNR into tubular or curvy structures, mostly in the form of silicon nanotubes.

Although both graphene and silicene are 2D nanomaterials, the main difference between graphene (honeycomb structure made of carbon) and silicene is in the geometry of their structures. Graphene is composed of hexagons, whereas silicene is composed of triangles. Both structures are stable at room temperature. In device applications of SiNRs, one should pay attention to how the SiNRs will be used as part of a device, whether they will be used as finite length free materials or attached at two ends. The present study elucidates the structural properties of SiNRs for both cases. But if this novel material is to be used in an attached fashion at its two ends, more information about the mechanical properties of this novel material would be necessary. Under uniaxial tension, this material may show some interesting properties.

In the second part of this study, uniaxial strain has been applied over SiNR models to investigate mechanical properties of SiNR sheets. This test has been applied over models of four different widths (nA where n=1–4) and same length at two different temperatures (1 K°, 300 K°) and two different strain modes; at slow mode (5% strain per step) and at fast mode (10% strain per step). Primarily, strain has been applied over SiNR models and then relaxation followed until the material is fragmented. In all models, thinning into a one single array of atoms which can be

called as necking starts at a single point. Then, due to the dislocation of atoms from a second layer toward these single points, these regions evolve into 1D atomic chains, which develop into a fragment. In 1A-1K-S model, necking initiation points appear at later steps which are distributed evenly along the length of the SiNR whereas in 1A-1K-F mode, there are many necking initiation points which transform into many regions of fragmentation at many different points in the end.

In models simulated at 300 K°, less necking initiation points are encountered, thereby fragmentation occurs at more steps of strain. Especially, in 1A-300K-S model, starting from a single necking initiation point in the middle, the whole model transforms into a single array of atoms like a silicon atomic chain in a very smooth way. 1K models (**Figures 3.5, 3.9, 3.10 and 3.11**) and 300K models (**Figures 3.7, 3.13, 3.14, and 3.15**) of increasing width generally seem to follow the general trends discussed before in the first four models compared (**Figures 3.5, 3.6, 3.7 and 3.8**).

1K models have a tendency to start necking earlier with more necking initiation points leading to fragmentation at many different points of a one long single array of atoms whereas 300K models start necking at lesser amount of points but after fragmentation, the fragmented pieces tend to form curvy structures. Different and/or more interesting structural features may take place at elevated temperatures for this particular material.

The present simulation method does not allow us to draw a reliable stress–strain curve, which would reveal a great deal of quantitative information about yield strength, ultimate tensile strength and toughness. However, it is still possible to infer from the resulting structures and the strain energies of different SiNR models that this material shows high ductility, high toughness and low yield strength. Comparison of strain energies of the same models at two different temperatures reveals that SiNRs have increased viscoelasticity due to the temperature increase.

# REFERENCES

[1] N. Taniguchi, On the Basic Concept of 'NanoTechnology', Proc. Intl. Conf. Prod. Eng. Tokyo Part II, Tokyo: Japan Society of Precision Engineering, 1974.

[2] J. Mongillo, Nanotechnology 101, Greenwood Press, 2007.

[3] What is nanotechnology?, http://nano.gov/nanotech-101/what/definition (accessed on 02.01.2012).

[4] K. E. Drexler, Engines of Creation, Anchor Books New York, 1986.

[5] The promise that launched the idea of nanotechnology, http://metamodern.com/ 2009/12/15/when-a-million-readers-first-encountered-nanotechnology (accessed on 02.01.2012).

[6] J. Ramsden, Essentials of Nanotechnology, BookBoon, 2009.

[7] Nanotechnology, http://nanotechnology.com (accessed on 02.01.2012).

[8] Optical Microscope, http://en.wikipedia.org/wiki/Optical_microscope (accessed on 02.01.2012).

[9] B.Fultz and J. Howe, Transmission Electron Microscopy and Diffractometry of Materials, Springer, 2007.

[10] M.Knoll, Zeitschrift für technische Physik, **16**: 467–475, 1935.

[11] G. Binnig and H. Rohrer, IBM Journal of Research and Development, **30**: 4, 1986.

[12] Press release for the 1986 Nobel Prize in physics, http://www.nobelprize.org/ nobel_prizes/physics/laureates/1986/press.html (accessed on 02.01.2012).

[13] C. Bai, Scanning tunneling microscopy and its applications, Springer-Verlag New York, 2000.

[14] D. A. Bonnell and B. D. Huey,Basic principles of scanning probe microscopy. In D. A. Bonnell. Scanning probe microscopy and spectroscopy: Theory, techniques, and applications (2 ed.), Wiley-VCH New York,2001.

[15] L. Williams and W. Adams, Nanotechnology Demystified, Mc-Graw Hill New York, 2007.

[16] B.D.Fahlman, Materials Chemistry, Springer Dordrecht-Heidelberg London New York, 2011.

[17] Y.Leng, Materials Characterization Introduction to Microscopic and Spectroscopic Methods, John Wiley & Sons, 2008.

[18] K.Siddharth, Experimental Probability, http://www.experiment-resources.com/ experimental-probability.html (accessed on 02.01.2012).

[19] J.R. Taylor, An Introduction to Error Analysis: The Study of Uncertainties in Physical Measurements 2nd Edition, University Science Books, 1997.

[20] L. Verlet, Mol. Phys. Rev., **159**: 98-103, 1967.

[21] A. Nordsieck, Math. Comput.,**16**: 22, 1962.

[22] M. Born and J. R. Oppenheimer, Ann. Physik, **84**: 457, 1927.

[23] M. Born and K. Huang, Dynamical Theory of Crystal Lattices, Oxford University Press Oxford, 1954.

[24] A. Satoh, Introduction to the Practice of Molecular Simulation, Elsevier, 2011.

[25] D.W. Heermann, Computer Simulation Methods, Springer-Verlag Berlin Heidelberg New York, 1990.

[26] N. Metropolis and J. Ulam, Am. star.Ass.,**44**: 335, 1949.

[27] M.P. Allen and J.P. Tildesley, Molecular Simulation of Liquids, Clarendon Press Oxford, 1987.

[28] F.Jensen, Introduction to Computational Chemistry, John Wiley & Sons, 1999.

[29] D.Marx and J. Hutter, Ab initio Molecular Dynamics Basic Theory and Advanced Methods, Cambridge University Press, 2009.

[30] S.M.Blinder, Introduction to Quantum Mechanics in Chemistry Material Science and Biology, Elsevier Academic Press: Amsterdam, 2004

[31] A.R.Leach, Molecular Modeling Principles and Applications, Pearson Education Limited, 2001.

[32] M.Springborg, Methods of Electronic Structure Calculation, John Wiley & Sons, 2000.

[33] A. Szabo and N.S. Ostlund, Modern Quantum Chemistry: Introduction to Advanced Electronic Structure Theory, McGraw-Hill New York, 1989.

[34] C. Møller and M.S. Plesset, Phys. Rev., **46**: 618, 1934.

[35] W. Kohn and L. J. Sham, Phys. Rev., **140**: A1133, 1965.

[36] W.Kohn, Nobel Lecture: Electronic structure of matter—wave functions and density functionals

[37] K. Burke, ABC of DFT, University of California, Irvine, 2007.

[38] R M. Martin, Electronic structure Basic Theory and Practical Methods, University Press, Cambridge, 2004.

[39] G. E. Scuseria and V. N. Staroverov, Progress in the development of Exchange-Correlation, Elsevier Amsterdam, 2006.

[40] J. Kohanhoff and N.I. Gidopoulos, Density Functional Theory: Basics New Trends And Applications Volume 2, Part 5, Chapter 26, pp 532–568 in Handbook of Molecular Physics and Quantum Chemistry, Wiley, 2003.

[41] J. L. Wintterlin and M.-L. Bocquet, Surf. Sci., **603**: 1841, 2009.

[42] K.S.Novoselov, A. K. Geim, S. V. Morozov, D. Jiang, M. I. Katsnelson, I. V. Grigorieva, S. V. Dubonos, and A. A. Firsov, Nature **438**: 197, 2005.

[43] C. Kane, Nature, **438**: 168, 2006.

[44] Guzman-Verri, Electronic Properties of Silicon Based Nanostructures, Wright State University, 2006.

[45] K. S. Novoselov, A. K. Geim, S. V. Morozov, D. Jiang, Y. Zhang, S. V. Dubonos, I. V. Grigorieva, and A. A. Firsov, Science, **306**: 666, 2004.

[46] A. K. Geim and K. S. Novoselov, Nature Mater.,**6**: 183, 2007.

[47] E.F.Sheka, May Silicene Exist?,
http://arxiv.org/ftp/arxiv/papers/0901/09013663.pdf (last accessed on 02.01.2012).

[48] C. Léandri, G. Le Lay, B. Aufray, C. Girardeaux, J. Avila, M. E. Davila, M. C. Asensio, C. Ottaviani, and A. Cricenti, Surf. Sci., **574**: L9, 2005.

[49] A. Kara, H. Enriquez, Ari P. Seitsonen, L.C. Lew Yan Voon, Sébastien Vizzini, B. Aufray and H. Oughaddou, Surf. Sci. Rep., **67**: 1-18, 2012.

[50] U. Bardi, Rep. Prog. Phys., **57**: 939, 1994.

[51] J. Eugene, B.Aufray and F. Cabané, Surf. Sci., **241**: 1, 1991.

[52] Y.Liu and P. Wynblatt, Surf. Sci., **240**:245, 1990.

[53] H. Giordano, O. Alem and B. Aufray, Scr. Metall. **28**: 257, 1993.

[54] I. Meunier, J.M. Gay, L. Lapena, B. Aufray, H. Oughaddou, E. Landemark, G. Falkenberg, L. Lottermoser and R.L. Johnson, Surf. Sci., **422**: 42, 1999.

[55] R. Dudde, H. Bernhoff, B. Reihl, Phys. Rev. B, **41**: 12029, 1990.

[56] M. Göthelid, M. Hammar, M. Björkqvist, U.O. Karlson, S.A. Flodström,C. Wigren, G. Lelay, Phys. Rev. B, **50**: 4470, 1994.

[57] M. Hammar, M. Göthelid, U.O. Karlson, S.A. Flodström, Phys. Rev. B, **47**: 15669, 1993.

[58] D. Dornish, W. Moritz, H. Schulz, R. Feidenhans'l, M. Nielsen, F. Grey,R.L. Johnson and G. Lelay, Surf. Sci., **274**: 215–221, 1992.

[59] G. Lelay, R.L. Johnson, R. Seemann, F. Grey, R. Feidenhans'l and M. Nielsen, Surf.Sci., **287**: 539–544, 1993.

[60] J. Nogami, A.A. Baski and C.F. Quate, Phys. Rev. Lett., **65**:1611, 1990.

[61] C. Polop, J.L. Sacedón, J.A. Martín-Gago, Surf. Sci., 245–248, 1998.

[62] C. Polop, C. Rojas, E. Roman, J.A. Martín-Gago, B. Brena, D. Cocco, G. Paolucci,Surf. Sci., **407**: 268–274,1998.

[63] J.A. Martín-Gago, C. Rojas, C. Polop, J.L. Sacedón and E. Romàn, Phys. Rev. B, **59**: 4, 1999.

[64] J.A. Martín-Gago, R. Fasel, J. Hayoz, R.G. Agostino, D. Naumovi, P. Aebi andL. Schlapbach, Phys. Rev. B, **55**:12896, 1997.

C. Polop, C. Rojas, J.A. Martín-Gago, R. Fasel, J. Hayoz, D. Naumovi and P. Aebi,Phys. Rev. B., **63**: 115414, 2001.

[65] H. Oughaddou, B Aufray, J.P. Bibérian and J.Y. Hoarau, Surf. Sci., **429**:320, 1999.

[66] H. Oughaddou, J.M. Gay, B. Aufray, L. Lapena, G. Le Lay, O. Bunk, G. Falkenberg, J.H. Zeysing and R.L. Johnson, Phys. Rev. B, **61**: 5692, 2000.

[67] J. Dalmas, H. Oughaddou, G. Le Lay, B. Aufray, G. Tréglia, C. Girardeaux, J. Bernardini, Jun Jujii and G. Panaccione, Surf. Sci., **600**: 1227, 2006.

[68] I. Meunier, J.M. Gay, L. Lapena, B. Aufray, H. Oughaddou, E. Landemark,G. Falkenberg, L. Lottermoser and R.L. Johnson, Surf. Sci., **422**: 42, 1999.

[69] H. Giordano and B. Aufray, Surf. Sci., **816**: 307–309, 1994.

[70] R.W. Olesinski and G.J. Abbaschian, Bull. Alloy Phase Diagr.,**9**: 59, 1988.

[71] H. Oughaddou, B Aufray, J.P. Bibérian and J.Y. Hoarau, Surf. Sci., **429**: 320, 1999.

[72] M. Hansen, Metallurgy and Metallurgical Engineering Series, Mc Graw-Hill Book Company, 1958.

[73] G. Le Lay, B. Aufray, C. Leandri, H. Oughaddou, J.P. Bibérian, P. De Padova, M.E. Davila and B. Ealet, Appl. Surf. Sci., **256**: 524–525, 2009.

[74] G. M. He, Phys Rev B, **73**: 035311, 2006.

[75] H. Sahaf, L. Masson, C. Léandri, B. Aufray, G. Le Lay and F. Ronci, Appl. Phys. Lett. **90**: 263110, 2007.

[76] P. De Padova, C. Quaresima, P. Perfetti, B. Olivieri, C. Leandri, B. Aufray, S. Vizzini and G. Le Lay, NanoLett. **8**: 271, 2008.

[77] B. Aufray, A. Kara, S. Vizzini, H. Oughaddou, C. Léandri, B. Ealet and G. Le Lay, Appl. Phys. Lett. **96**: 183102, 2010.

[78] A. Kara, S. Vizzini, C. Léandri, B. Ealet, H. Oughaddou, B. Aufray and G. Le Lay, J. Phys.: Condens. Matter, **22**: 045004, 2010.

[79] B. Lalmi, H. Oughaddou, H. Enriquez, A. Kara, S. Vizzini, B. Ealet and B. Aufray, Appl. Phys. Lett. **97**: 22310, 2010.

[80] Fernandez-Serra, M.-V.; Adessi, Ch.; Blase, X. Nano Lett.,**6 (12)**: 2674–2678, 2006.

[81] P. De Padova, C. Léandri, S. Vizzini, C. Quaresima, P. Perfetti, B. Olivieri, H. Oughaddou, B. Aufray and G. Le Lay, Nano Lett., **8**: 2299, 2008.

[82] P. De Padova, C. Quaresima, B. Olivieri, P. Perfetti and G. Le Lay, J. Phys. D.: Appl. Phys., **44**: 312001, 2011.

[83] A. Kara, C. Léandri, M.E. Davila, P. De Padova, B. Ealet, H. Oughaddou, B. Aufray and G. Le Lay, J. Supercond Nov Magn, **22**:259-263, 2009.

[84] S. Cahangirov, M. Topsakal, E. Aktürk, H. Sahin, S. Ciraci, Phys. Rev. Lett. **102**: 236804, 2009.

[85] M. Topsakal, S. Ciraci, Phys. Rev. B, **81**: 024107, 2010.

[86] Y.L. Song, Y.Zhang, J.M. Zhang and D.B. Lu, Appl. Surf. Sci., **256**: 6313–6314, 2010.

[87] Y.L. Song, Y. Zhang, J.M. Zhang, D.B. Lu and K.W. Xu, Appl. Surf. Sci., **990**: 75, 2011.

[88] N. Y. Dzade, K. O. Obodo, S. K. Adjokatse, A. C. Ashu, E. Amankwah, C. Atiso, A. A. Bello, E. Igumbor, S. B. Nzabarinda, J. T. Obodo, A. O. Ogbuu, O. E. Femi, J. O. Udeigwe, and U. V. Waghmare, J. Phys. Condens. Matter, **22**: 375502, 2010.

[89] J.M.Finn, Classical Mechanics, Jones and Bartlett, 2010.

[90] M.E.Tuckerman, Statistical Mechanics Theory and Simulation, Oxford University Press Inc., 2010.

[91] A.Deriglazov, Classical Mechanics Hamiltonian and Lagrangian Mechanics, Springer Verlag Berlin Heidelberg, 2010.

[92] N.M. Laurendeau, Statistical Thermodynamics Fundamentals and Applications, Cambridge University Press, 2005.

[93] Molecular Dynamics at Constant Temperature, http://www.pages.drexel.edu/~cfa22/msim/node33.html (accessed on 04.01.2012).

[94] H. J. C. Berendsen, J. P. M. Postma, W. F. van Gunsteren, A. DiNola, and J. R. Haak., Molecular dynamics with coupling to an external bath, *J. Chem. Phys.*, **81(8)**: 3684-90, 1984.

[95] Molecular Dynamics (Wikipedia), http://en.wikipedia.org/wiki/Molecular_dynamics (last accessed on 05.01.2012).

[96] H. C. Andersen, *J. Chem. Phys.*, **72**: 2384-2393, 1980.

[97] G. S. Grest and K. Kremer, Phys. Rev. A, **33(5)**: 3628-3631, 1986.

[98] P. Nikunen, M. Karttunen, and I. Vattulainen,Comput. Phys. Comm., **153(3)**: 407-423, 2003.

[99] T. Soddemann, B. Dünweg, and K. Kremer, Phys. Rev. E, **68(4)**: 046702, 2003.

[100] W.G. Hoover, Computational Statistical Mechanics, Elsevier Amsterdam, 1991.

[101] L. Verlet, Phys. Rev., **159**: 98–103, 1967.

[102] C. Störmer, Arch. Sci., **24:** 5–18, 113–158, 221–247, 1907.

[103] R. D. Skeel, BIT, **33:** 172–175, 1993.

[104] D. Frenkel and B. Smit, Understanding Molecular Simulation: From Algorithms to Application, Academic Press New York, 1996.

[105] C.W.Gear, Rep. ANL-7126, Argonne National Laboratory, 1966.

[106] C.W.Gear, Numerical Initial Value Problems in Ordinary Differential Equations, New Jersey, 1971.

[107] G.Ciccotti, W.G.Hoover, Molecular Dynamics Simulations of Statistical Mechanical Systems, E. Fermi 1985 Summer School. G. Ciccotti and W. G. Hoover Eds. North Holland, Amsterdam, 1986.

[108] M. Rieth, Nano-engineering in Science and Technology: An Introduction to the World of Nano-Design, World Scientific, Singapore, 2003.

[109] H.J.C. Berendsen and W.F. Van Gunsteren, Molecular Dynamics Simulations of statistical mechanics systems, 1986.

[110] S.Erkoc, Annual Reviews of Computational Physics IX, **9**:1-103, 2001.

[111] S.Erkoc, Physics Reports, **278**: 79, 1997.

[112] E. Pearson, T. Takai, T. Halıcıoğlu, and W. A. Tiller, J. Cryst. Growth, **70**: 33, 1984.

[113] J. E. Lennard-Jones, Proc. R. Soc. A,**106**: 441, 1924.

[114] B. M. Axilrod and E. Teller, J. Chem. Phys., **11**: 299, 1943.

[115] S. Erkoc, T. Halicioglu, and W. A. Tiller, J. Non-Cryst. Solids, **94**: 28, 1987.

[116] T. Takai, Computer Simulation of Silicon, Carbon, Silicon Carbide and Gold: Surface Processes and Energetics, Ph.D. Thesis, Stanford University, 1984.

[117] S. Katircioglu and S. Erkoc, Physica E, **9**: 314, 2001.

[118] H. Balamane, T. Halicioglu, and W. A. Tiller, Phys. Rev. B, **46**:2250, 1992.

[119] J. M. Haile, Molecular Dynamics Simulation Elementary Methods, Wiley, 1992.

[120] C. Kittel, Introduction to Solid State Physics, John Wiley & Sons-NY, 1986.

[121] S. Cihangirov, M. Topsakal, E. Akturk, H. Sahin, and S. Ciraci, Phys. Rev. Lett., **102**:236804, 2009.

[122] Erkoç, S., Simulations of Many Particle Systems, Lecture/Class, Middle East Technical University, unpublished, 2004.

[123] A. Ince and S. Erkoc, Comput.Mater. Sci., **50**:865-870, 2011.

[124] A. Ince and S. Erkoc, Phys. Status Solidi B, **249**:74-81, 2012.

[125] M. Topsakal, V. M. K. Bagci, and S. Ciraci, Phys. Rev. B,**81**:205437, 2010.

[126] D. Jose and A. Datta, Phys. Chem. Chem. Phys., **13**: 7304-7311, 2011.

# APPENDIX A

# A SUMMARY OF THE MOLECULAR DYNAMICS SIMULATION TECHNIQUE

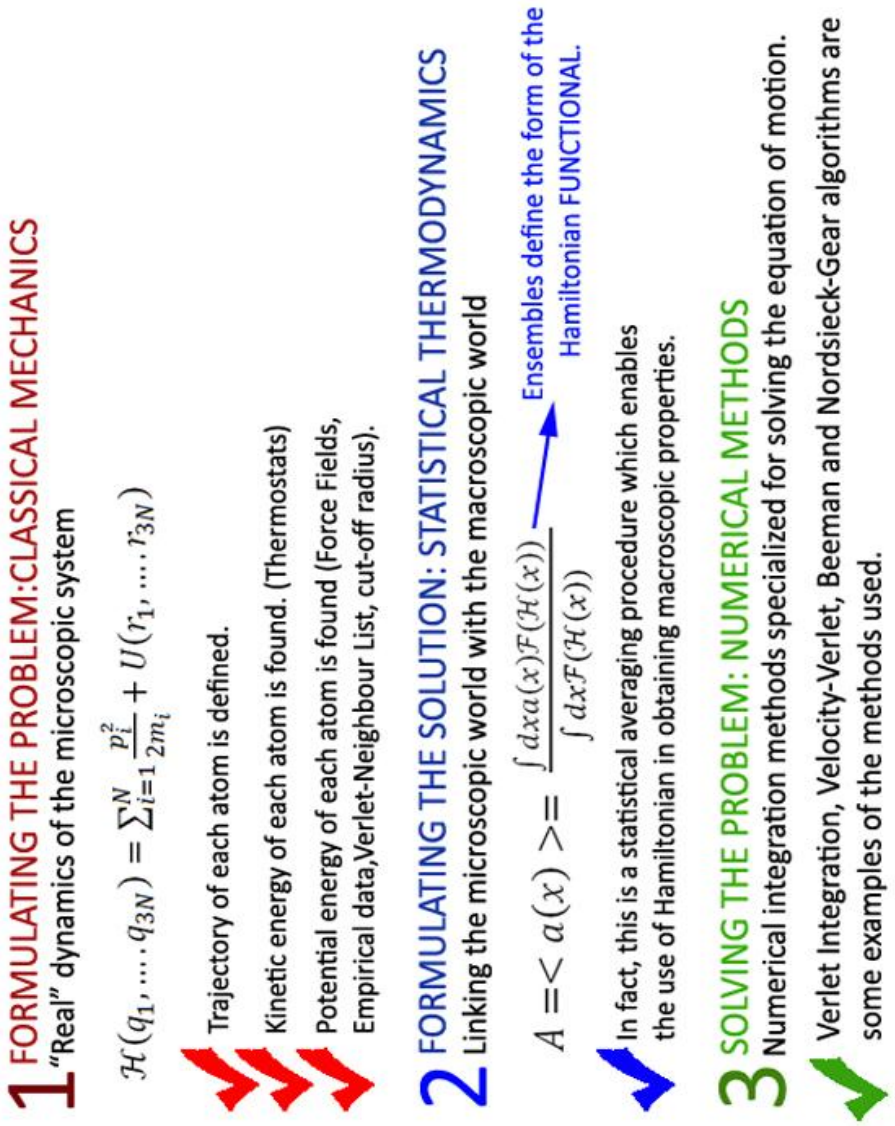


**Figure A.1** A summary of the molecular dynamics simulation technique.

# APPENDIX B

# A SUMMARY OF THE FORTRAN MOLECULAR DYNAMICS CODE

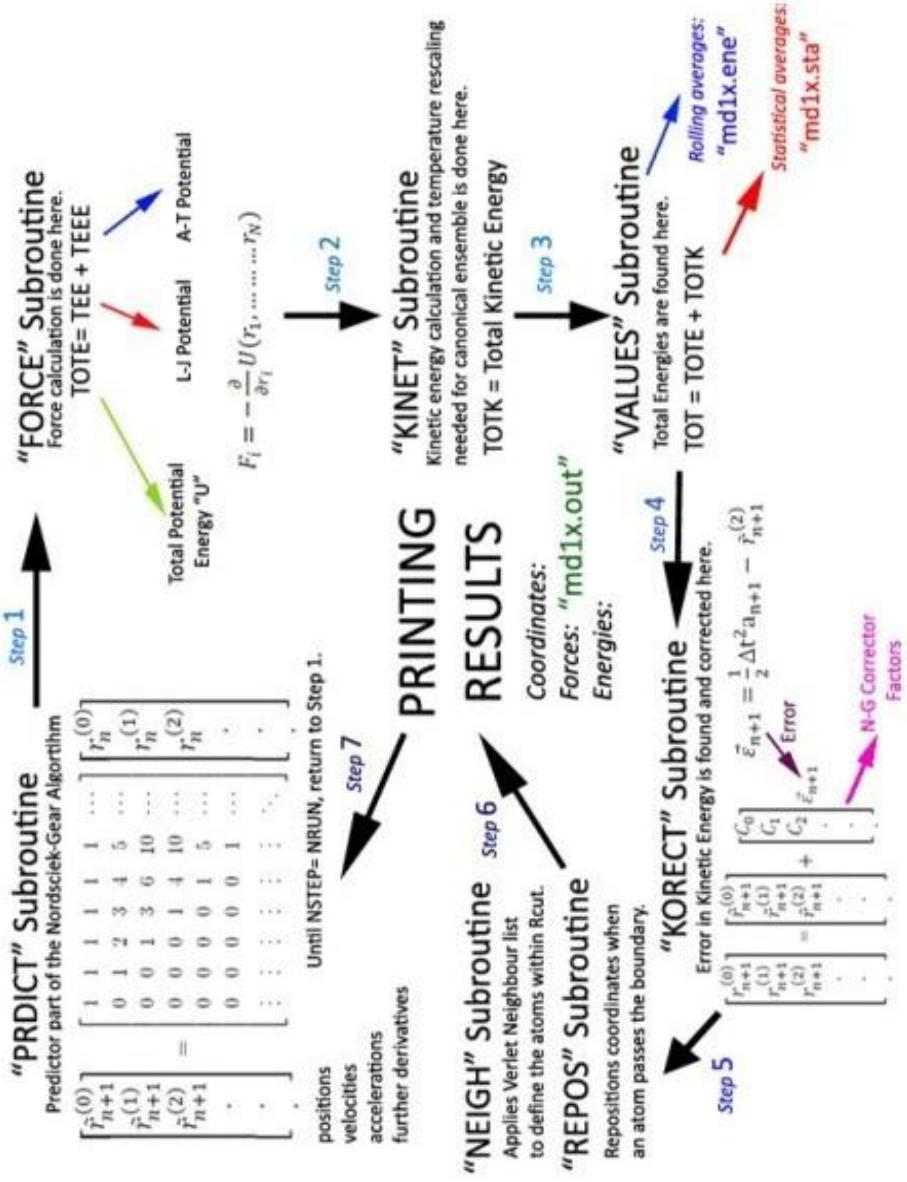


**Figure B.1** A summary of the molecular dynamics simulation technique.

# APPENDIX C

# IMAGES OF VARIOUS SiNR STRUCTURES

## C.1 Relaxed SiNR Structures

In this section, the relaxed SiNR structures found in the first part of the study which are not included in the Chapter 3 are shown. The images had to be shown at different scales due to the sizing issues of the images to fit the format of this thesis. But however, the length and width of the SiNR sheets would be sufficient to give a feeling of size if different SiNR structures are compared. In some images, more than two different views of the structure are given so that the details of the geometry of the structure become more obvious.

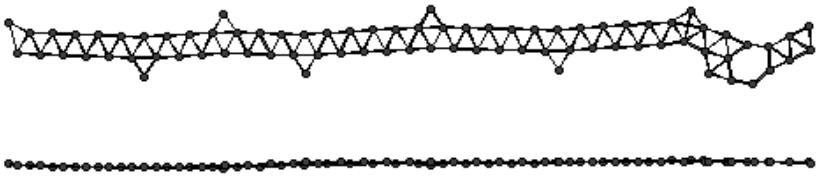

**Figure C.1** Images of relaxed 1A-1K-20H-PB model; top view (on top) and side view (at the bottom).

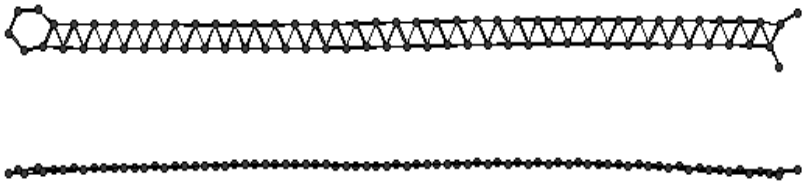

**Figure C.2** Images of relaxed 1A-1K-20H-NoPB model; top view (on top) and side view (at the bottom).

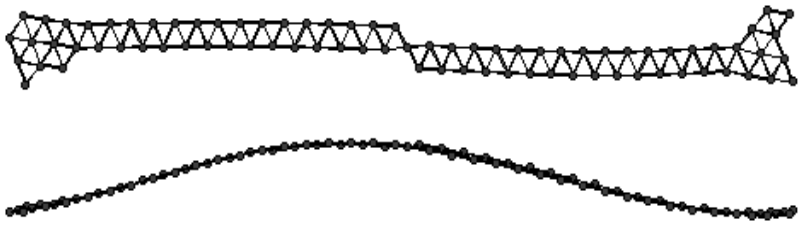

**Figure C.3** Images of relaxed 1A-300K-20H-PB model; top view (on top) and side view (at the bottom).

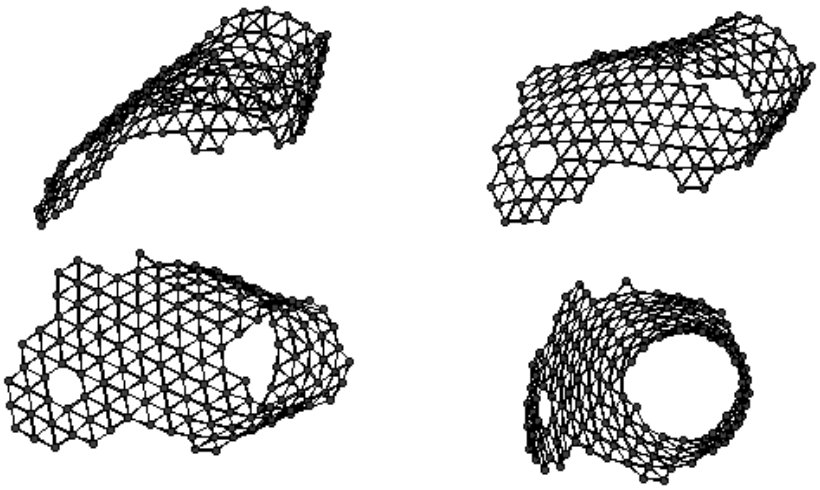

**Figure C.4** Images of relaxed 1A-300K-20H-NoPB model;four different views of the final 3-D wrapped silicon sheet structure is given.

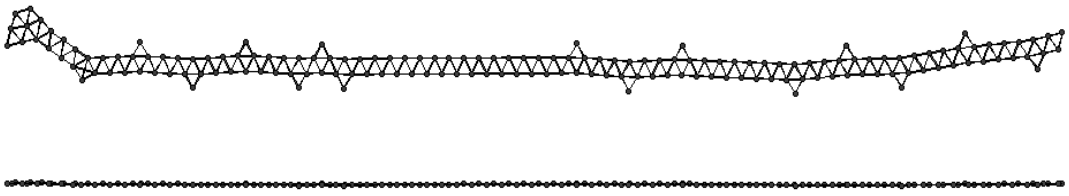

**Figure C.5** Images of relaxed 1A-1K-40H-PB model; top view (on top) and side view (at the bottom).

**Figure C.6** Images of relaxed 1A-300K-40H-NoPB model;two different views of the structure is given.

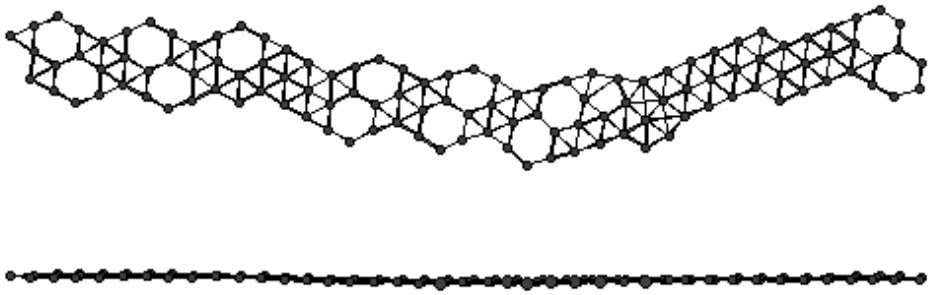

**Figure C.7** Images of relaxed 2A-1K-20H-PB model; top view (on top) and side view (at the bottom).

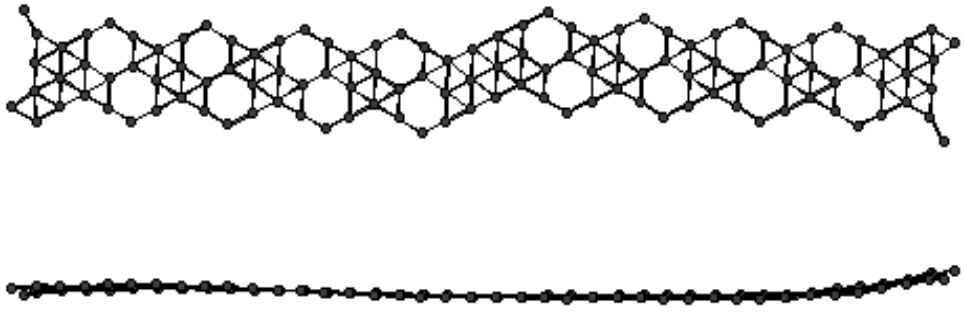

**Figure C.8** Images of relaxed 2A-1K-20H-NoPB model; top view (on top) and side view (at the bottom).

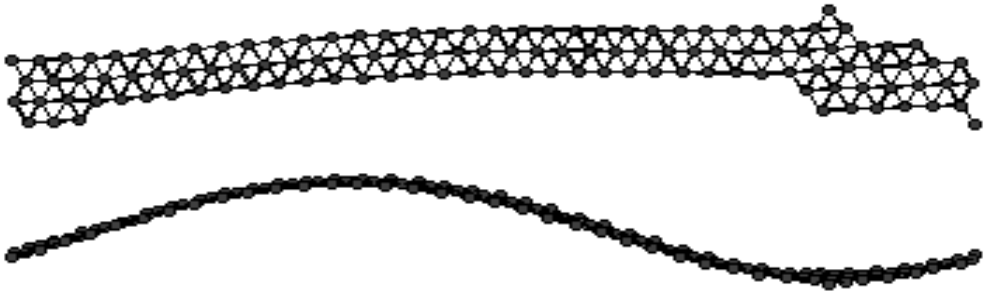

**Figure C.9** Images of relaxed 2A-300K-20H-PB model; top view (on top) and side view (at the bottom).

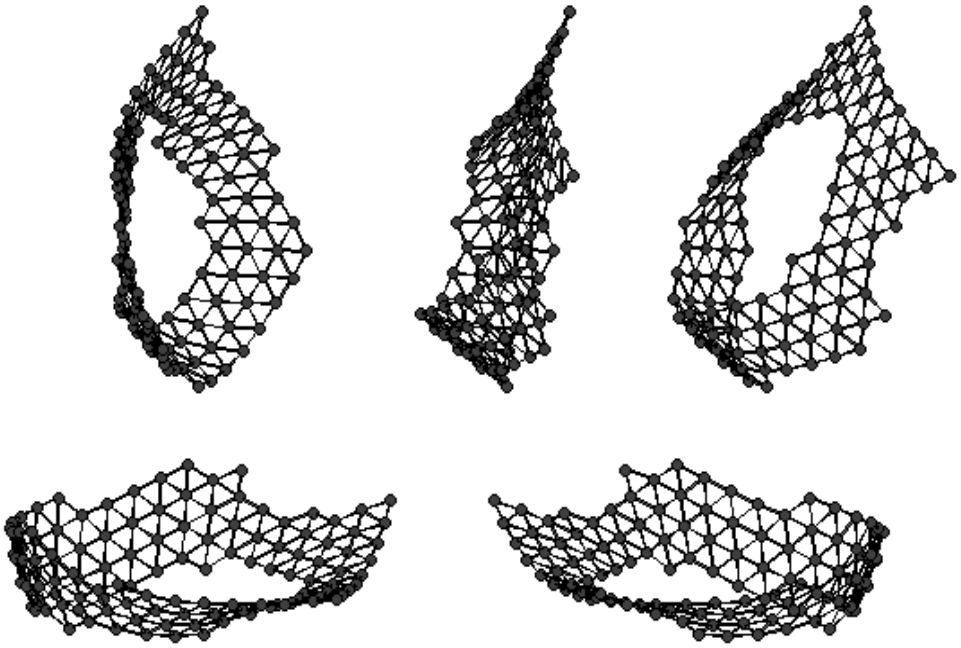

**Figure C.10** Images of relaxed 2A-300K-20H-NoPB model; five different views of the structure is given.

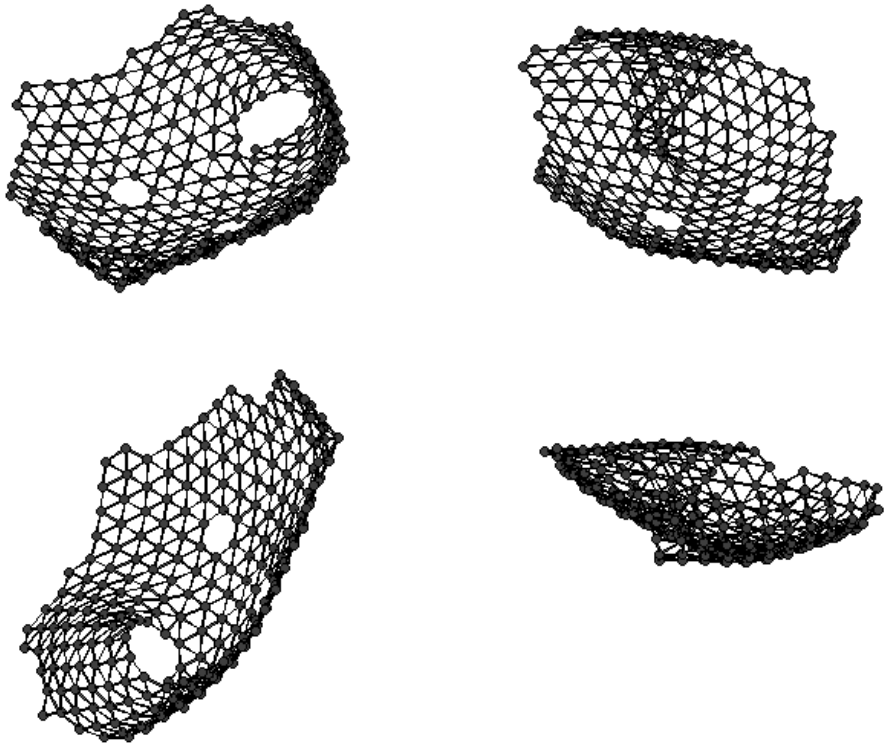

**Figure C.11** Images of relaxed 2A-300K-40H-NoPB model;four different views of the structure is given.

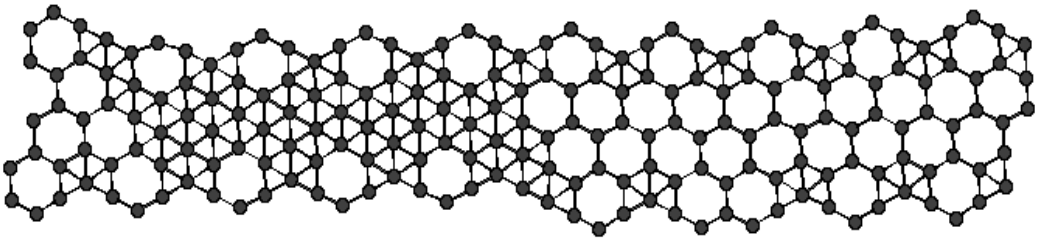

**Figure C.12** Image of relaxed 4A-1K-20H-PB model (top view).

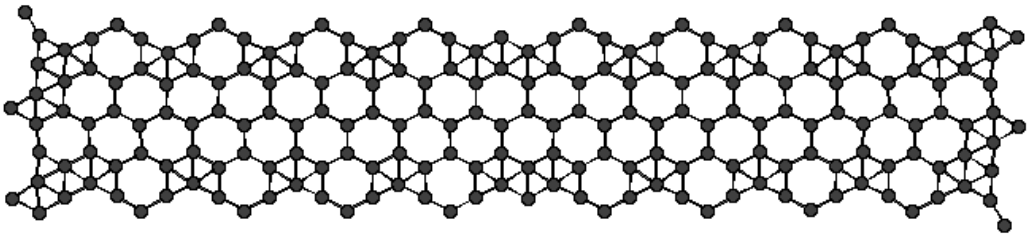

**Figure C.13** Image of relaxed 4A-1K-20H-NoPB model (top view).

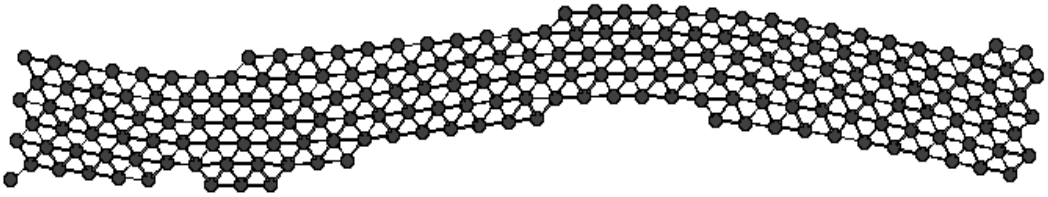

**Figure C.14** Image of relaxed 4A-300K-20H-PB model (top view).

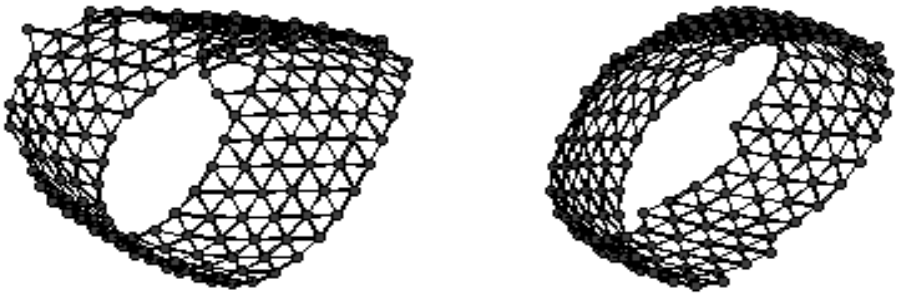

**Figure C.15** Images of relaxed 4A-300K-20H-NoPB model; two different views of the structure is given.

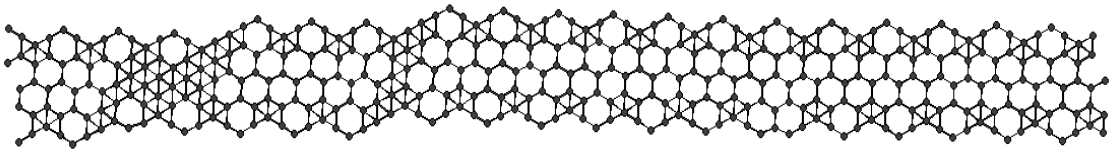

**Figure C.16** Image of relaxed 4A-1K-40H-PB model (top view).

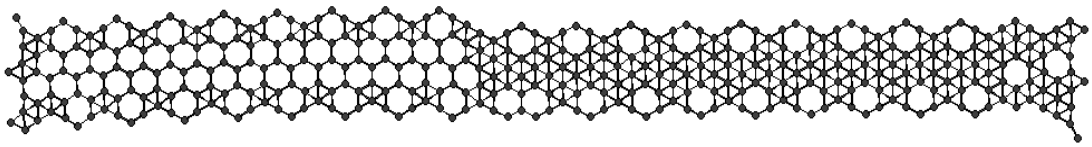

**Figure C.17** Image of relaxed 4A-1K-40H-NoPB model (top view).

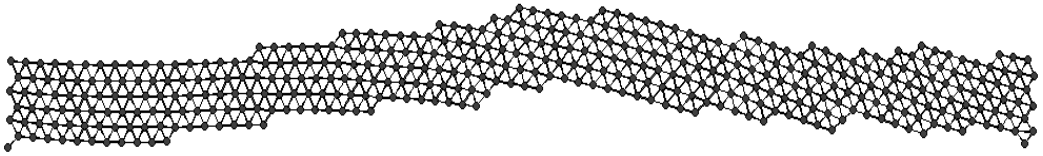

**Figure C.18** Image of relaxed 4A-300K-40H-PB model (top view).

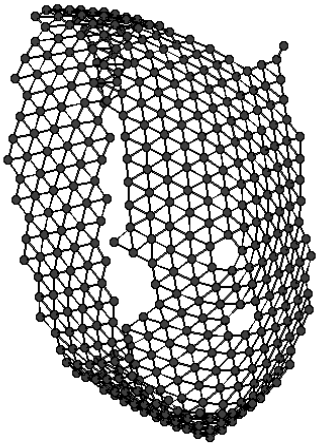

**Figure C.19** Image of relaxed 4A-300K-40H-NoPB model.

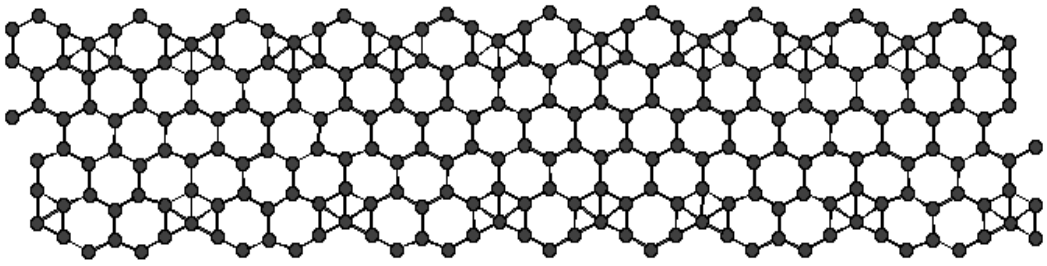

**Figure C.20** Image of relaxed 5A-1K-20H-PB model.

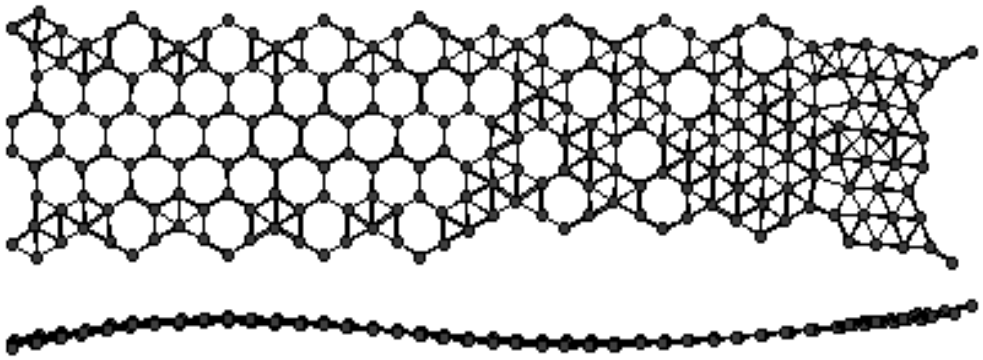

**Figure C.21** Images of relaxed 5A-1K-20H-NoPB model; top view (on top) and side view (at the bottom).

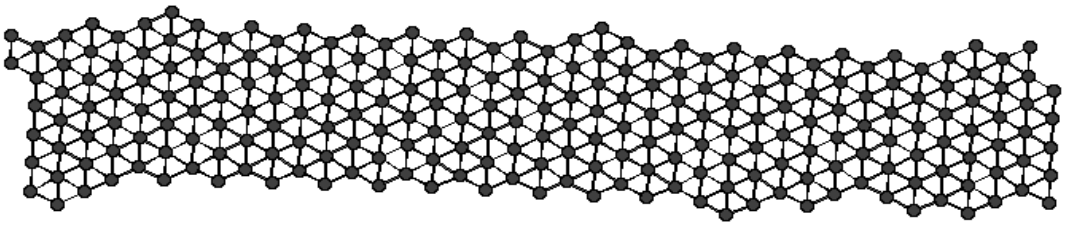

**Figure C.22** Image of relaxed 5A-300K-20H-PB model.

**Figure C.23** Image of relaxed 5A-300K-20H-NoPB model.

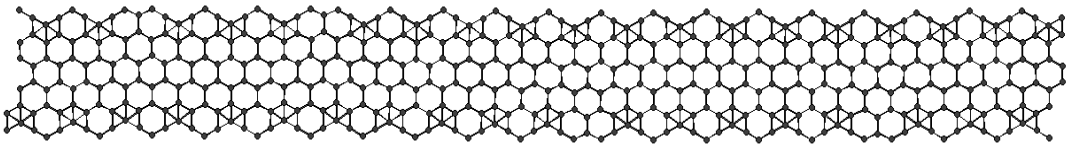

**Figure C.24** Image of relaxed 5A-1K-40H-PB model.

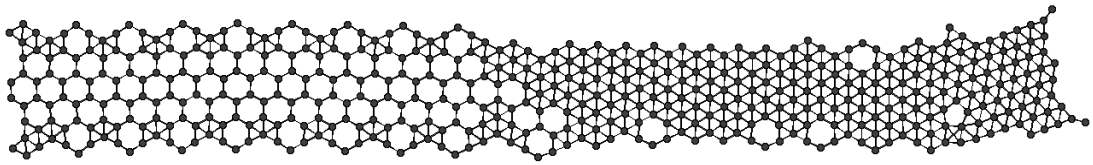

**Figure C.25** Image of relaxed 5A-1K-40H-NoPB model.

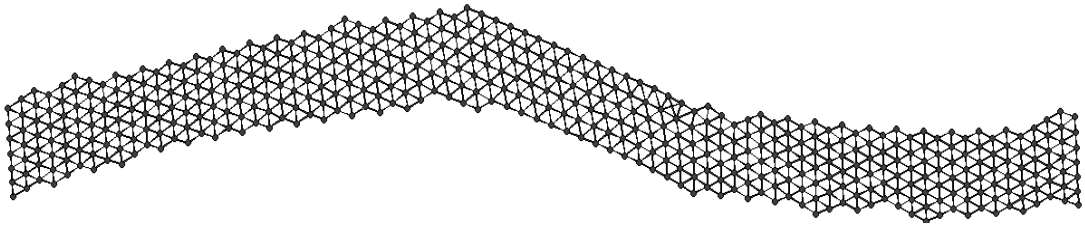

**Figure C.26** Image of relaxed 5A-300K-40H-PB model.

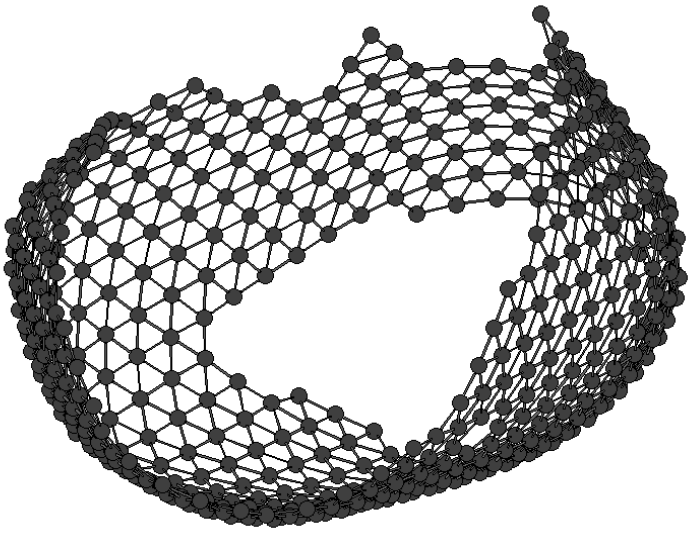

**Figure C.27** Image of relaxed 5A-300K-40H-NoPB model.

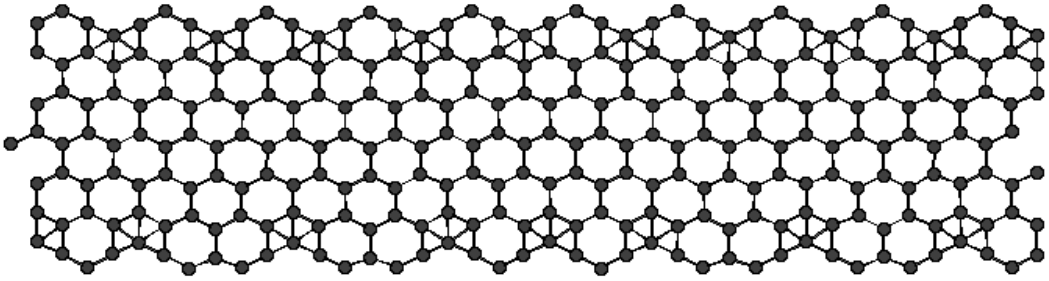

**Figure C.28** Image of relaxed 6A-1K-20H-PB model.

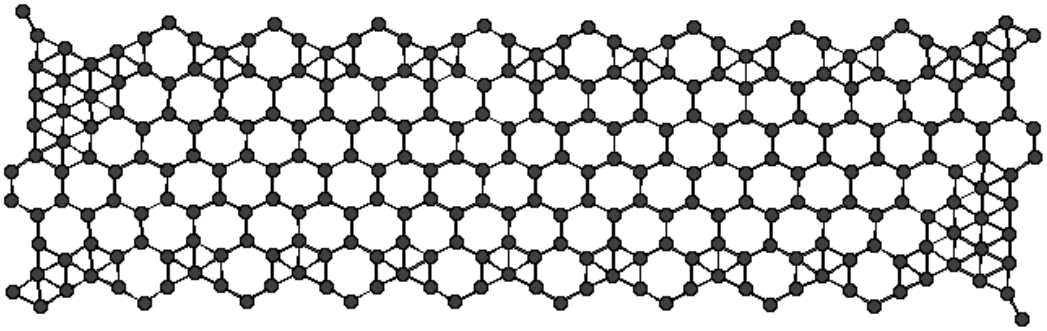

**Figure C.29** Image of relaxed 6A-1K-20H-NoPB model.

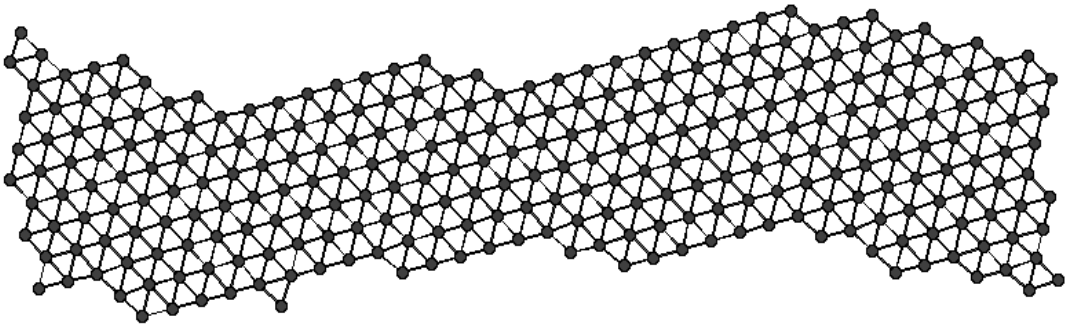

**Figure C.30** Image of relaxed 6A-300K-20H-PB model.

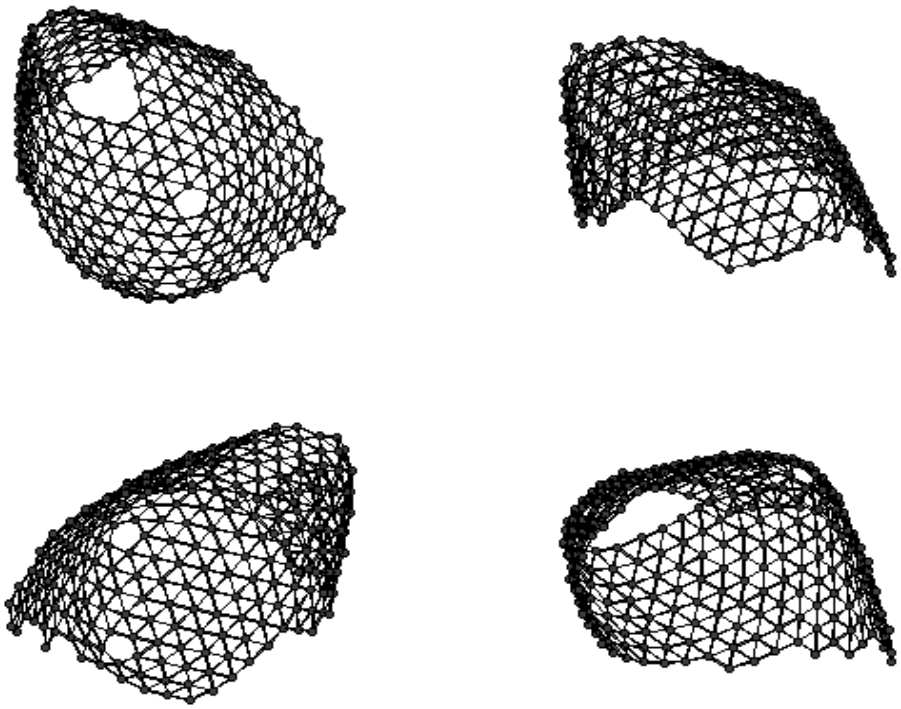

**Figure C.31** Images of relaxed 6A-300K-20H-NoPB model;four different views of the structure is given.

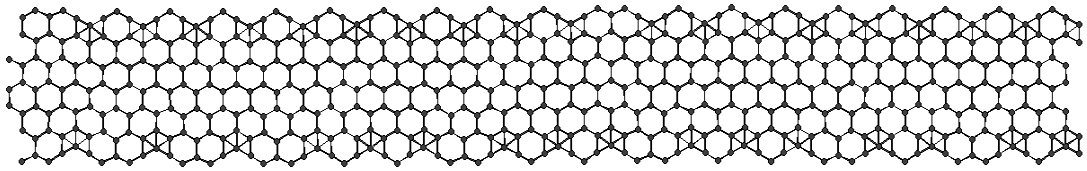

**Figure C.32** Image of relaxed 6A-1K-40H-PB model.

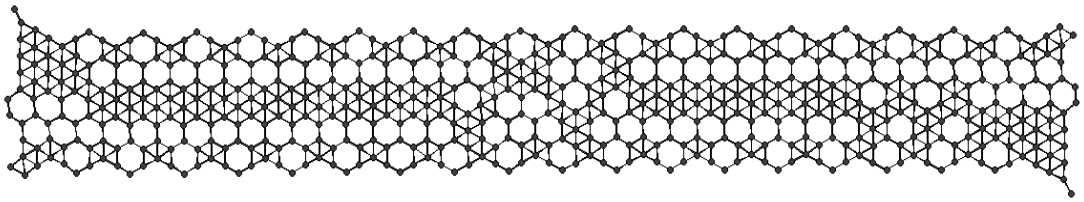

**Figure C.33** Image of relaxed 6A-1K-40H-NoPB model.

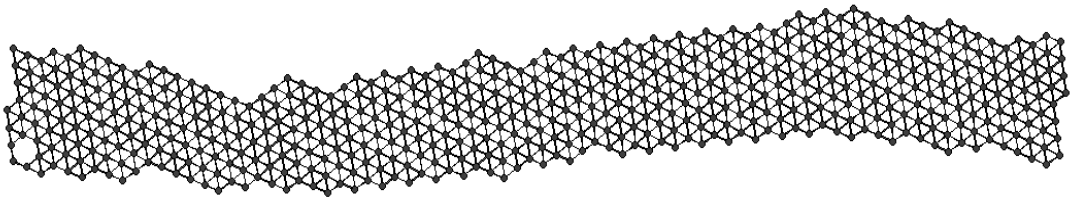

**Figure C.34** Image of relaxed 6A-300K-40H-PB model.

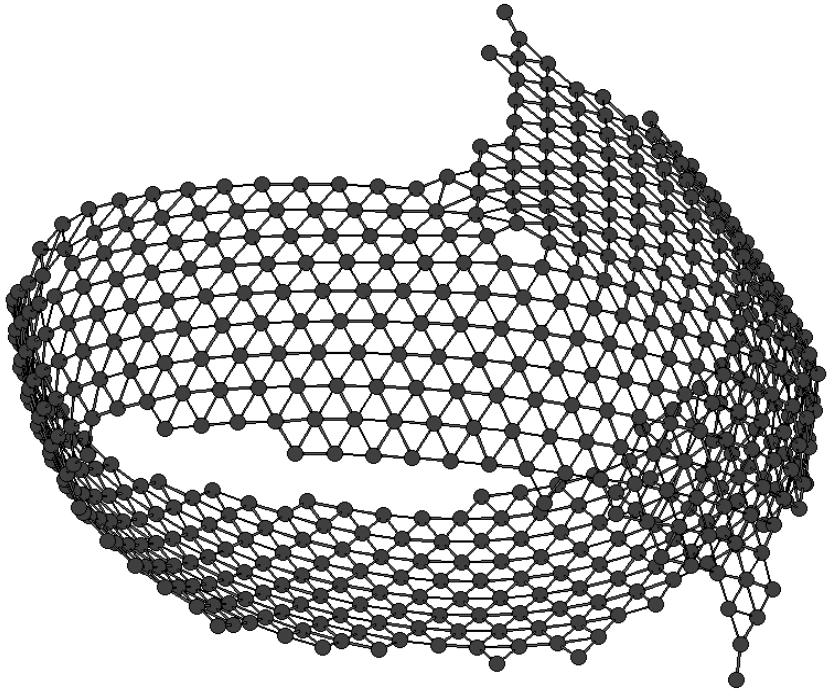

**Figure C.35** Image of relaxed 6A-300K-40H-NoPB model.

## C.2 Strained SiNR Structures

In this section, the strained SiNR structures found in the secondpart of the study which are not included in the Chapter 3 are shown. The images had to be shown at different scales due to the sizing issues of the images to fit the format of this thesis. But however, the length and width of the SiNR sheets would be sufficient to give a feeling of size if different SiNR structures are compared. Each image represents a strained version of the previous image even if its length does not seem larger due to the constriction of the page (due to the fitting issue).

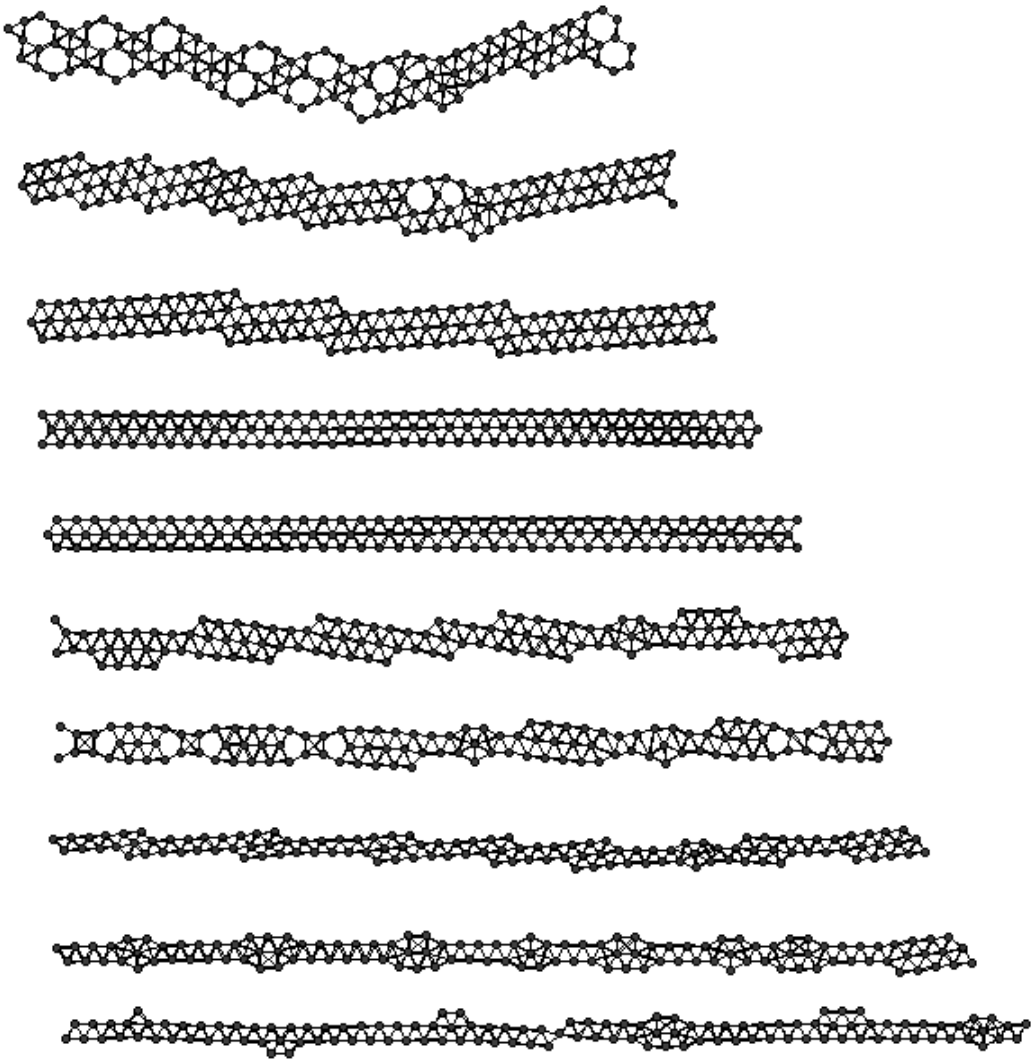

**Figure C.36** Behavior of 2A-1K-S model SiNR under uniaxial strain (Steps 1-10).

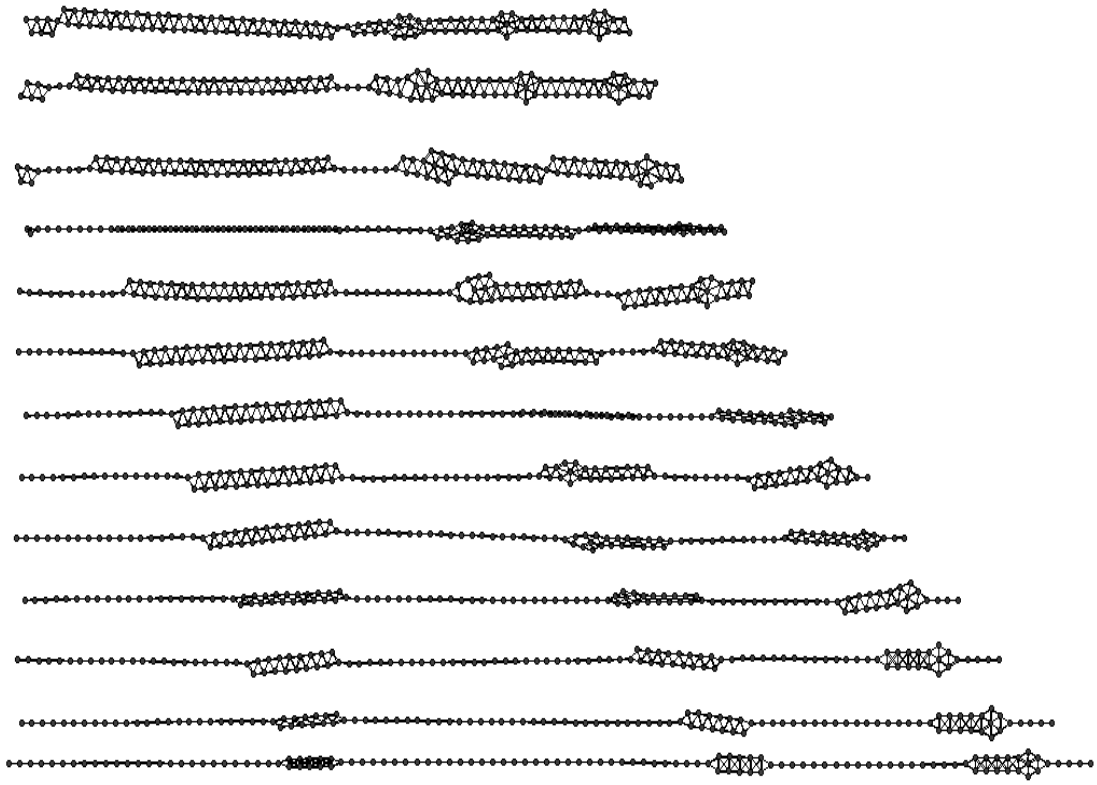

**Figure C.37** Behavior of 2A-1K-S model SiNR under uniaxial strain (Steps 11-23).

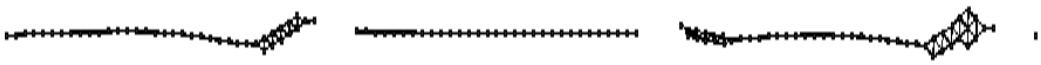

**Figure C.38** Behavior of 2A-1K-S model SiNR under uniaxial strain (Step 24). Fragmentation occurs at 24$^{th}$ step of %5 strain application.

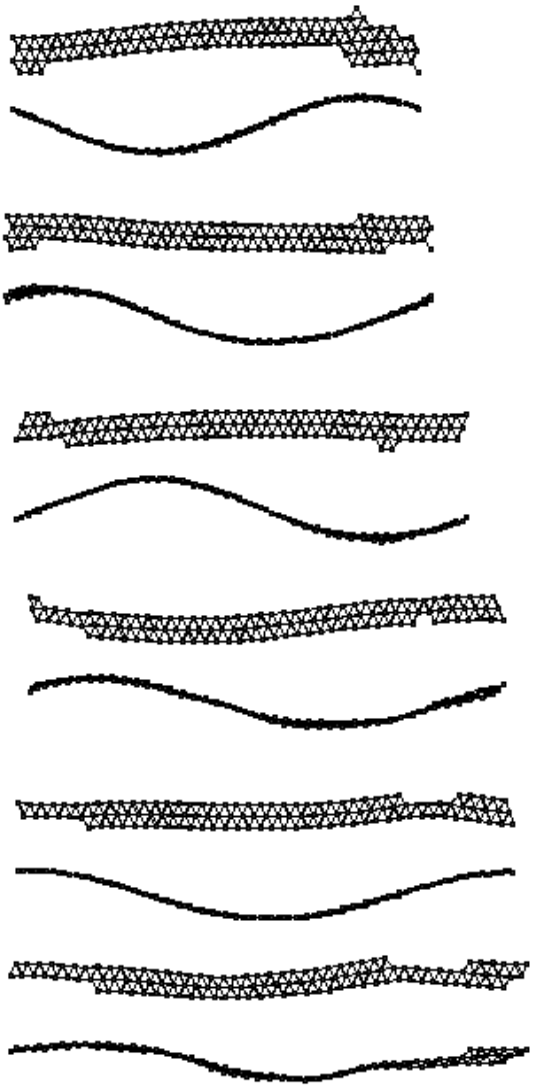

**Figure C.39** Behavior of 2A-300K-S model SiNR under uniaxial strain (Steps 1-6). Two images at two different views are given for each step; top view (on top) and side view (at the bottom).

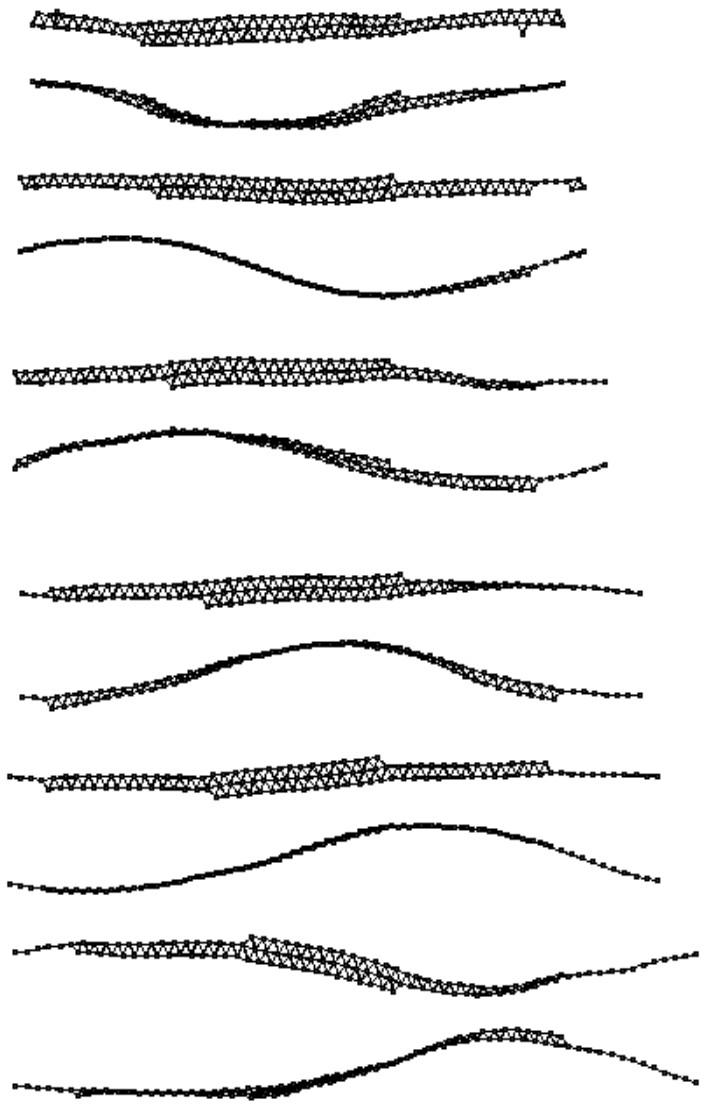

**Figure C.40** Behavior of 2A-300K-S model SiNR under uniaxial strain (Steps 7-12).Two images at two different views are given for each step; top view (on top) and side view (at the bottom).

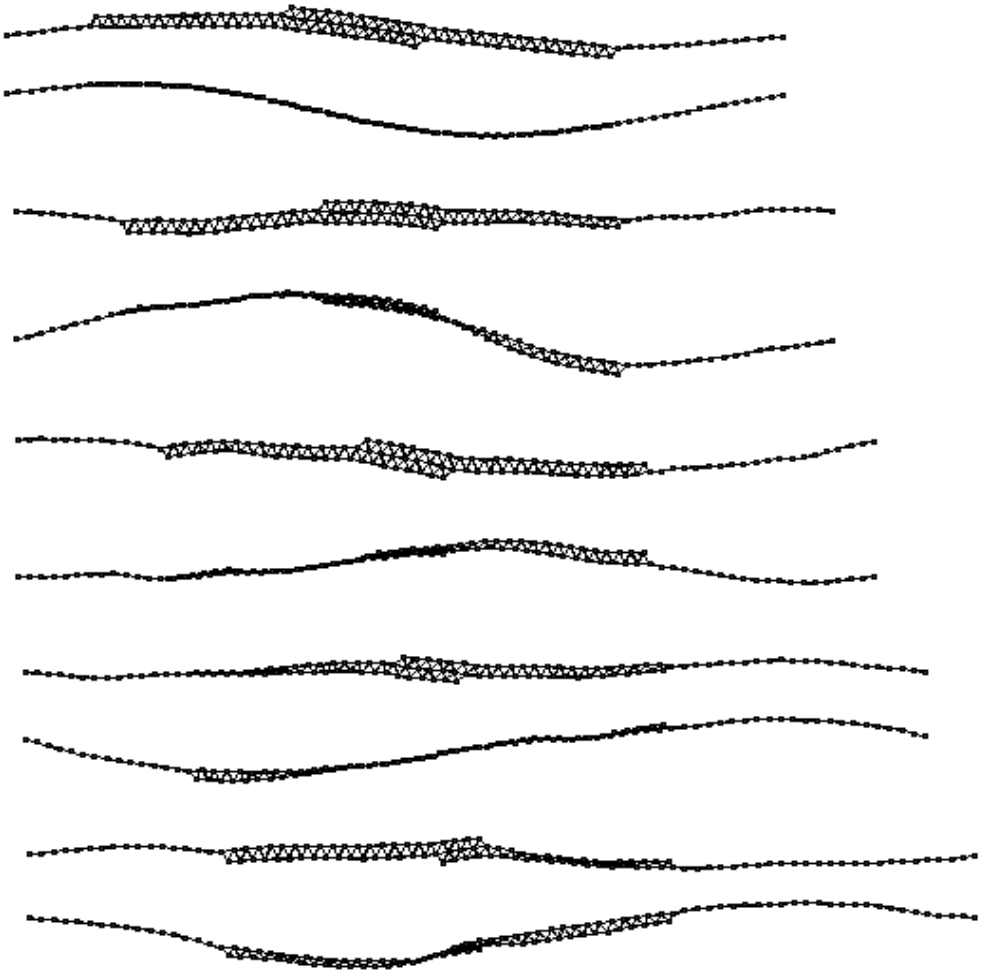

**Figure C.41** Behavior of 2A-300K-S model SiNR under uniaxial strain (Steps 13-17).Two images at two different views are given for each step; top view (on top) and side view (at the bottom).

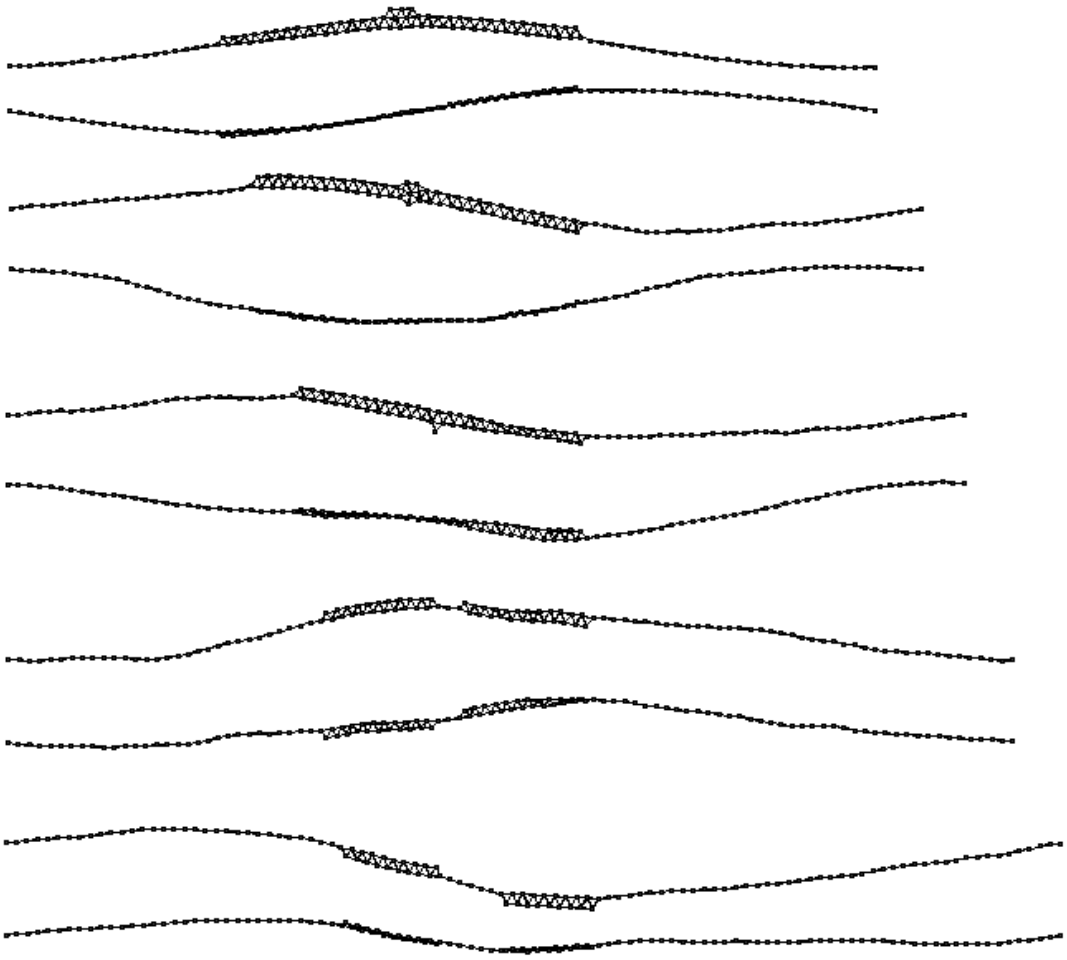

**Figure C.42** Behavior of 2A-300K-S model SiNR under uniaxial strain (Steps 18-22).Two images at two different views are given for each step; top view (on top) and side view (at the bottom).

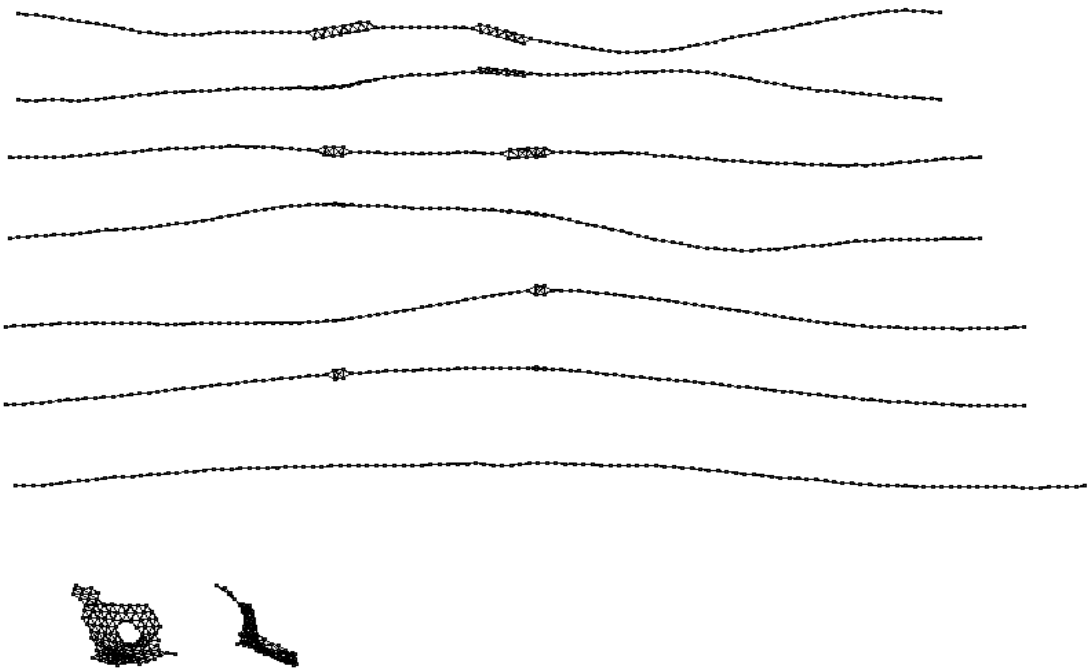

**Figure C.43** Behavior of 2A-300K-S model SiNR under uniaxial strain (Steps 23-27).Two images at two different views are given for each step; top view (on top) and side view (at the bottom). For the 27$^{th}$ step where the fragmentation occurs, two different views are given.

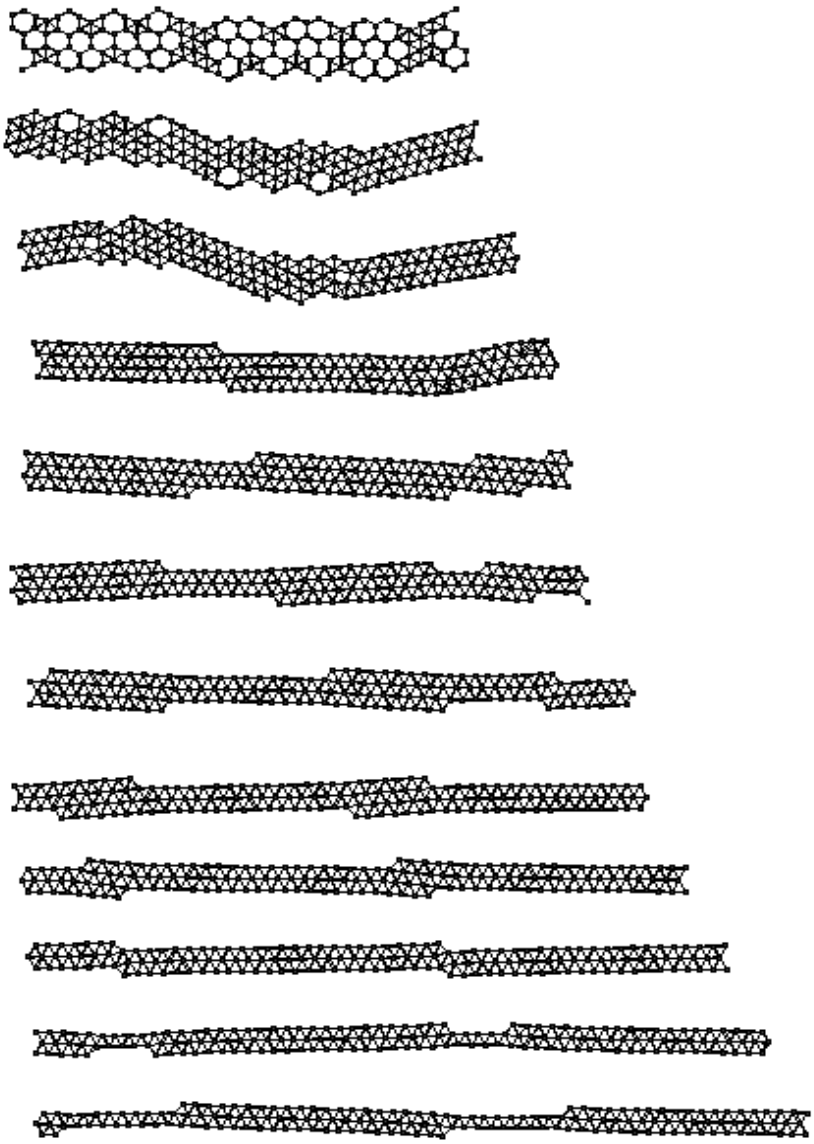

**Figure C.44** Behavior of 3A-1K-S model SiNR under uniaxial strain (Steps 1-12).

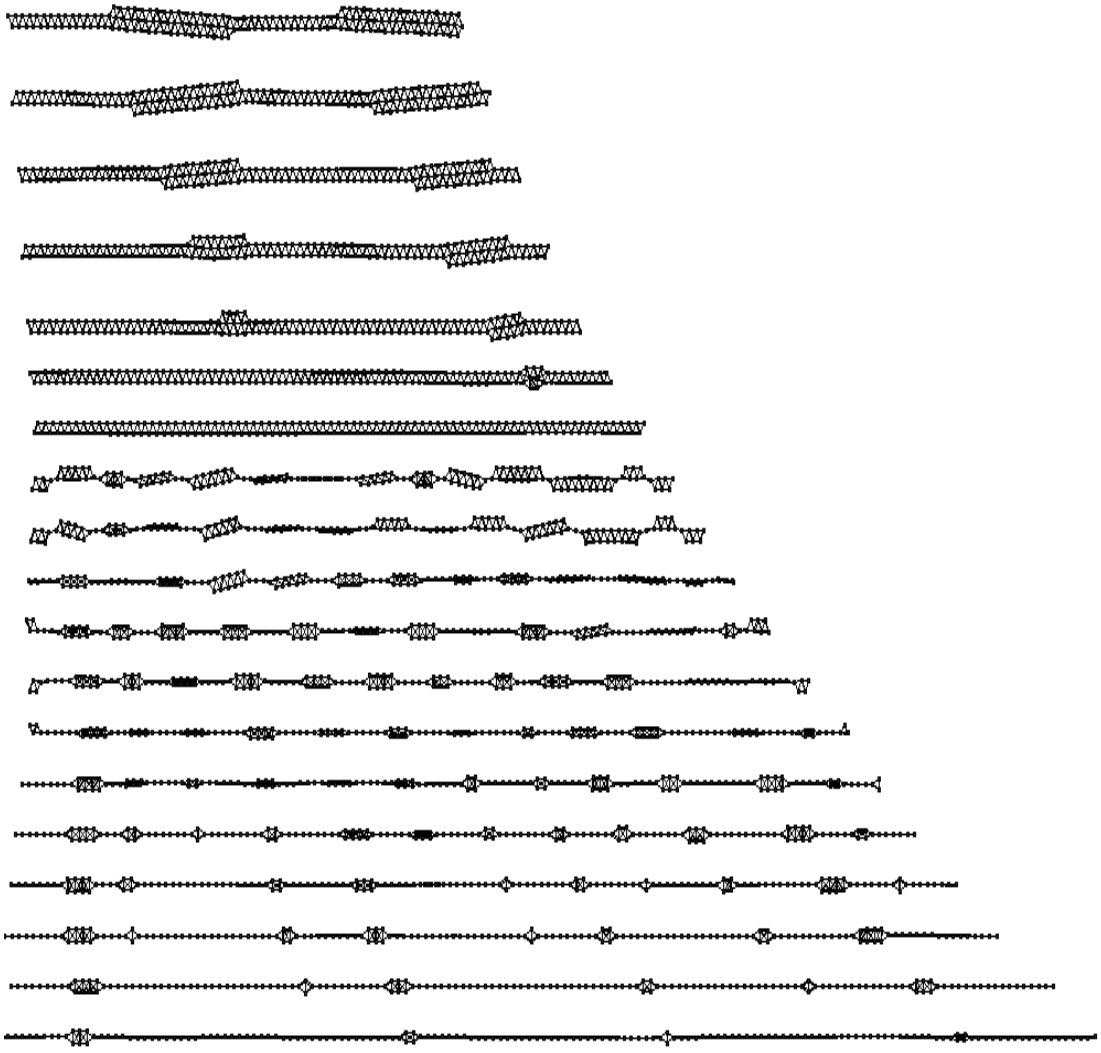

**Figure C.45** Behavior of 3A-1K-S model SiNR under uniaxial strain (Steps 13-31).

**Figure C.46** Behavior of 3A-1K-S model SiNR under uniaxial strain (Steps 32-33).

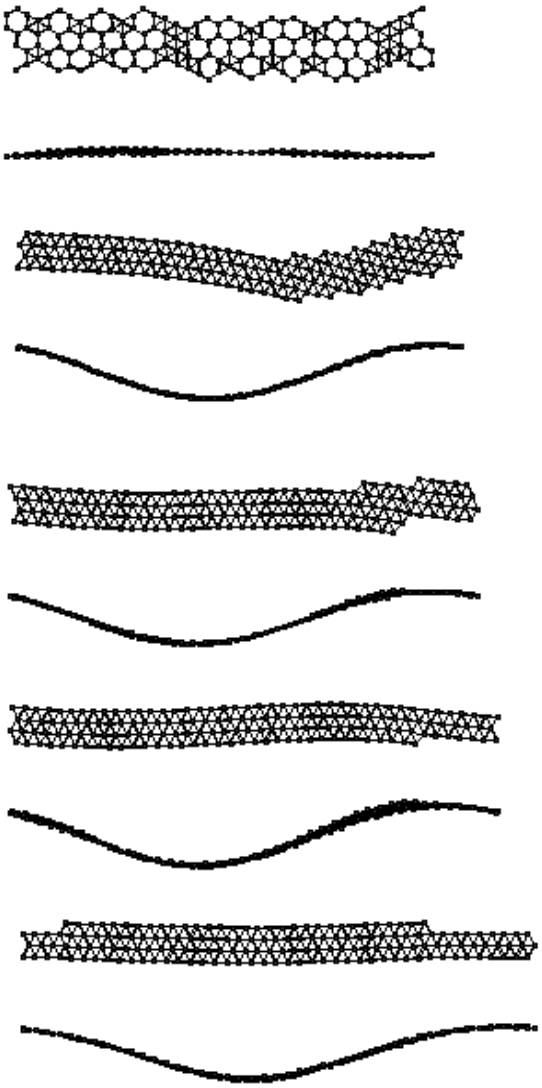

**Figure C.47** Behavior of 3A-300K-S model SiNR under uniaxial strain (Steps 1-5).Two images at two different views are given for each step; top view (on top) and side view (at the bottom).

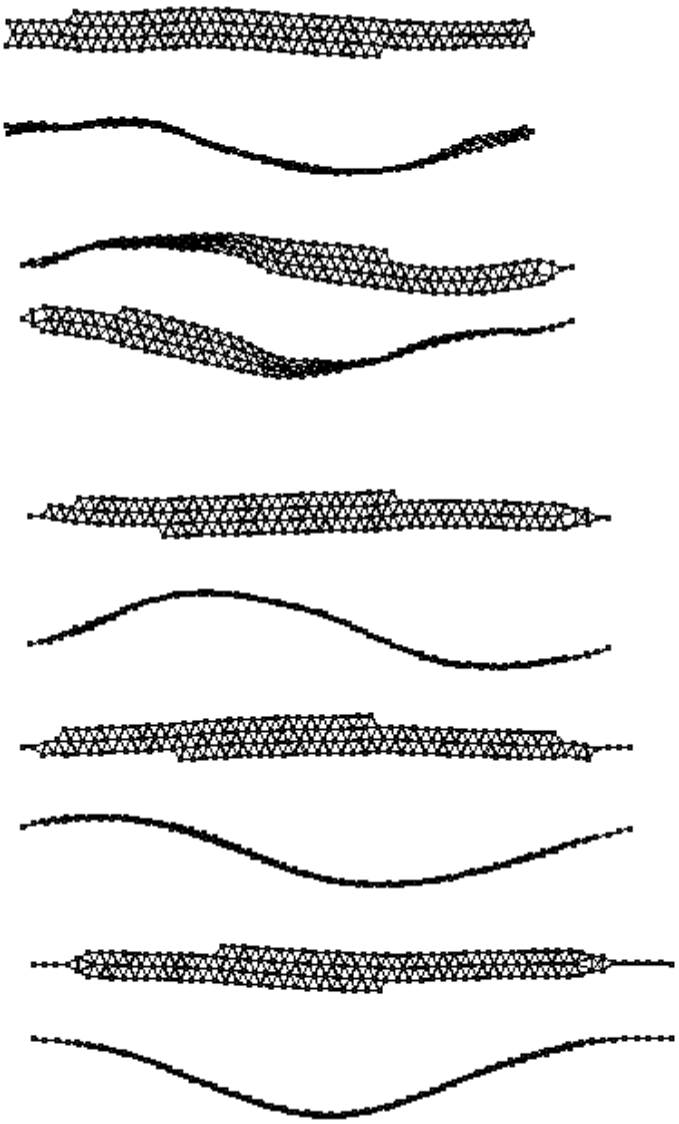

**Figure C.48** Behavior of 3A-300K-S model SiNR under uniaxial strain (Steps 6-10).Two images at two different views are given for each step; top view (on top) and side view (at the bottom).

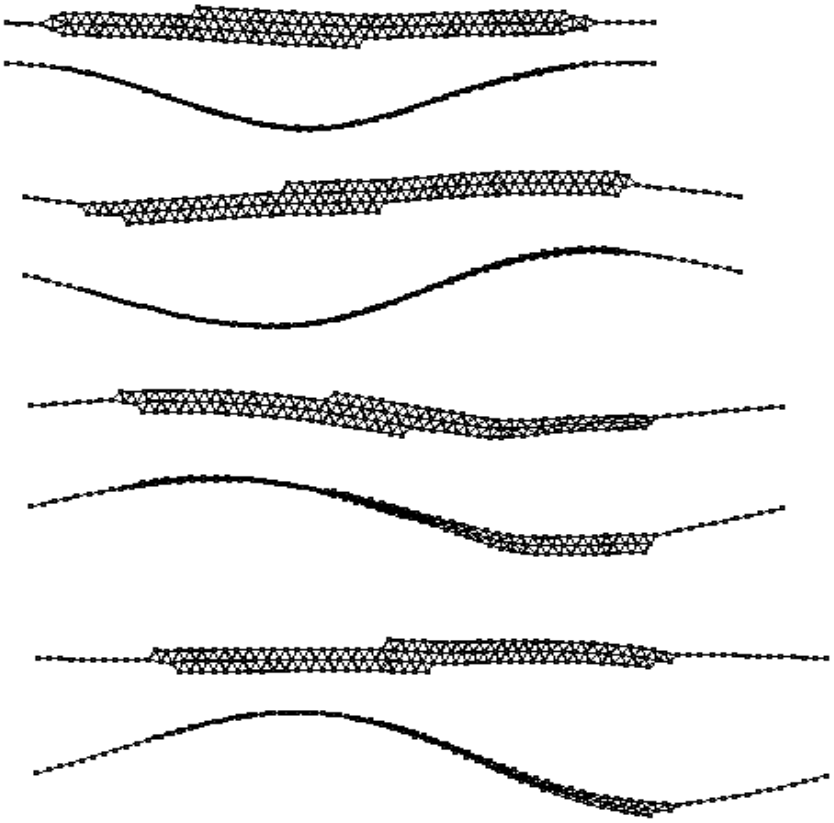

**Figure C.49** Behavior of 3A-300K-S model SiNR under uniaxial strain (Steps 11-14).Two images at two different views are given for each step; top view (on top) and side view (at the bottom).

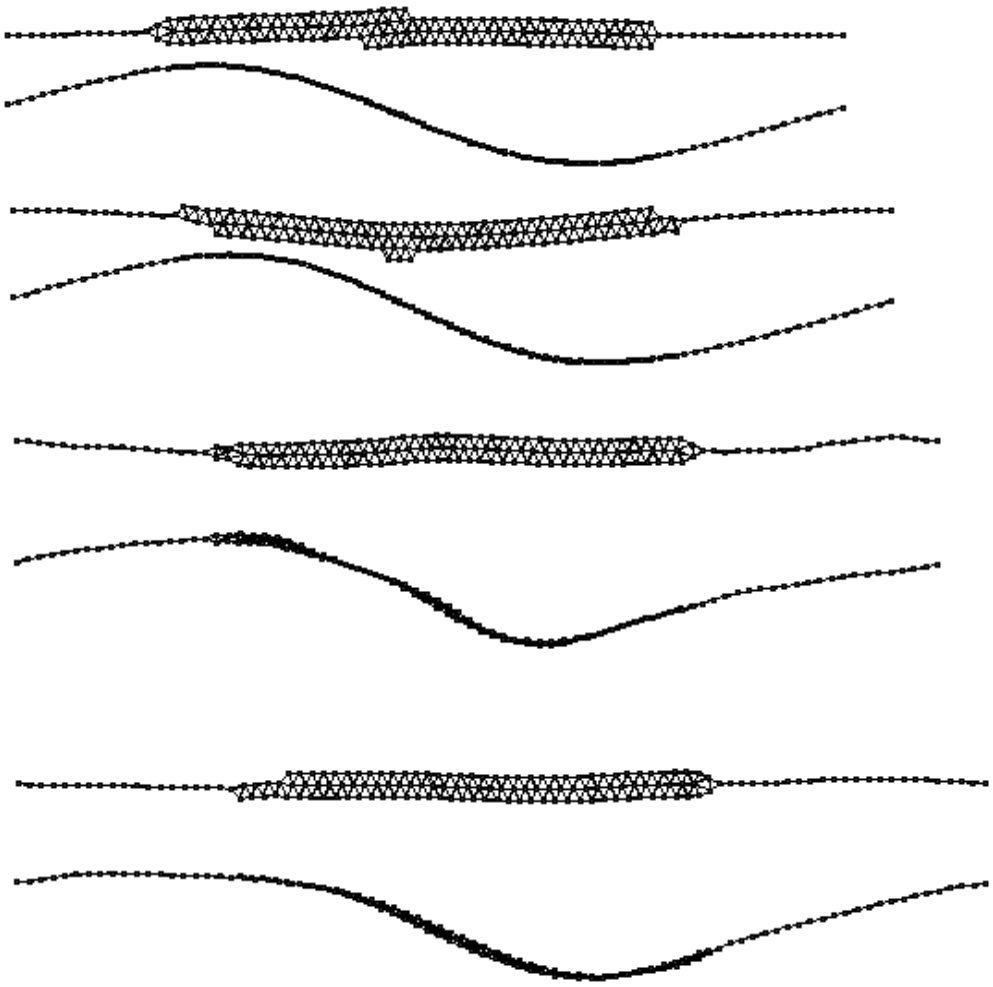

**Figure C.50** Behavior of 3A-300K-S model SiNR under uniaxial strain (Steps 15-18).Two images at two different views are given for each step; top view (on top) and side view (at the bottom).

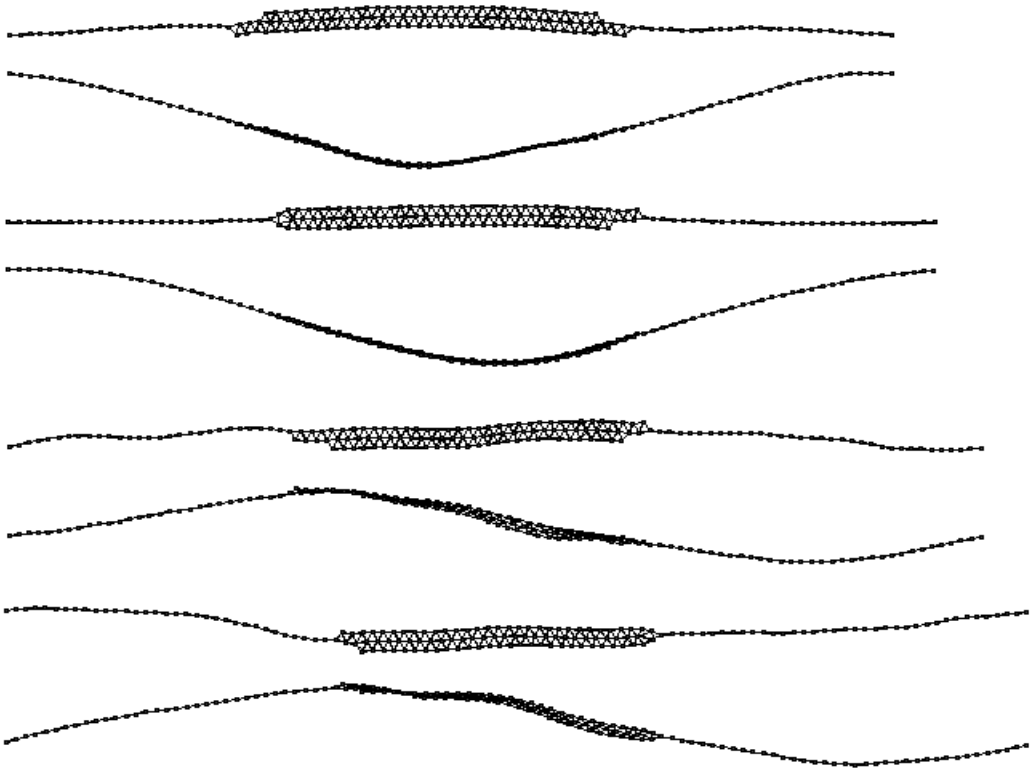

**Figure C.51** Behavior of 3A-300K-S model SiNR under uniaxial strain (Steps 19-23).Two images at two different views are given for each step; top view (on top) and side view (at the bottom).

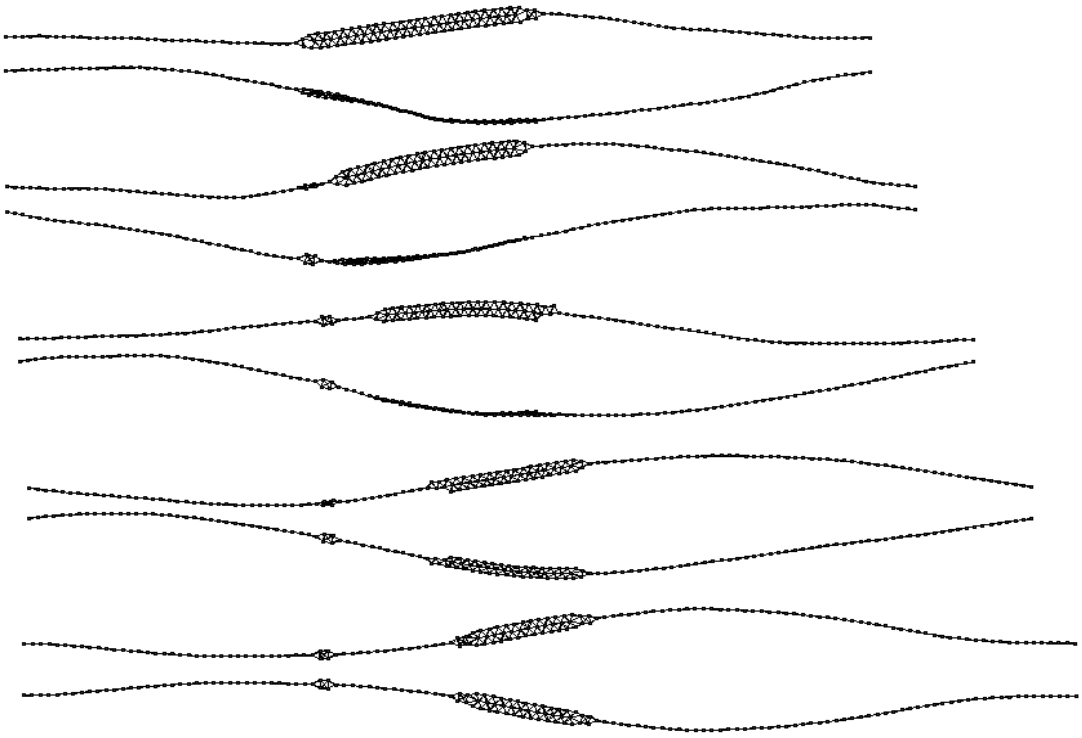

**Figure C.52** Behavior of 3A-300K-S model SiNR under uniaxial strain (Steps 24-27).Two images at two different views are given for each step; top view (on top) and side view (at the bottom).

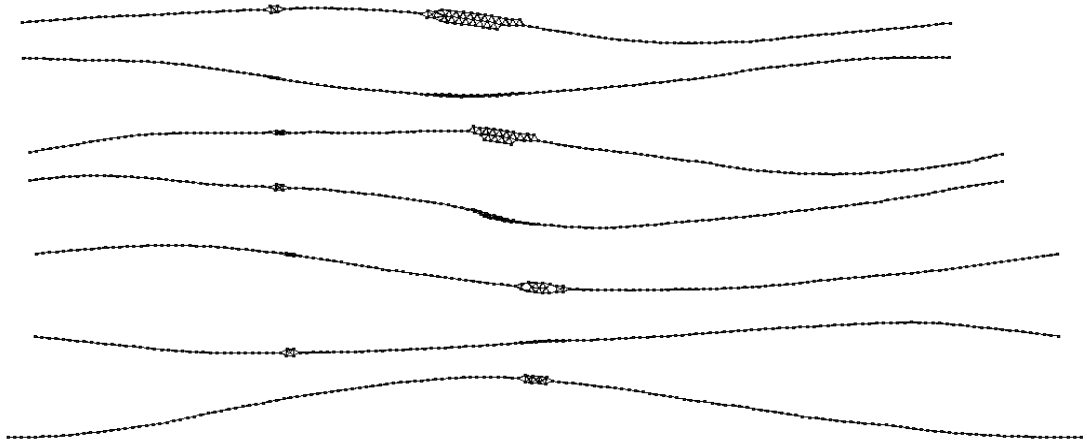

**Figure C.53** Behavior of 3A-300K-S model SiNR under uniaxial strain (Steps 28-31).Two images at two different views are given for each step; top view (on top) and side view (at the bottom).

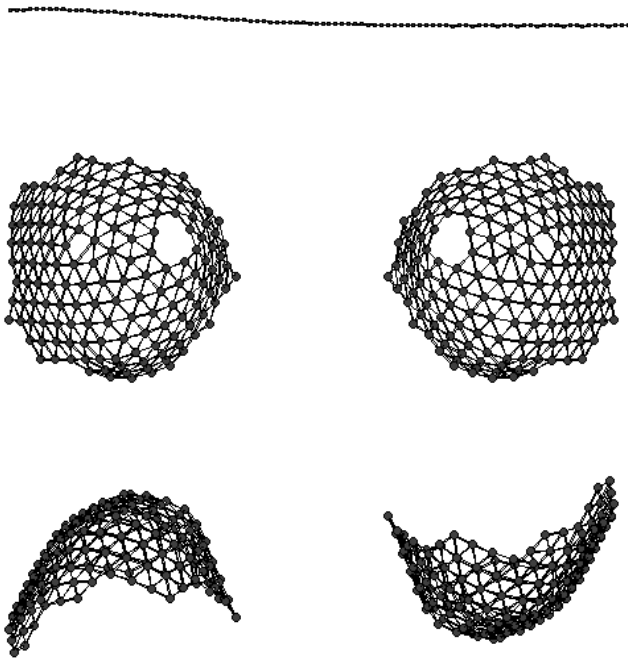

**Figure C.54** Behavior of 3A-300K-S model SiNR under uniaxial strain (Steps 32-33). For the 33$^{rd}$ step where the fragmentation occurs, four different views are given.

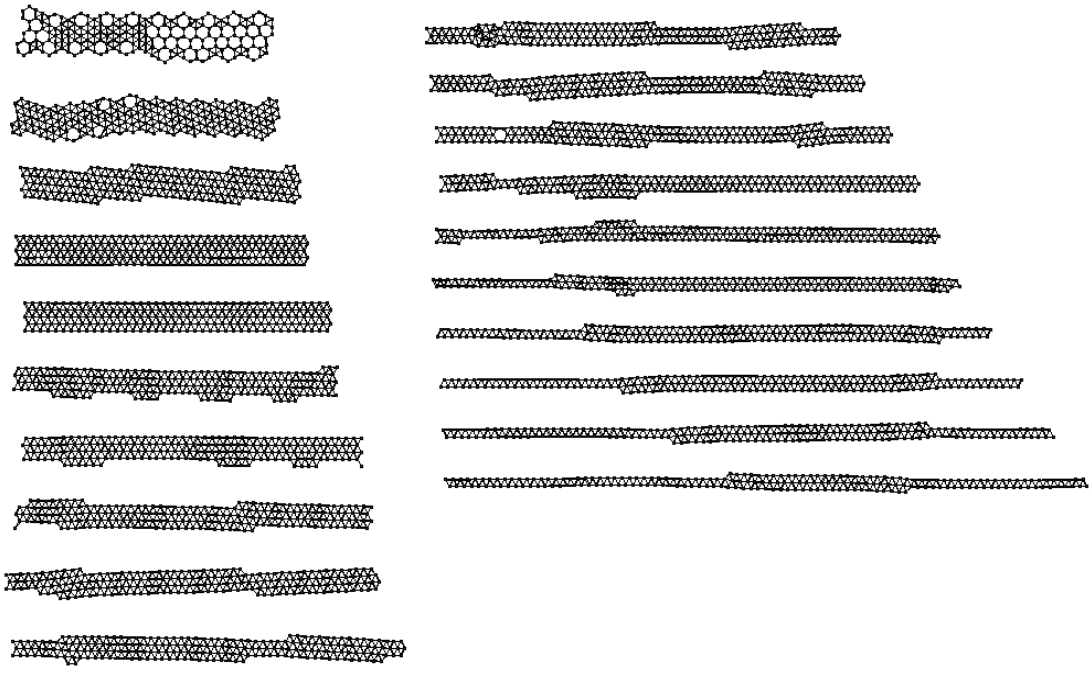

**Figure C.55** Behavior of 4A-1K-S model SiNR under uniaxial strain (Steps 1-20).

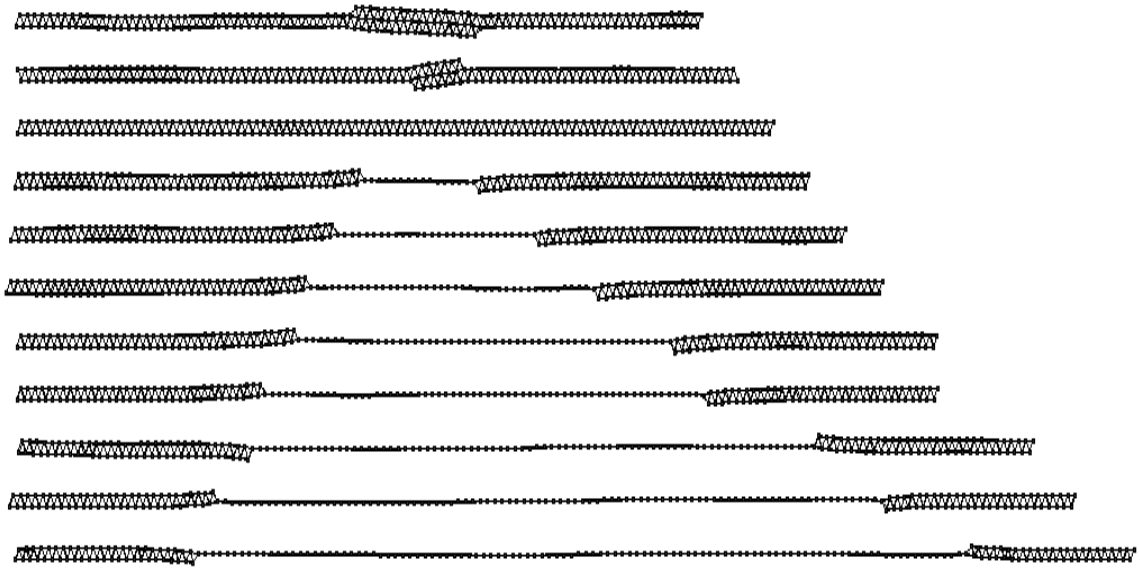

**Figure C.56** Behavior of 4A-1K-S model SiNR under uniaxial strain (Steps 21-31).

**Figure C.57** Behavior of 4A-1K-S model SiNR under uniaxial strain (Steps 32-38). Fragmentation occurs at 38$^{th}$ step.

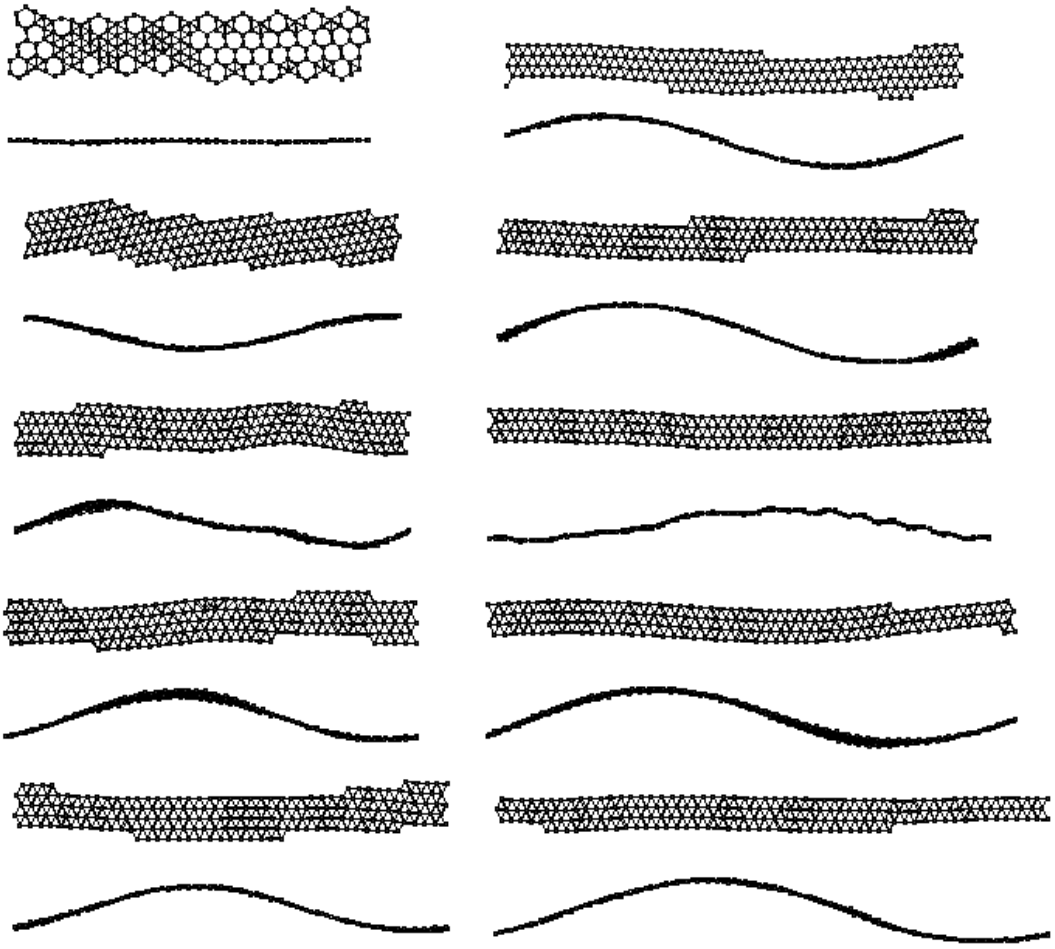

**Figure C.58** Behavior of 4A-300K-S model SiNR under uniaxial strain (Steps 1-10).Two images at two different views are given for each step; top view (on top) and side view (at the bottom).

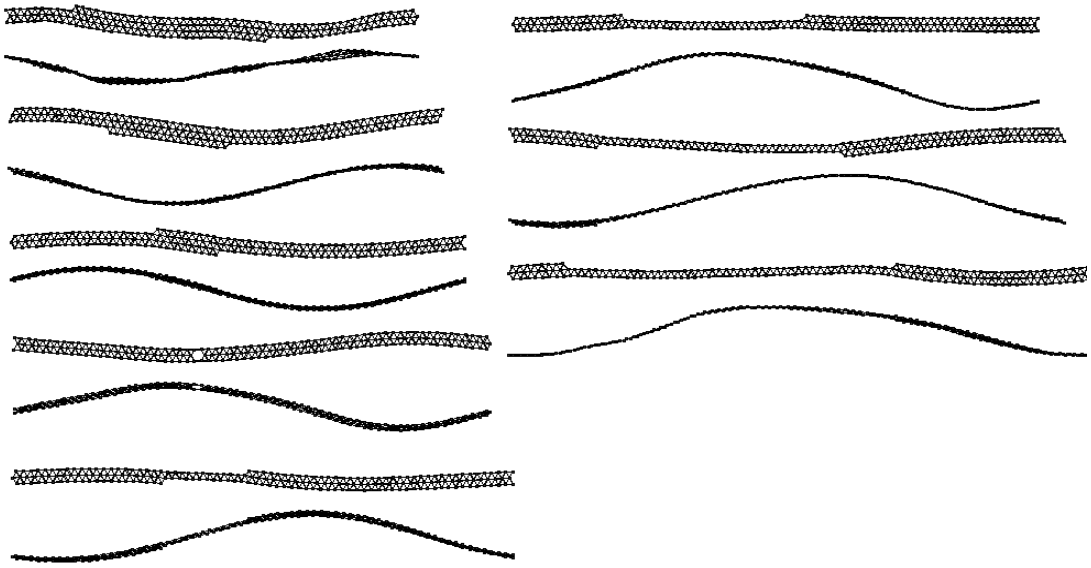

**Figure C.59** Behavior of 4A-300K-S model SiNR under uniaxial strain (Steps 11-18).Two images at two different views are given for each step; top view (on top) and side view (at the bottom).

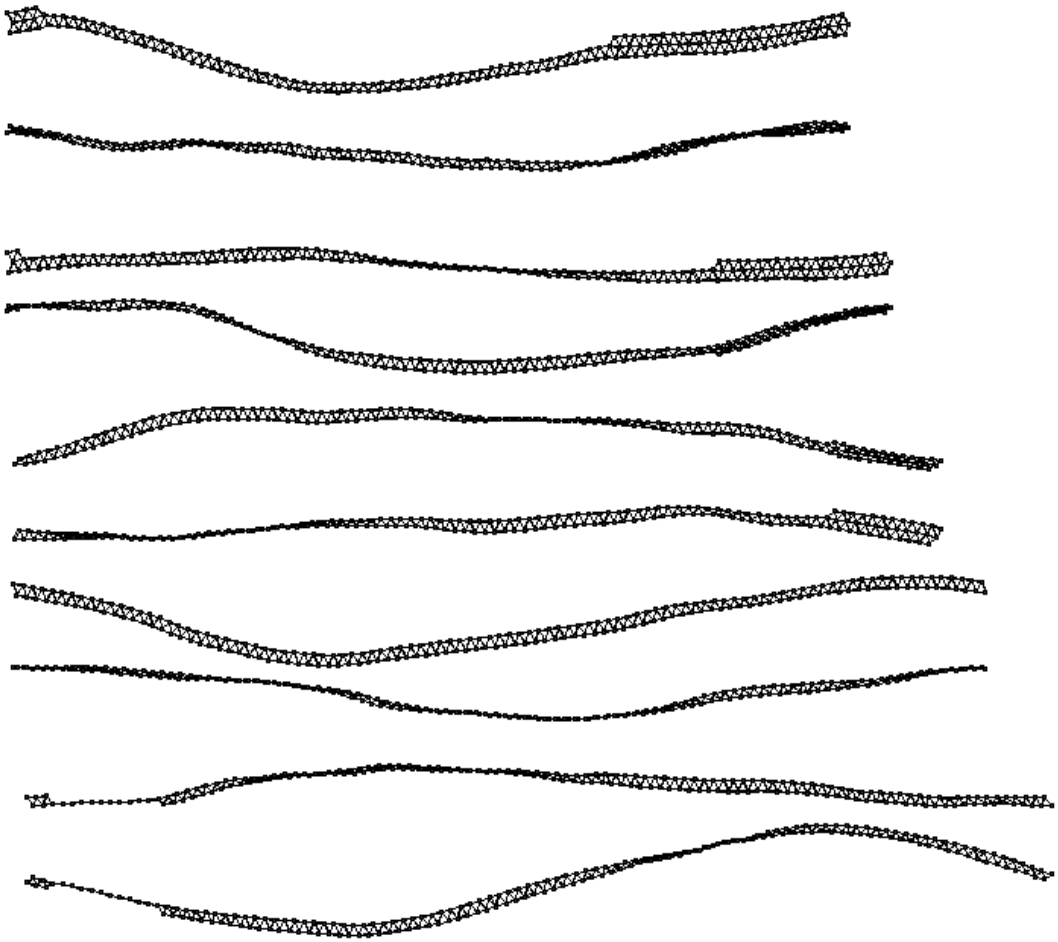

**Figure C.60** Behavior of 4A-300K-S model SiNR under uniaxial strain (Steps 19-23).Two images at two different views are given for each step; top view (on top) and side view (at the bottom).

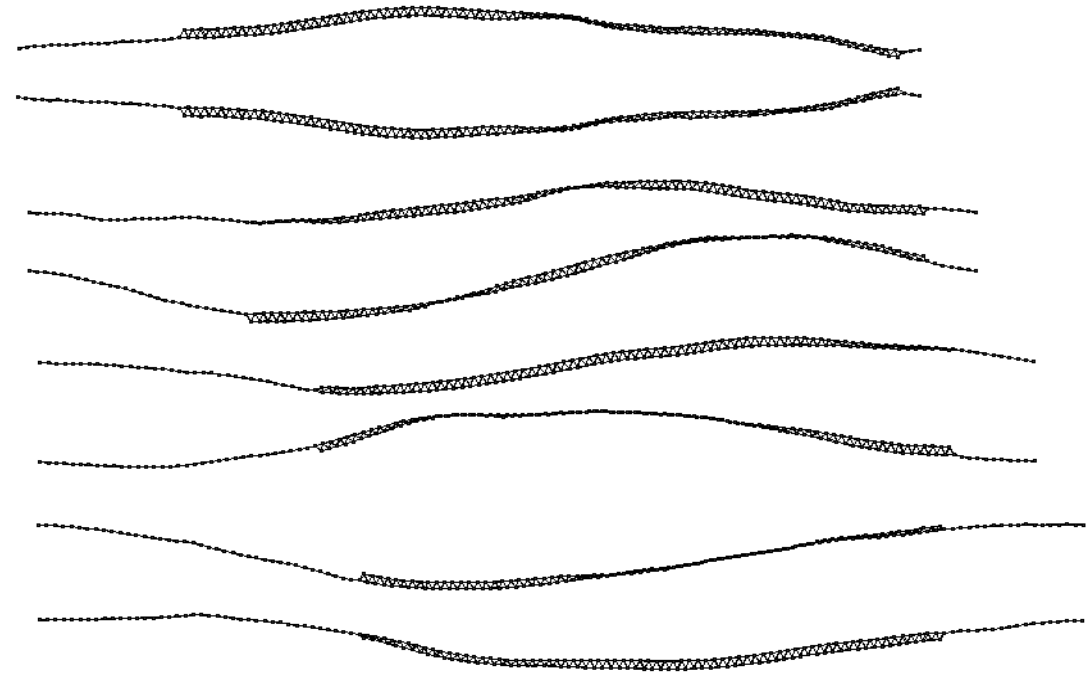

**Figure C.61** Behavior of 4A-300K-S model SiNR under uniaxial strain (Steps 24-27).Two images at two different views are given for each step; top view (on top) and side view (at the bottom).

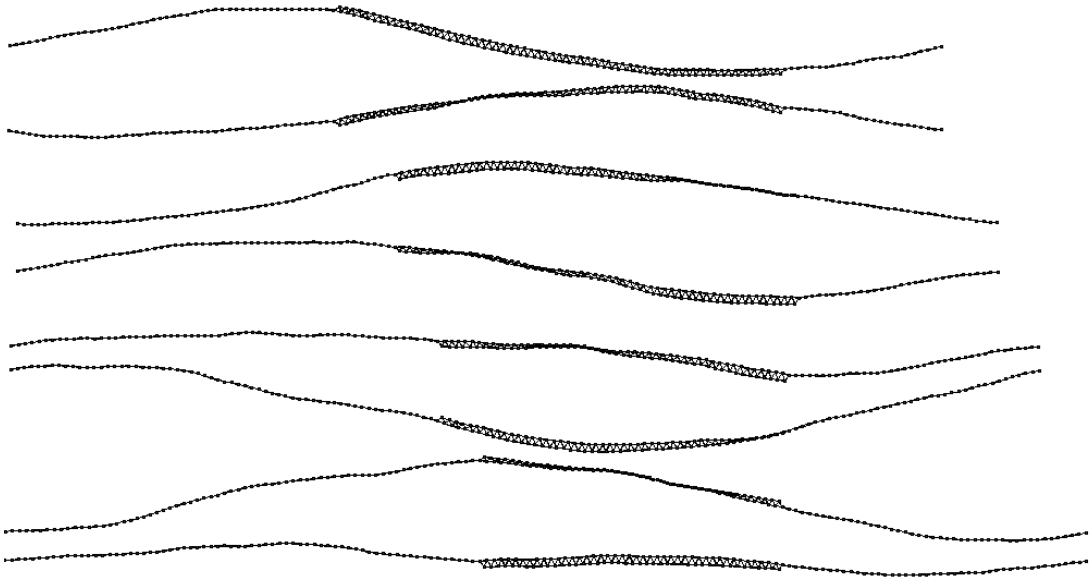

**Figure C.62** Behavior of 4A-300K-S model SiNR under uniaxial strain (Steps 28-31).Two images at two different views are given for each step; top view (on top) and side view (at the bottom).

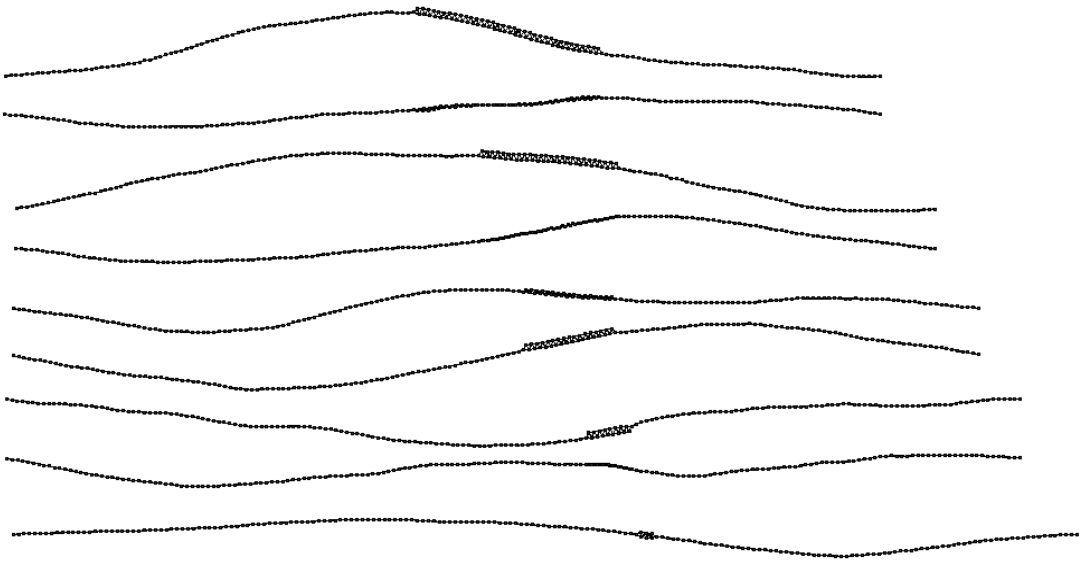

**Figure C.63** Behavior of 4A-300K-S model SiNR under uniaxial strain (Steps 32-36). Two images at two different views are given for each step; top view (on top) and side view (at the bottom). Only for the 36$^{th}$ step, only one image is given since the structure is almost a chain.

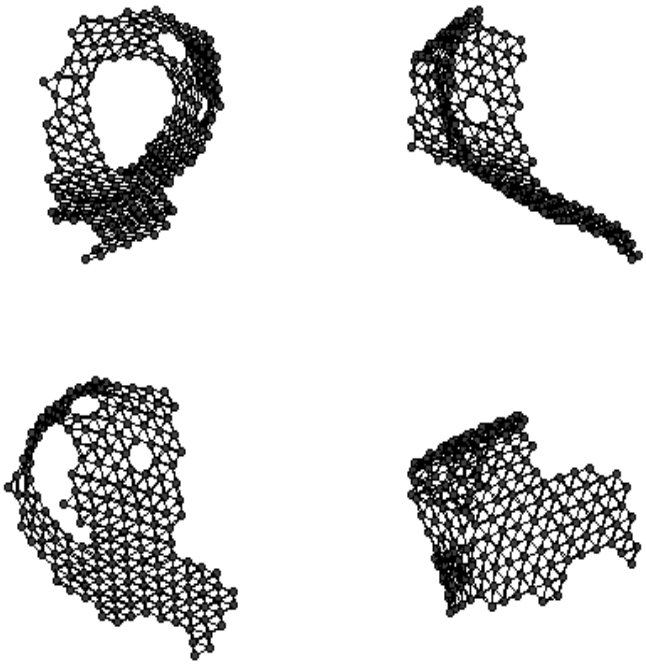

**Figure C.64** Behavior of 4A-300K-S model SiNR under uniaxial strain (Step 37). At 37$^{th}$ step, fragmentation occurs and in this figure, the final structure is shown at four different views.